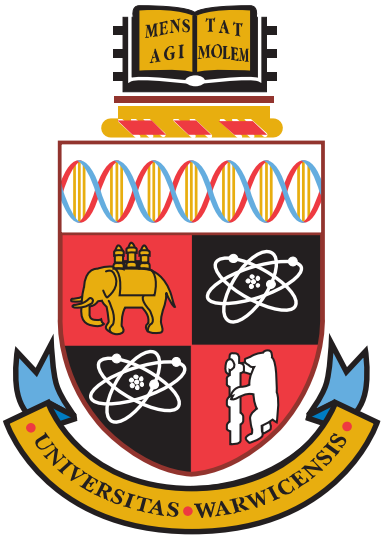

Collisional transport of trace impurity ions and the role of the radial electric field in spherical tokamak plasmas

by

Christopher Glyn Wrench

Thesis

Submitted to the University of Warwick

for the degree of

Doctor of Philosophy

Physics

September 2012

THE UNIVERSITY OF
WARWICK

Table of Contents

List of Figures

List of Tables

Declarations

The work presented in this thesis is the original work of the author, except where noted. This work was conducted at the University of Warwick under the supervision of Dr E. Verwichte and in collaboration with Dr K. G. McClements of the Culham Centre for Fusion Energy. This work has not been submitted for the award of any other degree. Parts of this work have appeared in the proceedings of the 38^{th} EPS Conference on Plasma Physics.

Acknowledgments

It is a pleasure to thank the many people who have helped me throughout the preparation of this thesis.

Firstly, I offer my sincerest gratitude to my supervisor, Dr Erwin Verwichte, whose patience and experience have been invaluable to me. The inspiration provided by his academic expertise is difficult to overstate. For his support and guidance I would also like to thank Dr Ken McClements, whose knowledge of tokamak physics has contributed greatly to my learning and this thesis. I am also grateful to the staff and fellow Ph.D. students of the Centre for Fusion, Space and Astrophysics for countless illuminating discussions and for making my studies so enjoyable.

The Department of Physics and the Centre for Fusion, Space and Astrophysics have provided the support and equipment I have needed to complete my thesis and I am grateful to EPSRC for funding my studies.

My parents, Glyn and Ana, have been a constant source of support and inspiration throughout my academic career.

Finally, I am particularly indebted to my partner Rosie for her constant encouragement and without whom I would likely still be writing this thesis.

Abstract

The mitigation and control of impurities, or non-fuel ions, in tokamak plasmas is vital for reducing energy losses and an understanding of impurity transport is required in order to predict the performance of present and future tokamak devices. The development and application of a full orbit, test particle code to the study of the collisional transport of test impurity ions in spherical tokamak plasmas is presented. This code is tested against the standard analytic description of collisional transport in magnetised plasmas and is demonstrated to be particularly suited to the study of the tight aspect ratio of the spherical tokamak design.

The principle results of the present work concern the investigation of the role of the radial electric field, a feature of high performance tokamak plasmas, on collisional ion transport. It is found that a static radial electric field leads to a significant reduction in the radial transport of test impurity ions. This effect may be explained in terms of a novel radial drift of the test ions arising due to the introduction of collisional Langevin terms to the full orbit, test particle equations of motion. This has significant implications for the confinement of impurity ions in high performance, steady state tokamak discharges. A scaling of this modification with impurity particle mass and charge numbers is derived analytically and verified numerically and a scaling with electric field parameters is derived numerically.

A time dependent radial electric field, which models a number of transient events in tokamak plasmas such as the low- to high-mode transition and edge localised modes, is also investigated and attempts at a preliminary comparison between experimental and numerical observations of impurity transport in spherical tokamak devices is presented.

Chapter 1

Introduction

1.1 Magnetic confinement fusion

The grand vision of proponents of nuclear fusion is the realisation of the generation of commercial amounts of energy via nuclear fusion, the process of fusing light nuclei into heavier nuclei. The potential of nuclear fusion as a future energy source has been extensively considered with regards to fuel availability, safety, environmental impact and economics [Miller, 1998; Najmabadi, 1999; Braams and Stott, 2002; Sheffield et al., 2001; Llewelyn-Smith and Ward, 2005] and it is seen by many as a sustainable long term energy source. The process is attractive since it releases no carbon dioxide, produces a relatively small amount of benign radioactive waste and, crucially, is inherently safer than existing nuclear *fission* power plants, since fusion does not rely on a critical mass of fuel, eliminating the risk of runaway processes which have plagued the nuclear fission industry.

It is envisioned that the first generations of commercial fusion power plants will use deuterium and tritium, isotopes of hydrogen, as fuel, utilising the process

$$D + T \rightarrow He^4 + n + 17.58 \text{ MeV} \tag{1.1}$$

to generate nuclear energy. Approximately 80% of the 17.58 MeV of fusion energy released in each reaction is carried by the neutron, which can be used to generate electricity, with the rest of the energy carried by the α particle. Central to the goal of achieving *self-sustained* nuclear fusion is the effective utilisation of the energy carried by the α particle in order to continually heat the deuterium-tritium fuel and maintain a sufficiently high fusion reaction rate.

If this self heating is sufficient to overcome the various energy loss mechanisms which exist in a fusion reactor then *ignition* is achieved. This is critical to the

feasibility of future fusion reactors since, in order to be a viable source of energy, any reactor must satisfy the condition that the energy used to drive the device is far exceeded by the energy released from the fusion reactions. This requirement was first formalised by Lawson [1957] and is widely referred to as the *Lawson criterion*. This criterion is expressed as a product of three key parameters: density, n; temperature, T; and energy confinement time, τ_{E}. This condition for ignition expressed in terms of the triple product of these quantities is

$$nT\tau_{\mathrm{E}} > 3 \times 10^{21} \quad \mathrm{m}^{-3}\ \mathrm{keV\ s}. \tag{1.2}$$

Temperatures of the order of 10 keV, or approximately 110 million K, are required for the fusion reactions to occur spontaneously and in order to satisfy the Lawson criterion. At such temperatures the deuterium-tritium fuel mix is a fully ionised plasma.

Currently, the most developed concept for a nuclear fusion reactor is the tokamak, a magnetic confinement system in which strong applied magnetic fields maintain a hot plasma for sufficiently long times that enough fusion reactions occur to produce a useful amount of energy. The projected reactor values of n, T and τ_{E} have all been achieved in tokamak devices, although never simultaneously. However, the result of a large international collaboration, ITER [ITER Physics Basis Editors et al., 1999], which aims to demonstrate the commercial viability of fusion energy, is due to come on line in the next decade. ITER will address fundamental physics issues concerning the steady state operation of magnetic confinement fusion devices in operating regimes approaching that of a commercial power plant. The performance of such a device is limited by the transport processes which limit the confinement of the plasma fuel. Plasma transport is therefore a critical topic in the development of a magnetically confined fusion device and this field is rightly at the heart of fusion research.

1.2 Tokamak plasmas

Magnetic confinement devices such as tokamaks utilise strong applied magnetic fields in order to confine the charged particles which constitute the fusion plasma. Due to the solenoidal nature of the magnetic field a torus is the simplest topological configuration that can be assumed to have no magnetic field lines exiting from it's bounding surface [D'haeseleer et al., 2001]. This property of toroidal confinement systems is crucial for achieving sufficiently long energy confinement, since charged particles are constrained to move along lines of magnetic force but cannot move

across these lines, as demonstrated in section 2.3. Closed magnetic field lines which are isolated from the material walls of a tokamak device therefore ensure that, in principle, one can achieve sufficiently long energy confinement to satisfy the Lawson criterion (however, it shall be shown that collisional processes, for example, limit this confinement).

Of great importance for toroidal plasma equilibrium and stability calculations and transport analysis are flux coordinates (Ψ, θ, φ), which are natural coordinates for describing a torus. Generally Ψ is the *flux surface label*, which can loosely be identified with the minor radius of the torus and which identifies surfaces of constant plasma pressure, φ is the geometric toroidal angle and θ is the geometric poloidal angle. Here the toroidal and poloidal directions refer to the long way around and the short way around the torus respectively, as depicted in figure 1.1.

The conventional design for a tokamak device is presented in figure 1.1. The fusion plasma is contained in a toroidal vacuum vessel, surrounded by a metallic wall which is one of a number of *plasma facing components*, and held in isolation from the material walls by a helical magnetic field. The helical nature of the magnetic field is key to the stability of the plasma. There are two major components required to generate this magnetic field. The first is the *central solenoid* (orange in figure 1.1), an iron core which passes through the centre of the toroidal vacuum vessel. The voltage applied to the primary circuit is slowly swept from a large positive to a large negative value, magnetising the iron core and inducing a toroidal current in the plasma, analogously to the secondary coil of a transformer. This toroidal current in the plasma gives rise to a poloidal magnetic field. In addition, large D-shaped *toroidal magnetic field coils* (blue in figure 1.1) generate a toroidal magnetic field component. In equilibrium, the applied tokamak magnetic field balances the outward pressure of the high temperature fusion plasma. Often this requires the generation of additional poloidal magnetic field or of a vertical magnetic field, using additional external coils.

The external coils can be used to shape the fusion plasma, so that the shape of the plasma poloidal cross section (a cross section of the plasma at constant toroidal angle) is not simply circular. Since in a tokamak power plant the temperature and density profiles will be largely self-determined by fusion energy production and plasma transport the shape of the plasma is left as a free parameter of the tokamak design for controlling plasma performance. This magnetic shaping may be used to operate a so called *diverted* plasma configuration. In this case the confined plasma is surrounded by a region of open magnetic field lines, which direct any particles which leave the confined plasma to the *divertor*, a dedicated region of the first wall which can withstand the flux due to this exhaust of particles. The *separatrix*, or *last closed*

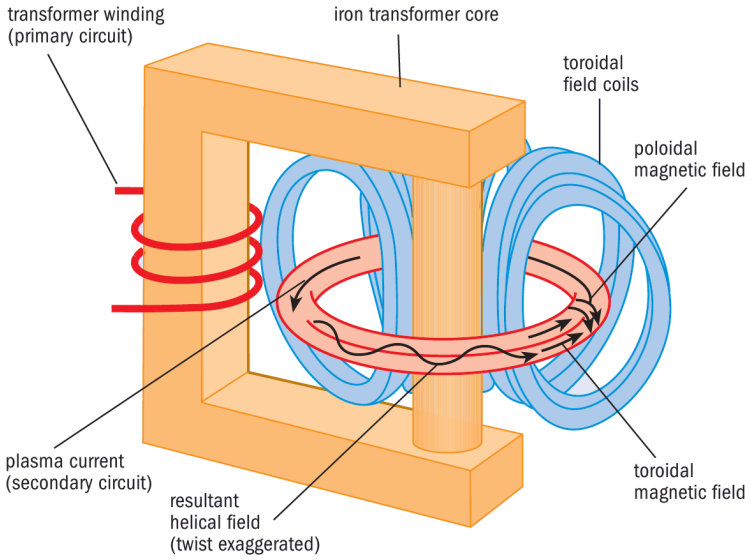

Figure 1.1: Schematic of the conventional tokamak design [Nuttall, 2008]. The fusion plasma is confined in a toroidal vacuum vessel by toroidal and poloidal magnetic fields, generated by toroidal field coils and the plasma current induced by the transformer action respectively. The resultant helical magnetic field is crucial for plasma stability.

flux surface, is the curve which separates the regions of closed and open magnetic field lines. An alternative configuration which pre-dates the divertor configuration is the *limited* plasma configuration, in which the minor radial extent of the plasma is physically restricted by a *limiter* that extends in from the vacuum vessel wall.

Typically the plasma energy density is much smaller than the magnetic field energy [Wesson, 2004], which has important consequences for the cost of electricity produced via magnetic confinement devices. The ratio of plasma pressure to magnetic pressure is called the plasma-β and is defined as

$$\beta = \frac{p}{B^2/2\mu_0} = \frac{nk_BT}{B^2/2\mu_0}. \tag{1.3}$$

Here p is the plasma pressure and B is the magnitude of the tokamak magnetic field. This quantity is related to the overall cost of electricity production by tokamak devices since it measures the efficiency of the use of the magnetic field, which is a significant cost of the tokamak design. A high β is desirable since this quantity scales with the plasma pressure. Thus, for a fixed magnetic field (in other words, for a fixed machine cost), a higher β indicates higher plasma density and temperature values, or an increased fusion reaction rate.

In the present thesis we investigate the collisional processes which limit con-

finement in spherical tokamaks, an advanced tokamak design which offers a more compact device than the conventional tokamak, see figure 1.2. In particular we primarily focus on the Mega Ampère Spherical Tokamak (MAST) [Cox and the MAST team, 1999], a relatively large spherical tokamak (ST) device. On key characteristic of a tokamak is the *aspect ratio* of the plasma, that is the ratio of the major to minor radius of the torus. Early tokamak devices were large aspect ratio devices. For example, the Joint European Torus (JET) [Rebut et al., 1985], the largest tokamak currently in operation has, has a minor and major radius of 1.25 m and 2.96 m, corresponding to an aspect ratio of 2.37. The MAST device on the other hand has a minor radius of approximately 0.65 m and a major radius of approximately 0.85 m.

One considerable advantage of spherical tokamaks over conventional tokamaks is that the compact design and tight aspect ratio allows a weaker magnetic field to be used, reducing the cost of such a device for a given amount of heating power. It is well established that spherical tokamaks are able to access high β [Lloyd et al., 2004]. Spherical tokamaks such as MAST have also been demonstrated to exhibit conventional tokamak-like confinement, in agreement with international scaling laws [Gusev et al., 2003]. Thus while ST devices may offer a number of advantages over conventional tokamaks, they follow the same scaling laws as conventional tokamaks and thus share many common properties and characteristics. I will therefore occasionally use the term tokamak to refer to both conventional and spherical tokamaks.

Spherical tokamak plasmas such as MAST tend to be strongly shaped, that is the poloidal cross deviates significantly from the circular cross section of the idealised large aspect ratio tokamak, as depicted in figure 1.2. This strong shaping and access to high-β operating regimes has extended the operating space of tokamaks, providing a stringent test of scaling laws and theories and offered insight into the dependence of physical processes on, for example, the plasma shaping. The impact of MAST and tight aspect ratio on a number of aspects of tokamak physics is reviewed by Lloyd et al. [2004].

1.3 The impact of impurities

The control and removal of impurities from tokamak fusion plasmas is a critical issue for future reactors. By impurities it is meant any ions which are not the reactants for fusion reactions. There exists a maximum permissible impurity concentration above which ignition cannot occur [Hirshman and Sigmar, 1981]. Thus it is critical that impurity levels may be controlled or at the very least limited.

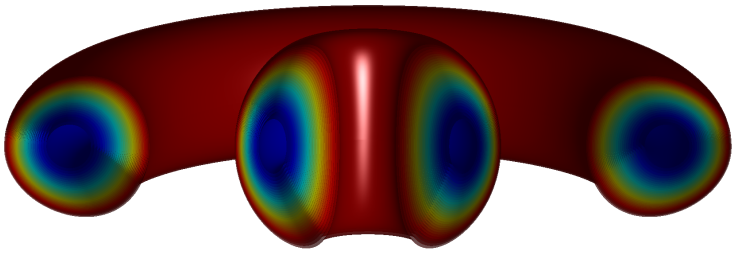

Figure 1.2: Comparison of the aspect ratio of conventional (outer torus) and spherical tokamak (inner torus) plasmas.

There exists two general sources of impurities in tokamak devices. The first is intrinsic to the fusion reactions occurring in the plasma core, that is the fusion-produced α particles. Simply by having fusion reactions occurring we are introducing impurity ions which themselves do not contribute to the production of fusion energy. However, as discussed in the previous section, one aims for a scenario where these α particles are used for self-heating of the plasma. Thus, it is desirable to devise an operational scheme such that α particles remain confined within the plasma just long enough for them to transfer their energy to the deuterium and tritium ions, but are then promptly lost. Once the helium ions have transferred their energy to the fusion plasma, they are referred to as *helium ash*. The presence of helium ash is undesirable for reasons discussed below.

The other source of impurities is the tokamak device itself. At the temperature of a fusion reactor material hitting the tokamak walls (through, for example, disruptions or instabilities of the plasma) sputter wall material into the plasma. We therefore require materials with high charge numbers, Z, which are resistant to sputtering. However, high-Z impurities, when injected into the plasma, are detrimental to plasma performance and so a compromise is necessary.

Impurities present in a fusion plasma affect the reactor performance through enhanced radiation losses and fuel dilution [ITER Physics Basis Editors et al., 1999]. Sputtering of wall material and high-Z elements give rise to partially stripped ions, which in turn give rise to plasma energy loss through enhanced radiation. There are two types of process involved. The first is the enhancement of Bremsstrahlung because of the higher value of the ionic charge for impurities. The second is the radiation which occurs through the atomic processes of line radiation and recombination. The mitigation and control of impurities is therefore vital in reducing these energy losses from fusion tokamak plasmas.

Conversely, impurity ions present in the edge or near the divertor of a tokamak, where there is little fusion energy production, may be beneficial by radiating

thermal energy and thereby mitigating the heat load incident on the divertor and plasma facing components [Murakami et al., 2003]. An understanding of impurity transport (a topic which has received less attention than the transport of bulk ions) is therefore crucial in order to predict the overall performance of fusion plasmas [ITER Physics Basis Editors et al., 1999].

1.4 Thesis overview

In this thesis the role of the radial electric field on the collisional transport of impurity ions in spherical tokamak plasmas is investigated using a full orbit particle code. In chapter 2 a number of important tokamak physics concepts are introduced and discussed. These include tokamak plasma equilibria, the dynamics of charged particles in toroidal magnetic fields and particle confinement and collisional transport in tokamak plasmas. This chapter ends with a brief summary of experimental observations of impurity transport in conventional and spherical tokamaks.

The development and application of the numerical tool used throughout this thesis, the full orbit particle code CUEBIT, is then discussed in chapter 3. Examples of collisionless particle trajectories in tokamak plasmas calculated using CUEBIT are presented and these orbits are tested for correctness using the analytical results of the preceding discussion of charged particle dynamics. The implementation of collisions in CUEBIT is then compared against the standard theory of collisional transport in tokamak plasmas, *neoclassical theory*, in chapter 4.

Having verified the correct expected behaviour of the numerical code and it's suitability for the study of spherical tokamak plasmas, chapter 5 introduces the radial electric field and investigates the modification of the collisional transport of impurity ions due to this field. A scaling of this modification with impurity particle mass and charge numbers is derived analytically and verified numerically and a scaling with electric field parameters is derived numerically. Chapter 6 introduces a time dependency of the radial electric field, which models a number of transient events in tokamak plasmas, and attempts a preliminary comparison between experimental observations of impurity transport on MAST with the results of the CUEBIT code. Finally, in chapter 7 a brief summary of the key results of the present work is given and future plans are outlined.

Chapter 2

Tokamak and plasma physics

> The goal in plasma physics, as in the study of any fluid such as air, water, or liquid helium, is to understand and to control it — to pump, to compress, to heat and extract energy, to propagate waves, to measure and, above all, to keep it from leaking.
>
> Grad, H, *Plasmas*, Physics Today **19**, pp. 34–44, 1969.

2.1 The problem of plasma physics

A plasma is essentially a collection of charged particles, both ions and electrons, interacting self-consistently with one another, via the Coulomb force, and any externally applied electric and magnetic fields. It is this property of collective long-range interactions, of plasma with itself and of plasma with its electromagnetic environment, that gives rise to the great complexity of its behaviour [Post, 1956]. One could, *in principle*, fully describe a plasma and its associated collective modes by considering the motion of each individual charge. The motion of non-relativistic charged particles in electromagnetic fields is governed by the Lorentz force equation,

$$m\frac{\mathrm{d}\mathbf{v}}{\mathrm{d}t} = Ze\left(\mathbf{E} + \mathbf{v} \times \mathbf{B}\right), \tag{2.1}$$

where m, Ze and $\mathbf{v}$ are the mass, charge and velocity of a particle and $\mathbf{E}$ and $\mathbf{B}$ are the electric and magnetic fields experienced by the particle. In order to exactly solve for the motion of a charged particle the dynamics of the fields must also be considered, in other words $\mathbf{E}$ and $\mathbf{B}$ are not static and are in fact influenced by the presence of charged particles. Equation 2.1 must therefore be solved self-consistently

with the evolution of these fields, described by the set of Maxwell's equations:

$$\nabla \cdot \mathbf{E} = \frac{\rho}{\epsilon_0}, \tag{2.2a}$$

$$\nabla \cdot \mathbf{B} = 0, \tag{2.2b}$$

$$\nabla \times \mathbf{E} = -\frac{\partial \mathbf{B}}{\partial t}, \tag{2.2c}$$

$$\nabla \times \mathbf{B} = \mu_0 \mathbf{j} + \mu_0 \epsilon_0 \frac{\partial \mathbf{E}}{\partial t}, \tag{2.2d}$$

which are coupled to particles through the charge density ρ and the current density $\mathbf{j}$. The set of equations 2.1 and 2.2 provides a formally complete description of a plasma. However, the apparent simplicity of the problem, succinctly stated in five equations, belies the hugely complex and varied solutions of the above system. For systems of practical interest, the above system is in fact impossible to solve, since it is not possible (nor desirable) to know the position and velocity of each particle. Thus, much of plasma physics is directed at constructing approximations which make solution of the above equations tractable.

Whilst the approach outlined above is not practical, the dynamics of individual charges and the Lorentz force equation, 2.1, are central to the present work. We can reduce the complexity of the problem by neglecting the self-consistent evolution of particles, that is we assume that the electric and magnetic fields in the problem are externally prescribed and static. This allows us to solve for the exact particle dynamics, in other words find exact solutions to the Lorentz force equation, assuming this stationary electromagnetic environment. We further reduce the complexity of the problem by assuming test particles, that is we follow a species of independent particles which interact with with some prescribed background field or species of particles which is either static or evolves independently of the test particle species.

Alternative particle descriptions exist. Rather than solving the Lorentz force equation, *guiding centre* and *gyrokinetic* theories average over the particle cyclotron period, solving for the trajectories of the averaged, or *guiding centre*, particle position. Averaging out the fastest particle time scale allows one to describe longer time scale phenomenon more easily and allows gyrokinetic codes to simulate the self-consistent dynamics of particles. However, the description of the averaged particle motion relies on an ordering of the particle equation of motion and care must be taken to ensure that the solution has been calculated to a sufficiently high order [Baños, 1967]. The first principles *full orbit* approach, based on the solution of the Lorentz force equation, on the other hand, is rigorously correct and can ultimately be used to verify the ordering and expansion employed in gyrokinetic calculations.

2.2 Plasma equilibrium

The previous chapter introduced the toroidal nature of the confining tokamak magnetic field. This toroidal nature is crucial for achieving plasma confinement. In the present section we demonstrate that toroidal magnetically confined plasmas are viable, in other words that is it possible to form a toroidal plasma equilibrium by the appropriate generation of a magnetic environment, and discuss a tokamak equilibrium model valid for both spherical and conventional tokamaks that is used throughout this thesis.

The full set of equations which describe the long-time behaviour of plasmas, the MHD equations, may be reduced to an equilibrium set of equations, the so-called *magnetostatic equations* [Freidberg, 1987],

$$\mathbf{j} \times \mathbf{B} = \nabla p, \tag{2.3a}$$

$$\nabla \times \mathbf{B} = \mu_0 \mathbf{j}, \tag{2.3b}$$

$$\nabla \cdot \mathbf{B} = 0, \tag{2.3c}$$

by assuming a stationary plasma. Non-stationary equilibria, with a non-zero plasma flow velocity, $\mathbf{v}$, do exist but the effect of toroidal flow, v_φ, on the equilibrium flux surfaces is usually small provided that this rotation is small compared with the bulk plasma ion thermal speed, $v_{\mathrm{th,i}}$, in other words provided that $v_\varphi^2 \ll v_{\mathrm{th,i}}^2$. Toroidal flows in present day conventional tokamaks are generally subsonic, although in MAST higher levels of rotation compared to conventional tokamaks are readily achieved due to the lower moment of inertia of the ST design.

From (2.3a) we have that the condition for equilibrium is for the magnetic force, $\mathbf{j} \times \mathbf{B}$, to balance the pressure gradient force, ∇p. This force balance equation summaries the condition for the existence of a equilibrium plasma configuration. Finding a solution to this equation, in other words forms of $\mathbf{j}$ and $\mathbf{B}$ which balance ∇p, is the aim of the present section.

2.2.1 The problem of toroidal confinement

From the magnetostatic equations above it follows that magnetic induction and current density are everywhere normal to the pressure gradient,

$$\mathbf{B} \cdot \nabla p = 0 \quad \text{and} \quad \mathbf{j} \cdot \nabla p = 0. \tag{2.4}$$

In other words, pressure is constant along lines of both magnetic field and current density. The curve $p = constant$ defines a family of surfaces characterised by the value of the constant. Since, for practical cases, we require that the plasma is confined and isolated from material walls, surfaces of constant pressure must be closed. Additionally, we require that the $\mathbf{j} \times \mathbf{B}$ force nowhere vanishes in order to satisfy the equilibrium force balance. We therefore find, via a well know theorem [Alexandroff and Hopf, 1935], that such surfaces must be a set of nested tori (essentially since any closed surface $p = constant$ divides all space into two regions, inside and out, all such closed surfaces must topologically be similar to a torus). These surfaces are called *flux surfaces*, since they may be uniquely labelled by the poloidal flux function Ψ, this is the magnetic flux passing through a surface of constant poloidal angle bounded by the *magnetic axis* and the magnetic surface of interest. All surfaces contain within them the *magnetic axis*, a unique line which defines the maximum pressure and therefore defines the limiting magnetic surface whose cross-sectional area is zero. It should be noted that there exists two definitions of flux surfaces, one from each of the equations in (2.4). In the following we assume that these sets of surfaces are coincident.

One attractive property of these toroidal surfaces of constant pressure, and a consequence of the aforementioned theorem, is that the fields $\mathbf{B}$ and $\mathbf{j}$ will be non-zero everywhere on the surface, indicating that the $\mathbf{j} \times \mathbf{B}$ force can, in principle at least, everywhere balance the plasma pressure.

We now consider two important consequences of constructing a toroidal plasma and magnetic field structure. The first of these is analogous to the force between parallel current carrying wires. The magnetic field observed at one wire due to current in the other leads to a $\mathbf{j} \times \mathbf{B}$ force which acts to push the wires together. In other words, parallel currents attract each other and, conversely, anti-parallel currents repel each other. If we consider a plasma to be a bundle of parallel current carrying wires in the toroidal direction then there is mutual attraction between each wire, resulting in an effective net force acting to reduce the diameter of the bundle. The bundle could be replaced by a distributed current such as the current carried by a finite-radius, cylindrical plasma. This contracting, inward directed force is called the *pinch force*.

Secondly, at each point on a current carrying loop of wire there is a repulsive force between that point and the point opposite, since current flows in opposite directions on opposing sides of the loop. The result is an outward directed force, called the *hoop force*, which acts to expand the diameter of the loop. The magnetic field lines are more dense on the inside the loop than outside, a purely geometrical

effect resulting from the curvature of the current path. Thus, the magnetic field is stronger on the inside of the loop than on the outside, in other words there is a larger magnetic pressure on the inside of the loop resulting in an outward force. The combined effects of magnetic pressure and tension can be visualised by imagining a current-carrying loop where the conductor has a finite diameter. The hoop force will cause the diameter of the loop to increase while the pinch force will cause the diameter of the conductor to decrease.

These forces may be introduced more rigorously by substituting for the current density, using Ampère's law, (2.3b), in the equation for force balance, (2.3a), which yields

$$\nabla p = \frac{1}{\mu_0} (\nabla \times \mathbf{B}) \times \mathbf{B} = \frac{1}{\mu_0} \left[(\mathbf{B} \cdot \nabla) \mathbf{B} - \nabla \left(\frac{B^2}{2} \right) \right], \tag{2.5}$$

or, expressed as the so called *pressure-balance condition*,

$$\nabla \left(p + \frac{B^2}{2\mu_0} \right) = \frac{1}{\mu_0} (\mathbf{B} \cdot \nabla) \mathbf{B}. \tag{2.6}$$

The right-hand side of the above equation arises from a parallel tension force. The left-hand side of this equation indicates that we consider the magnetic field to have associated with it a *magnetic pressure*, $p_{\mathrm{mag}} = B^2/2\mu_0$. An important figure of merit used when comparing the design of magnetic confinement devices is the *plasma-β*, (1.3), which is defined as the ratio of the kinetic (or plasma) pressure to the magnetic pressure.

The problem of toroidal equilibrium may be considered two-fold. First, the magnetic confinement must provide radial pressure balance, so that in the poloidal plane flux surfaces form closed nested surfaces. Secondly, the configuration must compensate for the outward expansion force inherent in all toroidal plasmas without sacrificing stability [Freidberg, 1982]. This is often achieved by the suitable application of a vertical magnetic field applied so as to reduce the magnetic field on the inboard side of the plasma and increase it on the outboard side, resulting in a balance of magnetic pressure on both sides of the plasma. Alternatively, an appropriate balance of toroidal and poloidal magnetic fields may compensate this expansion force [Freidberg, 1982, Sec. IV].

The existence of analytical solutions to (2.3a), despite its apparent simplicity, has only been demonstrated for symmetric systems; there exists a basic existence problem for the fully three-dimensional, non-symmetric case [Edenstrasser, 1980]. In the next section, we therefore deal only with the relatively simple case of axisym-

metric toroidal plasmas. The problem of toroidal force balance can then be recast into a single equation, the Grad-Shafranov equation, which must be satisfied by any axisymmetric plasma in equilibrium.

2.2.2 The Grad-Shafranov equation

The Grad-Shafranov (GS) equation derives from the MHD equilibrium force balance equation, $\mathbf{j}\times\mathbf{B} = \nabla p$, in coordinate systems with an ignorable coordinate [Shafranov, 1958; Grad and Rubin, 1958; Lust and Schlüter, 1957]. Tokamak plasmas are, to a first approximation, *axisymmetric*, that is symmetric in the toroidal direction. The assumption of axisymmetric allows one to reduce the three equations $\mathbf{j}\times\mathbf{B} = \nabla p$ to a single equation, the GS equation, which in cylindrical coordinates, (R, φ, Z), has the familiar form

$$\Delta^*\Psi \equiv R\frac{\partial}{\partial R}\left(\frac{1}{R}\frac{\partial\Psi}{\partial R}\right) + \frac{\partial^2\Psi}{\partial Z^2} = -\mu_0 R^2\frac{dp}{d\Psi} - \frac{1}{2}\frac{df^2}{d\Psi}, \tag{2.7}$$

where $p = p(\Psi)$ is the plasma pressure, $f = f(\Psi)$ is the poloidal current and $\Delta^* \equiv R^2\nabla\cdot\left(R^{-2}\nabla\right)$ is the elliptic operator. The GS equation is a second order nonlinear, elliptic partial differential equation, whose solutions describe axisymmetric plasma equilibria. The solution to the GS equation, in other words the functional form of $\Psi(R, Z)$, describes the tokamak plasma shape and poloidal magnetic field.

The total tokamak magnetic field is generally written as

$$\mathbf{B} = f(\Psi)\nabla\varphi + \nabla\varphi\times\nabla\Psi = \mathbf{B}_\mathrm{T} + \mathbf{B}_\mathrm{P}, \tag{2.8}$$

with $f = RB_\varphi$ and B_φ the toroidal magnetic field strength. Equation (2.8) is a general result which follows simply from the divergence free nature of the magnetic field vector, $\nabla\cdot\mathbf{B} = 0$, and the assumption of axisymmetry [D'haeseleer et al., 2001]. The toroidal magnetic field, $\mathbf{B}_\mathrm{T}$, is determined by the prescription of $f(\Psi)$ whilst the poloidal magnetic field, $\mathbf{B}_\mathrm{P}$, is determined by the solution of the GS equation, $\Psi(R, Z)$.

2.2.3 Analytic Solov'ev equilibria

Analytic solutions of the Grad-Shafranov equation are used to study plasma equilibrium, MHD stability and transport properties of toroidally axisymmetric fusion devices, both theoretically and numerically. They are also useful for benchmarking MHD equilibrium codes, which solve the GS numerically, for situations where the usual large aspect ratio expansion is not justified [Cerfon and Freidberg, 2010].

The Solov'ev solution to the GS equation [Solov'ev and Shafranov, 1966; Solov'ev, 1968] is a widely used analytic solution which is useful for both numerical and analytic study of tokamak plasmas since it is both simple and yet exact. With this solution we may describe up-down symmetric limited or diverted equilibria (we could also describe up-down asymmetric diverted equilibria, however, these solutions tend to be semi-numerical; in the present work we are concerned only with analytic solutions). The Solov'ev solution, in general, includes the effects of finite aspect ratio, finite beta and a non-circular cross section.

The Solov'ev solution derives from the assumption of a linear right-hand side of the GS equation with the source terms $f(\Psi)$ and $p(\Psi)$ defined as [Solov'ev, 1968]

$$p(\Psi) = p_{\mathrm{e}} + p'\Psi, \tag{2.9a}$$

$$f^2(\Psi) = f_0^2 - 2A\Psi, \tag{2.9b}$$

with $p' < 0$ for physical equilibria. Here a prime denotes a derivative with respect to the poloidal flux, Ψ. With this choice of the source terms the GS equation takes the form

$$\Delta^* \Psi = -\mu_0 p' R^2 + A. \tag{2.10}$$

The choice of the free functions given above has the considerable advantage of making the GS equation a *linear* inhomogeneous partial differential equation.

Derivation of the Solov'ev solution

The usual method of finding a solution to the GS equation is to expand either the homogeneous solution or the full solution as a separable power series, such as

$$\Psi(R, Z) = \sum_{n=0}^{\infty} g_n(R) Z^n \tag{2.11}$$

or similar [Zheng et al., 1996]. In the following we expand the full solution in this way. With this particular form of the solution the second derivative with respect to the vertical coordinate is

$$\frac{\partial^2 \Psi_n}{\partial Z^2} = n(n-1) Z^{n-2} g_n(R) = (n+2)(n+1) Z^n g_{n+2}(R). \tag{2.12}$$

where we have redefined the index n in order to arrive at the final equality. Substituting the expansion above into the GS equation, we have that the solution satisfies

the equations

$$R\frac{d}{dR}\left(\frac{1}{R}\frac{dg_n}{dR}\right) + (n+2)(n+1)g_{n+2} = \begin{cases} -\mu_0 p' R^2 - ff' & \text{if } n = 0, \\ 0 & \text{otherwise ,} \end{cases} \tag{2.13}$$

for each value of n, where we have collected terms proportional to each Z^n. We therefore have a system of ordinary differential equations for each term in the expansion (above), which couple the n and $n+2$ terms of the expansion in the radial coordinate.

In order to find simple analytic solutions to the GS equation we make some simplifying assumptions and truncate the series expansion of our solution. First, we seek solutions which are up-down symmetric, and so only retain even values of n in the expansion above. Up-down asymmetric solutions may be found, but they tend to be more complicated and require a semi-numerical approach to solve the required plasma boundary conditions [Atanasiu et al., 2004; Guazzotto and Freidberg, 2007; Cerfon and Freidberg, 2010]. Secondly, we truncate the expansion of the solution at $n = 2$, in other words we assume that $g_n = 0$ for $n \geqslant 4$. With this truncated expansion of the poloidal flux function the GS equation takes the form

$$R\frac{d}{dR}\left(\frac{1}{R}\frac{dg_0}{dR}\right) + 2g_2 + Z^2 R\frac{d}{dR}\left(\frac{1}{R}\frac{dg_2}{dR}\right) = -\mu_0 p' R^2 - ff'. \tag{2.14}$$

From this equation, we see that the right hand term is independent of Z^2. The term proportional to Z^2 therefore satisfies

$$R\frac{d}{dR}\left(\frac{1}{R}\frac{dg_2}{dR}\right) = 0, \tag{2.15}$$

which is just (2.13) for $n = 2$ and which has solution

$$g_2(R) = c_1 + c_2 R^2. \tag{2.16}$$

We may now solve for g_0 using the $n = 0$ case of (2.13). With

$$R\frac{d}{dR}\left(\frac{1}{R}\frac{dg_0}{dR}\right) = (C - 2c_2)R^2 + A - 2c_1 \tag{2.17}$$

we have that

$$g_0 = \frac{1}{8}(C - 2c_2)R^4 + \frac{1}{4}(A - 2c_1)R^2[2\ln R - 1] + \frac{c_3}{2}R^2 + c_4. \tag{2.18}$$

Here we have introduced $C = -\mu_0 p'$. Combining this with our expression for g_2 we have the solution to the GS equation

$$\Psi(R,Z) = \frac{1}{8}\left(C - 2c_2\right)R^4 + \frac{1}{4}\left(A - 2c_1\right)R^2\left[2\ln R - 1\right] + \frac{c_3}{2}R^2 + c_1 Z^2 + c_2 R^2 Z^2 + c_4. \tag{2.19}$$

This solution describes the geometry of surfaces of constant poloidal flux for up-down symmetric, axisymmetric plasmas. For such plasmas the shape of the poloidal cross section is described by four parameters: the major radius, geometric minor radius, elongation and triangularity (see section 2.2.3), which are related to the constants c_1, c_2, c_3 and c_4. The above solution is the simplest solution which allows one the freedom to specify these four geometric quantities independently [Zheng et al., 1996]. Furthermore, the constants A and C provide two constraints on the toroidal plasma current and poloidal plasma beta figures of merit. Thus this equilibrium model is specified by setting six free parameters: c_1, c_2, c_3, c_4, A and C.

Setting $c_1 = A/2$ we arrive at Solov'ev's original solution

$$\Psi(R,Z) = \frac{1}{8}\left(C - 2c_2\right)R^4 + \frac{c_3}{2}R^2 + c_4 + \frac{A}{2}Z^2 + c_2 R^2 Z^2, \tag{2.20}$$

as used by Freidberg [1987]. This may be easily rewritten in a more useful form as

$$\Psi(R,Z) = C\left\{\frac{\gamma}{8}\left[\left(R^2 - R_0^2\right)^2 - R_b^4\right] + \frac{1}{2}\left[\left(1-\gamma\right)R^2 + \frac{A}{C}\right]Z^2\right\}, \tag{2.21}$$

where we have introduced the new constants R_0, R_b and γ to replace c_2, c_3 and c_4, with these two sets of constants related as follows:

$$c_2 = \frac{1}{2}C\left(1-\gamma\right), \tag{2.22a}$$

$$c_3 = \frac{1}{4}C\gamma R_0^2, \tag{2.22b}$$

$$c_4 = \frac{1}{8}C\gamma\left(R_0^4 - R_b^4\right). \tag{2.22c}$$

Here R_0 is the major radius of the magnetic axis.

With the above Solov'ev solution (2.21) only three independent shaping parameters are free parameters of the model: the major radius, the geometric minor radius and the plasma elongation (these quantities are defined in figure 2.1). The triangularity is, for a given flux surface, a function only of the inverse aspect ratio and so is not a free parameter of the solution above [Zheng et al., 1996; Weening, 1997]. To retain the freedom in the choice of triangularity we must retain the term proportional to $R^2\left(2\ln R - 1\right)$ in the solution. However, throughout the remainder

of this work we continue to neglect this term. Whilst retaining it allows for a more flexible model of axisymmetric tokamak equilibria, the simpler model which neglects this term is easier to manipulate and to use to derive expressions for flux surface averaged quantities and analytic coordinate system transformations.

The constant A, which is often referred to as the *diamagnetic factor*, characterises the modification of the toroidal magnetic field, B_φ, due to poloidal plasma currents and defines the β regime of interest [Cerfon and Freidberg, 2010]. Throughout the following we assume, for simplicity, that A, is zero. This corresponds to operation with a pure vacuum toroidal field $B_\varphi = f_0/R$. Unfortunately, this has the consequence of over constraining the plasma current, I_p, or poloidal beta, β_p, [Zheng et al., 1996]. In other words, by assuming that $A = 0$ we waive the freedom to specify both I_p and β_p independently. Again, we make this assumption for simplicity when working with this equilibrium model. The (toroidal) plasma current and poloidal-β are defined as

$$I_p = \int \mathbf{j} \cdot \nabla\varphi \mathrm{dS}_p \tag{2.23}$$

and

$$\beta_p = \frac{p}{B_p^2/2\mu_0} \tag{2.24}$$

respectively, with the integral taken over the poloidal tokamak cross section.

Geometric properties of the Solov'ev solution

The geometry of the poloidal cross section of a surface of constant poloidal flux is characterised by the three fundamental dimensionless parameters

$$\epsilon = \frac{a_g}{R_g}, \tag{2.25a}$$

$$\kappa = \frac{S}{\pi a_g}, \tag{2.25b}$$

$$\delta = \frac{R_g - R_{Z_\pm}}{a_g}. \tag{2.25c}$$

Here ϵ is the inverse aspect ratio, κ is the plasma elongation in the vertical direction, δ is the plasma triangularity (see figure 2.1) and S is the area of the poloidal cross section.

The poloidal flux function given above is defined such that $\Psi = 0$ characterises the plasma boundary, usually called the *separatrix* or *last closed flux surface*, and $\Psi < 0$ everywhere within the plasma boundary. The major radial extent of the

last closed flux surface (LCFS) along the mid plane occurs when $\Psi = 0$ and $Z = 0$,

$$R_{\pm} = \sqrt{R_0^2 \pm R_b^2}. \tag{2.26}$$

Using standard tokamak notation this corresponds to

$$R_{\pm} = R_g \pm a_g, \tag{2.27}$$

with R_g the geometric major radius and a_g is the geometric minor radius of the plasma boundary. Solving the above relations simultaneously yields

$$R_0 = R_g\sqrt{1+\epsilon^2}, \tag{2.28}$$

in other words the magnetic axis is shifted outboard from the geometric axis, and

$$R_b^2 = 2\epsilon R_g^2 = \frac{2\epsilon R_0^2}{1+\epsilon^2}, \tag{2.29}$$

For convenience we define the parameter

$$\alpha = \frac{2\epsilon}{1+\epsilon^2}. \tag{2.30}$$

Finally we note that [Freidberg, 1987; Weening, 1997]

$$\gamma = \frac{\kappa^2}{1+\kappa^2}, \tag{2.31}$$

with $\kappa = S/\pi a_{\mathrm{g}}$ the plasma elongation.

Generally it is more useful to define a plasma equilibrium in terms of the magnetic axis major radius and poloidal flux value, plasma elongation and inverse aspect ratio of the last closed flux surface, rather than the derived quantities C, R_b and γ. Therefore, we rewrite the Solov'ev solution as

$$\Psi\left(R,Z\right) = \frac{C\kappa^2}{2(1+\kappa^2)}\left[\frac{1}{4}\left(R^2-R_0^2\right)^2 - \frac{\alpha^2 R_0^4}{4} + \frac{R^2Z^2}{\kappa^2}\right]. \tag{2.32}$$

Here we have used that $\kappa^2 = \gamma/(1-\gamma)$. Defining the minimum poloidal flux value, Ψ_0, as that on the magnetic axis,

$$\Psi(R_0,0) = \Psi_0 = -\frac{C\kappa^2}{2(1+\kappa^2)}\frac{\alpha^2 R_0^4}{4} = -\frac{C\gamma R_b^4}{8}, \tag{2.33}$$

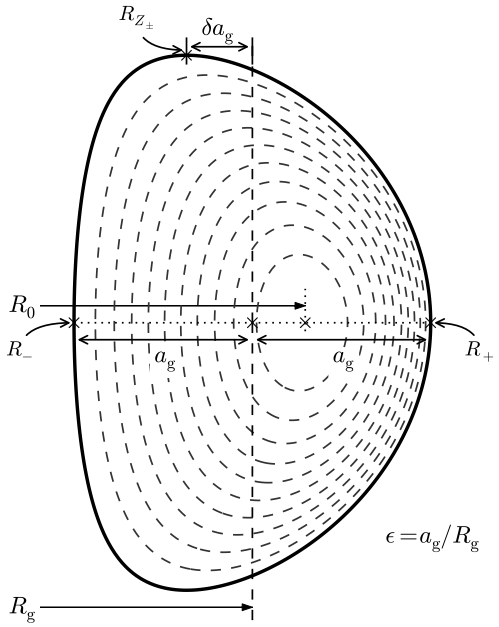

Figure 2.1: Geometric quantities which characterise up-down symmetric tokamak plasmas. Indicated on the figure are: the major radius R_0; the geometric major and minor radii, R_g and a_g respectively; the inverse aspect ratio ϵ; the plasma triangularity δ; the maximum and minimum major radial extent, R_+ and R_- respectively; and the major radius of the maximum vertical extent of the plasma $R_{Z_\pm}$.

we may therefore write the Solov'ev solution as

$$\Psi(R,Z) = -\Psi_0 \left\{ \frac{1}{\alpha^2 R_0^4} \left[\left(R^2 - R_0^2\right)^2 + \frac{4R^2Z^2}{\kappa^2} \right] - 1 \right\}. \tag{2.34}$$

Introducing the normalised poloidal flux $\psi = 1 - \Psi/\Psi_0$, with $\psi \in [0,1]$, we may write

$$\psi(R,Z) = 1 - \frac{\Psi}{\Psi_0} = \frac{1}{\alpha^2 R_0^4} \left[\left(R^2 - R_0^2\right)^2 + \frac{4R^2Z^2}{\kappa^2} \right]. \tag{2.35}$$

Thus the magnetic surfaces, figure 2.2, are completely determined by the specification of four free parameters: R_0, ϵ, κ and C: the major radius of the magnetic axis, the inverse aspect ratio, the elongation and pressure gradient constant respectively. Here R_0, ϵ and κ determine the shape of the flux surfaces whilst C sets the depth of the potential well through Ψ_0.

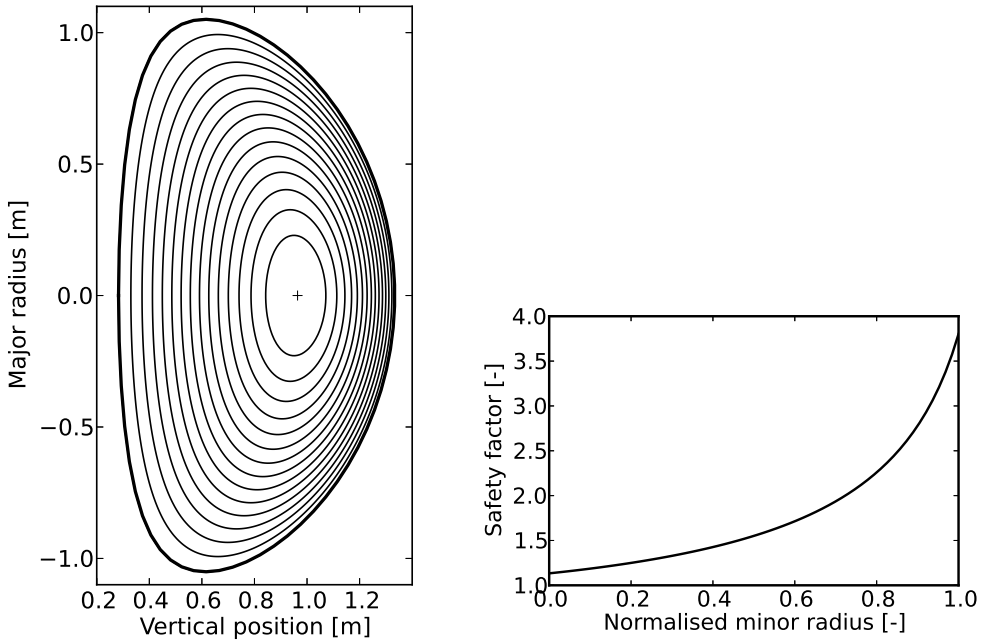

Figure 2.2: Surfaces of constant poloidal flux for a MAST-like equilibrium (left), approximated using the Solov'ev solution to the Grad-Shafranov equation with $R_0 = 0.964$, $\kappa = 2$ and $\epsilon = 0.645$, and corresponding safety factor profile (right). In the left-hand figure the plasma separatrix is indicated by a thicker solid line and the magnetic axis is indicated by a cross (+).

Limitations of the Solov'ev solution

We finish this section by noting a number of limitations of the Solov'ev solution derived above. Firstly, the Solov'ev solution has finite pressure gradient and current density at the plasma edge, thus the solution is characterized by finite jumps of pressure gradient and plasma current at the plasma surface [Guazzotto and Freidberg, 2007]. One must use profiles which are quadratic in Ψ instead to give [Atanasiu et al., 2004; Guazzotto and Freidberg, 2007] zero current and zero pressure gradient at the plasma surface.

The Solov'ev equilibrium solution above is, as already mentioned, over-constrained in β_p, which is determined by the choice of plasma current, and triangularity, which is determined by the choice of aspect ratio. More complicated Solov'ev models lift this limitation [Weening, 2000].

Furthermore, in the limit of large aspect ratio the Solov'ev solution does not display a significant variation in the safety factor (unlike in the case of tight aspect ratio, see figure 2.2), which is a measure of the ratio of toroidal to poloidal magnetic

field strength, with minor radius. Thus this solution is more suited for ST studies [Freidberg, 1987]. This limitation often makes it difficult to fit the Solov'ev model to experimentally determined plasma equilibria.

Finally, one limitation of the previous discussion of the GS equation, not specifically of the Solov'ev solution derived, is that plasma rotation has been neglected. We have derived and used the Grad-Shafranov equation for stationary plasma equilibrium, which describe *static equilibria*. However, tokamak experiments often use rotation in order to improve plasma confinement. In order to derive equilibrium solutions in this case one must retain the inertia terms in the fluid momentum balance equation (force balance equation), which then reads

$$\rho \frac{d\mathbf{v}}{dt} = -\nabla p + \mathbf{v} \times \mathbf{B}, \tag{2.36}$$

where ρ is the plasma mass density. This has the effect of introducing a centrifugal force which acts in the direction away from the axis of rotation.

2.3 Charged particle dynamics

Since, as noted at the start of this chapter, a plasma is essentially a collection of charged particles interacting self-consistently with one another and any externally applied electric and magnetic fields, single particle dynamics is the most fundamental description of a plasma. Whilst this approach is not practical for describing real macroscopic-sized plasmas, the study of single particle motion can yield valuable insight into the confinement and transport of particles in the complicated geometry of a tokamak.

In the following sections, the motion of charged particles in externally applied electric and magnetic fields are derived and the trajectories of such particles in the magnetic field of a tokamak are discussed. For the present discussion the self-fields of the particles are neglected.

2.3.1 Charged particle Lagrangian in electromagnetic fields

In the following sections, the dynamics of a charged particle in an electromagnetic field is derived and discussed using a non-canonical Lagrangian formalism. Such a formalism allows us to derive a number of important results of charged particle dynamics using a unified framework and more quickly than directly from the Lorentz

force equation. For a particle of mass m and charge Ze in an electromagnetic field

$$\mathbf{B} = \nabla \times \mathbf{A}, \tag{2.37a}$$

$$\mathbf{E} = -\nabla\Phi - \frac{\partial \mathbf{A}}{\partial t}, \tag{2.37b}$$

with Φ the electrostatic potential and $\mathbf{A}$ the magnetic vector potential, the Lagrangian of the particle is

$$\mathcal{L}\left[\mathbf{q}(t)\right] = \mathcal{L}\left(\mathbf{q}, \dot{\mathbf{q}}, t\right) = \frac{1}{2} m |\dot{\mathbf{q}}|^2 + Ze\mathbf{A}(\mathbf{q}, t) \cdot \dot{\mathbf{q}} - Ze\Phi(\mathbf{q}, t), \tag{2.38}$$

a function of generalised position $\mathbf{q}(t)$, generalised velocity $\dot{\mathbf{q}}(t)$ and time t. The equations of motion for a particle in such an electromagnetic field are found by substituting the above Lagrangian into the Euler-Lagrange equations,

$$\frac{d}{dt}\left(\frac{\partial \mathcal{L}}{\partial \dot{\mathbf{q}}}\right) = \frac{\partial \mathcal{L}}{\partial \mathbf{q}}, \tag{2.39}$$

which are derived by demanding that the action, that is the path integral of the Lagrangian, is stationary with respect to variation of the path. This is the *principle of stationary action* [Landau and Lifshitz, 1976], which is central to Hamiltonian and Lagrangian mechanics.

In general, given a Lagrangian $\mathcal{L}(\mathbf{q}, \mathbf{q}, t)$, the corresponding *Hamiltonian* is defined as

$$\mathcal{H}\left(\mathbf{q}, \mathbf{p}, t\right) \equiv \mathbf{p} \cdot \dot{\mathbf{q}} - \mathcal{L}\left(\mathbf{q}, \dot{\mathbf{q}}, t\right), \tag{2.40}$$

where the generalised momentum $\mathbf{p}$ is used in favour of $\mathbf{q}$. Given the Lagrangian in (2.38), we have that

$$\mathbf{p} = \frac{\partial \mathcal{L}}{\partial \dot{\mathbf{q}}} = m\dot{\mathbf{q}} + Ze\mathbf{A}\left(\mathbf{q}, t\right), \tag{2.41}$$

which I shall refer to as the canonical momentum.

The Lagrangian formalism is said to be coordinate independent. That is, the action integral may be calculated in any coordinate system, and the principle of stationary action that determines the trajectories may be stated without reference to any particular set of coordinates. This property of the Lagrangian formalism allows one to find easily the dynamical equations in new, more convenient coordinates.

We therefore transform to a *phase-space Lagrangian*, by specifying the phase space coordinates $\mathbf{z} = \{\mathbf{r}, \mathbf{v}\}$, where $\mathbf{r}$ is the particle position and $\mathbf{v}$ is the particle

velocity, related to the canonical coordinates $\{\mathbf{q}, \mathbf{p}\}$ through

$$\mathbf{r} = \mathbf{q}, \tag{2.42a}$$

$$\mathbf{v} = (\mathbf{p} - Ze\mathbf{A})/m. \tag{2.42b}$$

In these coordinates we have the phase-space Lagrangian

$$\mathcal{L}(\mathbf{z}, \dot{\mathbf{z}}, t) = m\mathbf{v} \cdot \dot{\mathbf{r}} - \frac{1}{2}m|\mathbf{v}|^2 + Ze\mathbf{A}(\mathbf{r}, t) \cdot \dot{\mathbf{r}} - Ze\Phi(\mathbf{r}, t). \tag{2.43}$$

It is important to note that the variation of all six phase-space coordinates are independent during the variational process, even if a functional dependence should emerge from the equations of motion. This is because the variational process selects the physical motion from all possible motions, as to make the action stationary. So although, for example, $\mathbf{v} = \dot{\mathbf{r}}$ on the physical path of the particle, this will not be true along all conceivable paths through phase-space.

The equations of motion of the particle now follow from the Euler-Lagrange equations, which, in the phase space coordinates $\mathbf{z}$, become

$$\frac{d}{dt}\left(\frac{\partial \mathcal{L}}{\partial \dot{\mathbf{r}}}\right) = \frac{\partial \mathcal{L}}{\partial \mathbf{r}}, \tag{2.44a}$$

$$\frac{d}{dt}\left(\frac{\partial \mathcal{L}}{\partial \dot{\mathbf{v}}}\right) = \frac{\partial \mathcal{L}}{\partial \mathbf{v}}. \tag{2.44b}$$

From the phase space Euler-Lagrange equations for the velocity variable we have that $\dot{\mathbf{r}} = \mathbf{v}$, since $\partial\mathcal{L}/\partial\dot{\mathbf{v}} = 0$. From the remaining Euler-Lagrange equations we have that

$$\frac{d}{dt}(m\dot{\mathbf{r}} + Ze\mathbf{A}) = Ze\nabla(\mathbf{A} \cdot \dot{\mathbf{r}} - \Phi). \tag{2.45}$$

Evaluating this explicitly, noting that $\nabla(\mathbf{A} \cdot \dot{\mathbf{r}}) = \dot{\mathbf{r}} \times (\nabla \times \mathbf{A}) + (\dot{\mathbf{r}} \cdot \nabla)\mathbf{A}$ and that the left-hand side of the above equation is $m\ddot{\mathbf{r}} + Ze(\partial\mathbf{A}/\partial t + \dot{\mathbf{r}} \cdot \nabla\mathbf{A})$, we find

$$m\dot{\mathbf{v}} = Ze(\mathbf{E} + \dot{\mathbf{r}} \times \mathbf{B}), \tag{2.46}$$

or the Lorentz force on a charged particle, after the identification $\dot{\mathbf{r}} = \mathbf{v}$ has been made. This verifies the correctness of the phase-space Lagrangian introduced above.

2.3.2 Guiding centre motion

Despite the apparent simplicity of the equation of motion above, rigorous derivation of the trajectories of charged particles in a non-uniform magnetic field is a formidable

task, with exact solutions known only in a few simple cases [Vekstein et al., 2002]. Fortunately, in both laboratory plasma physics and in astrophysical plasmas, the non-uniformity of the magnetic field may be considered as being weak, in the sense that the gradient length scale of the magnetic field is large compared with the characteristic size of the plasma. In this case, an approximate description of charged particle motion known as the *guiding-centre* or *drift* approximation may be derived [Alfvén, 1940; Northrop, 1963; Littlejohn, 1983; Cary and Brizard, 2009].

A large part of the analysis of any dynamical system is a search for variables in which the motion is simplified. In the guiding centre approximation, a transformation is made in order to eliminate the rapid gyro motion from the particle equations of motion [Cary and Littlejohn, 1983]. The guiding centre transform decomposes particle motion into a fast, nearly circular gyro motion and a slower evolution of the particle *guiding centre*, that is the gyro-averaged position of the particle, see figure 2.3. The trajectory of the guiding centre evolves on a much longer time scale owing to the non-uniformity of the field than the fast gyro motion. The equations of motion of a particle guiding centre are now derived.

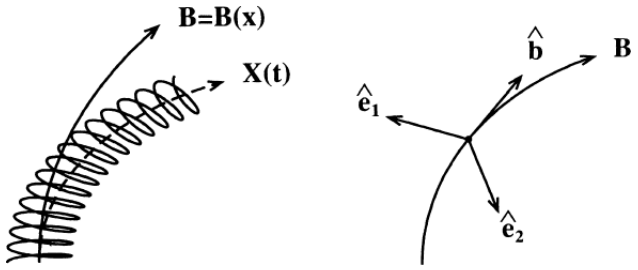

Figure 2.3: Charged particle motion in a non-uniform magnetic field. Left: in a non-uniform magnetic field a particle guiding centre drifts away from a magnetic field line. Right: field of orthonormal triads used to describe particle position [Littlejohn, 1988].

The guiding centre transform

The goal of the guiding centre transform is to introduce a transformation such that the Lagrangian for the guiding centre variables ($\mathbf{R}$, $v_\parallel$, $v_\perp$, ϑ) has an ignorable gyrophase ϑ and thus an associated constant of motion (via Noether's theorem, see, for example, [Landau and Lifshitz, 1976]). Here the guiding centre coordinates ($\mathbf{R}$, $v_\parallel$, $v_\perp$) are the guiding centre position and parallel and perpendicular velocities respectively. In the following we sketch, rather than rigorously perform, the derivation of the guiding centre motion.

In a uniform and constant magnetic field a charged particle will gyrate about a magnetic field line whilst moving freely along it. This gyro motion has a radius $\rho = v_\perp/\Omega$ and frequency $\Omega = ZeB/m$. The guiding centre of this particle,

$$\mathbf{R} = \mathbf{r} - \frac{1}{\Omega}\mathbf{b} \times \mathbf{v}, \tag{2.47}$$

will remain on the same field line moving only parallel to that line:

$$\dot{\mathbf{R}} = v_\parallel \mathbf{b}, \tag{2.48}$$

where $\mathbf{b} = \mathbf{B}/B$. This may easily be demonstrated: differentiating the above equation for the guiding centre position we have, using the Lorentz force equation (2.1) and assuming zero electric field,

$$\dot{\mathbf{R}} = \dot{\mathbf{r}} - \frac{1}{\Omega}\mathbf{b} \times \dot{\mathbf{v}} = \mathbf{v} - \frac{1}{\Omega}\mathbf{b} \times \left(\frac{Ze}{m}\mathbf{v} \times \mathbf{B}\right) = \mathbf{v} - \mathbf{b} \times (\mathbf{v} \times \mathbf{b}) \,. \tag{2.49}$$

Using the vector triple product $(\mathbf{A} \times \mathbf{B}) \times \mathbf{C} = \mathbf{B}\,(\mathbf{A} \cdot \mathbf{C}) - \mathbf{A}\,(\mathbf{B} \cdot \mathbf{C})$, we find

$$\dot{\mathbf{R}} = \mathbf{v} + \mathbf{b}\,(\mathbf{v} \cdot \mathbf{b}) - \mathbf{v}\,(\mathbf{b} \cdot \mathbf{b}) = v_\parallel \mathbf{b}. \tag{2.50}$$

This is the basis of magnetic confinement: in uniform magnetic fields charged particles are constrained to follow a magnetic field line (to within a Larmor radius) but cannot move across the field (although clearly collisions will change the guiding centre position, by an amount $\Delta\mathbf{R} = -\Omega^{-1}\mathbf{b} \times \Delta\mathbf{v}$, and particles can then be transported across the field).

If, however, the magnetic field is non-uniform, then the particle guiding centre is no longer restricted to move purely parallel to a particular magnetic field line. Guiding centre theory aims to describe the modifications to the above result, (2.50), due to a non-uniform magnetic field.

Under the guiding centre approximation, in which we assume a magnetic field that varies over length scales larger than the Larmor radius, we expect (motivated by the case of constant, uniform magnetic field) that the motion of a charged particle consists of a rapid gyro motion and a slower drift motion, so that we may write

$$\mathbf{r} = \mathbf{R} + \boldsymbol{\rho}, \tag{2.51}$$

with the gyro motion described by

$$\boldsymbol{\rho} = \rho\,(\mathbf{e}_1 \cos\vartheta + \mathbf{e}_2 \sin\vartheta)\,, \tag{2.52}$$

and the drift motion described by the time variation of $\mathbf{R}$. Here $\mathbf{e}_1$ and $\mathbf{e}_2$ are unit vectors perpendicular to the magnetic field which form an orthogonal triplet with $\mathbf{b}$, in other words $\mathbf{b} \cdot \mathbf{e}_1 \times \mathbf{e}_2 = 1$ (see figure 2.3). Furthermore, we decompose the particle velocity as

$$\mathbf{v} = u\mathbf{b} + w\mathbf{c} \tag{2.53}$$

with $\mathbf{c} = -\sin\vartheta\mathbf{e}_1 - \cos\vartheta\mathbf{e}_2$ [the instantaneous particle gyrophase is implicitly defined by this expression and (2.52)].

The derivation of guiding centre motion, as pioneered by Littlejohn [1983], is reviewed by Cary and Brizard [2009]. This method consists of an order by order expansion in particle position of the Lagrangian, using (2.51) and (2.53), at each step adding exact time derivatives to the particle Lagrangian in order to produce an appropriate simplification at that order. In the case of guiding centre motion, this simplification is the elimination of the fast gyro motion. Exact time derivatives do not change the equations of motion derived from that Lagrangian [Littlejohn, 1983]. This method is capable of producing the correct guiding centre expressions to all orders in the gyroradius [Cary and Brizard, 2009]. Previous methods, for example that of Northrop [1963], which did not derive from a Lagrangian or Hamiltonian formalism but instead attempted to average the Lorentz equation directly, had a number of short comings (the derived equations of motion did not conserve, for example, phase-space volume or an appropriate energy invariant [Baños, 1967; Cary and Brizard, 2009]), which are avoided using Littlejohn's method.

The result of performing the guiding centre transform to first order in the particle gyroradius is the guiding centre Lagrangian [Littlejohn, 1983]

$$\mathcal{L}_{\mathrm{gc}}\left(\mathbf{R}, u, \mu, \vartheta; t\right) = mu\mathbf{b} \cdot \dot{\mathbf{R}} - \frac{mu^2}{2} - \mu B + Ze\mathbf{A} \cdot \dot{\mathbf{R}} - Ze\Phi + J\dot{\vartheta}, \tag{2.54}$$

or

$$\mathcal{L}_{\mathrm{gc}}\left(\mathbf{R}, u, \mu, \vartheta; t\right) = mu\mathbf{b} \cdot \dot{\mathbf{R}} + J\dot{\vartheta} - \mathcal{H}_{\mathrm{gc}}, \tag{2.55}$$

where we have introduced the *gyroaction* variable $J \equiv m\mu/Ze$ and the guiding centre Hamiltonian $\mathcal{H}_{\mathrm{gc}}$. Furthermore, we have replaced the perpendicular velocity, w, with the *magnetic moment* $\mu = mw^2/2B$. Here the electric and magnetic fields and the magnetic and scalar potentials are evaluated at the guiding centre position, $\mathbf{R}$.

Guiding centre equations of motion

From the Lagrangian (2.54) and the Euler-Lagrange equations it is straightforward to derive the equations of motion of the guiding-centre. Here we begin to arrive at a number of important results and our rewards for utilising a Lagrangian formalism.

First, the Euler-Lagrange equation for the variable ϑ yields

$$\frac{d}{dt}\left(\frac{\partial \mathcal{L}_{\rm gc}}{\partial \dot{\vartheta}}\right) = \frac{\partial \mathcal{L}_{\rm gc}}{\partial \vartheta} \quad \rightarrow \quad \dot{J} = 0. \tag{2.56}$$

Thus the gyroaction (or, equivalently, the magnetic moment, μ) is conserved by the guiding centre equations of motion (this is obvious when one considers Noether's theorem, since the gyrophase ϑ is an ignorable coordinate: only its time derivative appears in the guiding centre Lagrangian [Cary and Brizard, 2009]).

Secondly, the Euler-Lagrange equation for the variable μ (or equivalently J) yields

$$\frac{d}{dt}\left(\frac{\partial \mathcal{L}_{\rm gc}}{\partial \dot{\mu}}\right) = \frac{\partial \mathcal{L}_{\rm gc}}{\partial \mu} \quad \rightarrow \quad \dot{\vartheta} = \Omega \tag{2.57}$$

This is an expected result, indicating that a positively charged particle will gyrate with a left-handed screw along a magnetic field line. If one is concerned only with the motion of the particle's guiding centre and not the evolution of its gyrophase then the term linear in $\dot{\vartheta}$ may be dropped from the guiding centre Lagrangian, since it does not affect the equations of motions of the variables $\mathbf{R}$ and u. Conversely, the adiabatic invariant μ does appear in these equations, as we shall see below, but only as a guiding centre dynamical parameter [Cary and Brizard, 2009].

The Euler-Lagrange for the variable u yields

$$\frac{d}{dt}\left(\frac{\partial \mathcal{L}_{\rm gc}}{\partial \dot{u}}\right) = \frac{\partial \mathcal{L}_{\rm gc}}{\partial u} \quad \rightarrow \quad 0 = m\mathbf{b}\cdot\dot{\mathbf{R}} - mu. \tag{2.58}$$

Thus the guiding centre Lagrangian (2.54) tells us that $u \equiv \mathbf{b}\cdot\dot{\mathbf{R}}$ is the velocity of the guiding centre in the direction of the magnetic field (evaluated at the guiding centre position).

Finally, all that is left to calculate are the equation of motion for the guiding centre position, $\mathbf{R}$. The left-hand side of this Euler-Lagrange equation is

$$\begin{aligned}\frac{d}{dt}\left(\frac{\partial \mathcal{L}_{\rm gc}}{\partial \dot{\mathbf{R}}}\right) &= \left(\frac{\partial}{\partial t} + \dot{\mathbf{R}}\cdot\nabla\right)\frac{\partial \mathcal{L}_{\rm gc}}{\partial \dot{\mathbf{R}}} \\ &= m\dot{u}\mathbf{b} + mu\left(\frac{\partial}{\partial t} + \dot{\mathbf{R}}\cdot\nabla\right)\mathbf{b} + Ze\left(\frac{\partial}{\partial t} + \dot{\mathbf{R}}\cdot\nabla\right)\mathbf{A},\end{aligned} \tag{2.59}$$

and the right-hand side may be shown to be

$$\frac{\partial \mathcal{L}_{\rm gc}}{\partial \mathbf{R}} = mu\left[(\dot{\mathbf{R}}\cdot\nabla)\mathbf{b} + \dot{\mathbf{R}}\times(\nabla\times\mathbf{b})\right] + Ze\left[(\dot{\mathbf{R}}\cdot\nabla)\mathbf{A} + \dot{\mathbf{R}}\times\nabla\times\mathbf{A}\right] - \mu\nabla B - Ze\nabla\Phi, \tag{2.60}$$

using the vector identity $\nabla(\mathbf{C}\cdot\mathbf{X}) = (\mathbf{C}\cdot\nabla)\mathbf{X} + \mathbf{C}\times(\nabla\times\mathbf{X})$, with $\mathbf{C}$ a constant. Note that we have used the following in deriving (2.59):

$$\frac{\partial}{\partial\dot{\mathbf{R}}}(\mathbf{b}\cdot\dot{\mathbf{R}})^2 = \frac{\partial}{\partial\dot{\mathbf{R}}}\left[(\mathbf{b}\cdot\dot{\mathbf{R}})(\mathbf{b}\cdot\dot{\mathbf{R}})\right] = 2u\mathbf{b}. \tag{2.61}$$

Therefore, the equation of motion for the guiding centre is

$$m\dot{u}\mathbf{b} = Ze(\mathbf{E} + \dot{\mathbf{R}}\times\mathbf{B}) - \mu\nabla B + mu\dot{\mathbf{R}}\times(\nabla\times\mathbf{b}) - mu\frac{\partial\mathbf{b}}{\partial t}. \tag{2.62}$$

Parallel dynamics

The parallel dynamics of the particle are found by taking the parallel component of (2.62), which yields

$$m\dot{u} = ZeE_{\parallel} - \mu\mathbf{b}\cdot\nabla B - mu\mathbf{b}\cdot\frac{\partial\mathbf{b}}{\partial t}. \tag{2.63}$$

The final term on the right-hand side of this equation is small compared with the electric field term [Helander and Sigmar, 2002] and is therefore neglected herein. The remaining terms in the equation accelerate and de-accelerate the particle along the magnetic field respectively. The parallel gradient of the magnetic field term is called the *mirror force* and is responsible for particle trapping in tokamak plasmas (see below).

Perpendicular dynamics

The perpendicular dynamics of the particle guiding centre are found by taking the vector product of (2.62) with $\mathbf{b}$. Noting that $\mathbf{b}\times(\dot{\mathbf{R}}\times\mathbf{B}) = (\mathbf{b}\cdot\mathbf{B})\dot{\mathbf{R}} - (\mathbf{b}\cdot\dot{\mathbf{R}})\mathbf{B} = B\dot{\mathbf{R}}_{\perp}$ we find that

$$\dot{\mathbf{R}}_{\perp} = \frac{\mathbf{E}\times\mathbf{B}}{B^2} + \frac{m\mu}{ZeB}\mathbf{b}\times\nabla B - \frac{mu^2}{ZeB}\mathbf{b}\times\left[\dot{\mathbf{R}}\times(\nabla\times\mathbf{b})\right]. \tag{2.64}$$

By approximating $\dot{\mathbf{R}}$ by $u\mathbf{b}$ the above expression may be rewritten in the familiar form

$$\dot{\mathbf{R}}_{\perp} = \frac{\mathbf{E}\times\mathbf{B}}{B^2} + \frac{mu_{\perp}^2}{2\Omega}\mathbf{b}\times\nabla\ln B + \frac{u^2}{\Omega}\mathbf{b}\times\kappa. \tag{2.65}$$

Here we have used that $B^{-1}\nabla B = \nabla \ln B$ and introduced the magnetic field curvature $\kappa = -\mathbf{b} \times (\nabla \times \mathbf{b})$. This result demonstrates that the particle guiding centre drifts across a strong magnetic field due to three forces. They are, in the order they appear in the above equation from left to right, the $\mathbf{E} \times \mathbf{B}$ drift, the *grad-B* drift and the *curvature* drift. The consequences of these drifts are discussed in the following section.

Conserved quantities

In addition to the above equations of motion, the Lagrangian formalism allows us to gain additional insight into the dynamics of charge particles. First, the particle Hamiltonian is conserved in Hamiltonian theory [Cary and Brizard, 2009], which implies, from (2.40), that the total particle energy,

$$\xi = \frac{mv^2}{2} + Ze\Phi \tag{2.66}$$

with v the total particle velocity, is a constant of the particle motion for time independent magnetic and electric fields.

Furthermore, in tokamak plasmas that have an ignorable direction (or direction of symmetry) there is an additional exact constant of the particle motion: the particle *toroidal canonical momentum*. From the toroidal Euler-Lagrange equation,

$$\frac{\mathrm{d}}{\mathrm{d}t}\left(\frac{\partial \mathcal{L}}{\partial \dot{\varphi}}\right) = \frac{\partial \mathcal{L}}{\partial \varphi}, \tag{2.67}$$

it is clear that if the particle Lagrangian does not depend on the toroidal angle, in other words if the electric and magnetic fields do not depend on this angle, then the toroidal canonical momentum [see (2.41)]

$$P_\varphi = \frac{\partial \mathcal{L}}{\partial \dot{\varphi}} \tag{2.68}$$

is a constant of the motion. This is true for both the particle and guiding centre Lagrangians. For the full particle Lagrangian we have, using $RA_\varphi = -\Psi$ [D'haeseleer et al., 2001],

$$P_\varphi = mRv_\varphi - Ze\Psi, \tag{2.69}$$

whereas the equivalent guiding centre constant of motion is

$$P_\varphi^{\mathrm{GC}} = mRub_\varphi - Ze\Psi. \tag{2.70}$$

2.3.3 Particle confinement and drifts in tokamaks

From the guiding centre equations above we can see that the effect of spatial variations in the magnetic field is to cause a modification of the parallel velocity of the guiding centre and drifts of the guiding centre position perpendicular to the magnetic field. The parallel and drift forces are the reason for the complexity of the orbits of charged particles in tokamak plasma, which we presently investigate. One immediate consequence of these drift is eloquently summarised by Spitzer [1967]:

> The crucial effects of field variation are particle trapping and the gradient-B and curvature drifts of gyrating particles across field lines, resulting from gradual distortion of the Larmor orbit. Thus the magnetic inhibition of free particle motion... has complementary weakness. Because it provides localization of charged particles in only two dimension, it requires a toroidal system for confinement; but the field curvature resulting from toroidicity leads to perpendicular drifts, i.e., to a weakening of the original inhibition.

So while we require closed magnetic field lines to confine charged particles, by requiring a toroidal magnetic field we allow the charged particles to drift across the otherwise confining field. In tokamak plasmas, these drifts can cause particles to travel far from their initial flux surface, which leads to large cross-field energy and particle transport described by *neoclassical transport theory*, a prominent result of this weaknesses, which is discussed in the next section.

As derived in the previous sections particle motion in toroidal, axisymmetric magnetic fields is characterised by three constants of their motion

$$\xi = \frac{mv^2}{2} + Ze\Phi \tag{2.71a}$$

$$\mu = \frac{mv_\perp^2}{2B} \tag{2.71b}$$

$$P_\varphi = mRv_\varphi - Ze\Psi \tag{2.71c}$$

(μ is actually an *adiabatic invariant*). A particle cannot enter a region where the magnetic field is such that $\mu B > \xi - Ze\Phi$, since this would imply that $v_\perp > v$ and $v_\parallel^2 = (2/m)(\xi - \mu B - Ze\Phi) < 0$, which is clearly non-physical. This indicates that there may be regions of strong magnetic field from which certain particles are excluded.

Introducing the pitch-angle variable

$$\lambda = \frac{\mu B_0}{mu^2/2} = \frac{v_\perp^2}{v^2}\frac{B_0}{B}, \tag{2.72}$$

with B_0 some normalising magnetic field, usually taken to be $\left\langle B^2 \right\rangle^{1/2}$, where angular brackets denote the *flux surface average*. In a tokamak, the magnetic field varies from a value of $B_{\min}$ on the outboard side to $B_{\max}$ on the inboard side. Thus, all particles must satisfy the condition

$$0 \leqslant \lambda \leqslant \frac{B_0}{B_{\min}}, \tag{2.73}$$

since the minimum value of λ occurs when $v_\perp = 0$ and the maximum value of λ occurs when $v_\parallel = 0$ and $B = B_{\min}$. However, a subset of particles exist for which

$$\frac{B_0}{B_{\max}} < \lambda \leqslant \frac{B_0}{B_{\min}}, \tag{2.74}$$

For these particles, their parallel velocity reaches zero at some point along their orbit. Those particles satisfying the above condition are restricted to the outboard side of a flux surface. In other words, there exists a region on a flux surface which certain particles cannot enter because the magnetic field strength is sufficiently strong that the magnetic mirror force of section 2.3.2 is able to reduce, and ultimately reverse, the sign of the particle's parallel velocity. Such particles are referred to as *trapped* particles. The turning points of the particle orbit are called *bounce points*.

Furthermore, there exists a class of particles for which

$$0 \leqslant \lambda \leqslant \frac{B_0}{B_{\max}}. \tag{2.75}$$

These particles are free to explore the entire flux surface. The magnetic mirror force acts to slow down these particles, however, not enough to reflect them. These particles are referred to as *passing* or *circulating* particles.

An illustration of the poloidal projections of these two main classes of particle orbit in tokamak plasmas is presented in figure 2.4. We see that passing particle orbits enclose the magnetic axis, whereas trapped particles are localised on the outboard side of the tokamak and are limited in poloidal angle. The extreme poloidal angles of a trapped particle orbit occur when the particle is reflected by the magnetic mirror force, in other words when the parallel parallel velocity is zero.

From the particle trapping condition (above) we have the lower bound on the particle pitch angle parameter $\lambda > B_0/B_{\max}$, with $B_{\max}$ the maximum magnetic field experience by the particle (not the maximum magnetic field on the local flux surface). For a large aspect ratio tokamak with circular, concentric magnetic flux surfaces we have that the toroidal magnetic field may be written

$$B(r) = \frac{R_0 B_0}{R} = \frac{B_0}{1 + \epsilon \cos\theta} = B_0 \left(1 - \epsilon \cos\theta\right), \tag{2.76}$$

with r the minor radius, θ the poloidal angle and $\epsilon = r/R_0$ the inverse aspect ratio of the torus. From the lower bound on the trapped particle condition we have that $\theta_b < \pm\pi$, since $v_\parallel = 0$ at the particle bounce points. It may be shown from (2.63) that the equation of motion for a *deeply trapped* particle along a magnetic field line, given the magnetic field above, is [Wesson, 2004]

$$\frac{d^2 s}{dt^2} = -\frac{1}{2}\frac{v_\perp^2}{q}\frac{r}{R_0^3} s = -\omega_b^2 s, \tag{2.77}$$

with s the distance along a magnetic field line and q the tokamak safety factor. Thus a deeply trapped particle undergoes simple harmonic motion between the poloidal angles $\pm\theta_b$ with a *bounce frequency* ω_b. In this deeply trapped limit it may also be shown that [Wesson, 2004]

$$\theta_b = \frac{v_{\parallel,0}}{v_{\perp,0}} 2\epsilon^{-1/2}. \tag{2.78}$$

Thus the smaller the angle $v_{\parallel,0}/v_{\perp,0}$ the shorter the trajectory between bounce points. Here the subscript zero indicates a value of the particle velocity evaluated at the location of the minimum magnetic field.

The constancy of toroidal angular momentum, P_φ, implies that a particle must drift across flux surfaces during an orbit, as illustrated by figure 2.4: since P_φ remains constant, changes in the particle toroidal velocity, v_φ, due to the variation of the magnetic field and forces across the particle orbit, must lead to changes in Ψ. Comparing the relative magnitude of the two terms in P_φ we have

$$\frac{mRv_\varphi}{Ze\Psi} \sim \frac{mv_\varphi}{ZerB_\mathrm{p}} \sim \frac{\rho_\mathrm{p}}{r}. \tag{2.79}$$

Here $\rho_\mathrm{p} = mv_\varphi/ZeB_\mathrm{p}$ is the poloidal Larmor radius. In order to arrive at this result we have used $B_\mathrm{p} = |\nabla\Psi|/R$ and estimated that $|\nabla\Psi| \sim \Psi/r$. The above result allows us to draw an important conclusion: if the velocity of a particle is small, such that $\rho_\mathrm{p} \ll r$, then the second term in the toroidal canonical momentum is dominant. Therefore, a particle remains close to the same flux surface at all

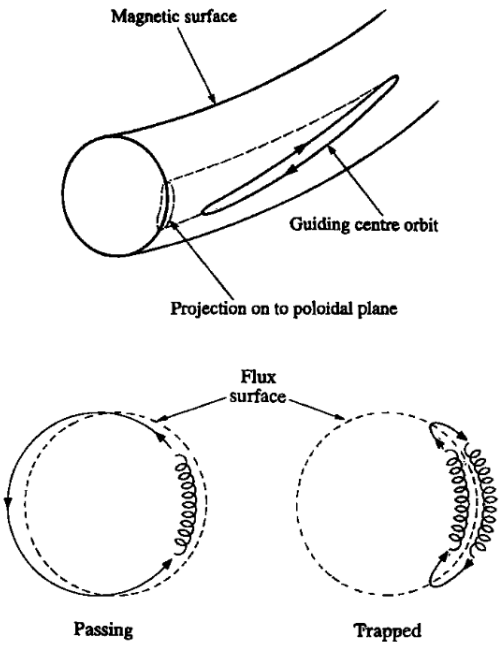

Figure 2.4: Illustration of the projection of a trapped particle orbit onto the poloidal plane (above) and of trapped and passing particle orbits in tokamak plasmas (below) [Wesson, 2004]. The variation of the magnetic field across the major radius of the plasma leads to magnetic forces which cause particles to drift from their initial flux surface and which causes some particles to become trapped on the outboard side of the tokamak. The origin of the major radius is to the left.

times. This condition is usually satisfied for thermal ions and electrons. For these particles, conservation of toroidal canonical momentum implies radial confinement. This is *Tamm's theorem* [Helander and Sigmar, 2002]. However, high energy ions can often have substantial poloidal gyroradii, particularly near the magnetic axis (where $B_\mathrm{p} \to 0$), as can high mass, low charge states impurities. Therefore, the orbits of these particles may deviate significantly from a given flux surface.

The radial extent of the trapped particle orbit may be determined using the constants of particle motion derived above. First, from the conservation of the toroidal angular momentum we may equate this quantity at two points of the particle orbit to find

$$mR_0 v_{\parallel,0} = mRv_\parallel - Ze(r - r_0)\Psi_0', \tag{2.80}$$

where the poloidal flux has been expanded as

$$\Psi(r) \approx \Psi(r_0) + \Psi'(r_0)(r - r_0). \tag{2.81}$$

Here the subscript zero indicates that the quantity has been evaluated in the outboard mid plane, at the position of minimum magnetic field on the particle orbit. Noting that $\Psi' \sim \nabla\Psi = RB_{\mathrm{P}}$ we have that

$$v_{\|} = \frac{R_0 v_{\|,0}}{R} + \Omega_p \Delta r, \tag{2.82}$$

with $\Delta r = r - r_0$ and Ω_P the poloidal cyclotron frequency. Eliminating $v_{\|}$ using the constancy of particle energy and noting that the conservation of magnetic moment yields the relationship

$$v_{\perp}^2 - v_{\perp,0}^2 = v_{\perp,0}^2 \epsilon \left(1 - \cos\theta\right). \tag{2.83}$$

For the large aspect ratio magnetic field (above) we find an equation that is quadratic in Δr, which we may solve to yield

$$\Delta r = \frac{2}{\Omega_P}\left[-\frac{v_{\|,0}R_0}{R} \pm \sqrt{v_{\|,0}^2 + v_{\perp,0}^2 \epsilon \left(1 - \cos\theta\right)}\right]. \tag{2.84}$$

In the outboard mid-plane we find that the distance between the two legs of the bounce orbit is

$$r_0 - r = \frac{2v_{\|,0}}{\Omega_p}, \tag{2.85}$$

assuming that $R_0/R \sim 1$.

2.4 Neoclassical transport theory: a heuristic discussion of collisional particle transport

Plasma transport theory is concerned with the determination of how, and at what rate, the transport of particles, energy and momentum perpendicular to a confining magnetic field occurs, in other words how quickly do particles escape the confining field. Understanding the mechanisms of plasma transport is of central importance to plasma physics. There are many examples of plasma behaviour and performance being limited by transport processes, from the transport of energy from the centre of the sun to the realisation of controlled nuclear fusion. Neoclassical theory provides a minimum level of transport which is inherent to *collisional* toroidal plasmas and an understanding of this level is critical in order to correctly analyse and diagnose transport contributions in magnetised plasmas.

Standard neoclassical theory [Hinton and Hazeltine, 1976; Hirshman and Sigmar, 1981] is a unified and mathematically complete theory of collisional transport in toroidal magnetised plasmas, the development of which followed the work of Galeev

and Sagdeev [1968], who first observed that transport in toroidal plasmas should be greater than expected from purely classical transport, that is, collisional transport in straight, uniform magnetic fields.

Whilst the majority of research effort spent investigating transport and confinement in tokamak plasmas has been directed towards the study of main ion and electron *turbulent* transport, a number of collisional mechanisms remain important for the next generation of tokamak devices and fusion reactors. For example, the bootstrap current [Bickerton et al., 1971; Zarnstorff et al., 1988] and radial electric field, investigated later in this thesis, are governed by neoclassical physics [Wang et al., 2006]. It is therefore important to have an accurate estimate of the level of neoclassical transport.

The full calculation necessary for computing particle transport rates, which relies on the averaged description of charged particle dynamics derived above, is a detailed and lengthy one and is beyond the scope of this thesis. The aim of this section is to simply introduce some standard concepts and results of neoclassical theory which are used throughout this thesis.

2.4.1 Classical transport

Individual particles in a plasma undergo collisions, which allow the particles to step perpendicular to the magnetic field with a step size equal to the Larmor radius, ρ, and with a characteristic collision time, τ. This leads to the classical diffusion coefficient [Helander and Sigmar, 2002]

$$D_{\mathrm{cl}} \sim \frac{\rho^2}{\tau} = \nu\rho^2. \tag{2.86}$$

The classical collision time for like ion collisions is given by [Helander and Sigmar, 2002]

$$\tau_{\mathrm{ii}} = \frac{6\sqrt{2}\pi^{3/2}\epsilon_0^2}{\ln\Lambda}\frac{m_{\mathrm{i}}^{1/2}T_{\mathrm{i}}^{3/2}}{n_{\mathrm{i}}Z_{\mathrm{i}}^4e^4}, \tag{2.87}$$

which is a function of the local ion temperature and density profiles, T_i and n_i, respectively. Here, $\ln\Lambda$ is the Coulomb logarithm and ϵ_0 is the permittivity of free space. For collisions of impurity ions with the main (or bulk) ion species, the collision time is a factor of $m_{\mathrm{Z}}/m_{\mathrm{i}}$ longer [Helander and Sigmar, 2002]

$$\tau_{\mathrm{zi}} \equiv \frac{1}{\nu_{\mathrm{zi}}} = \frac{6\sqrt{2}\pi^{3/2}\epsilon_0^2}{\ln\Lambda}\frac{m_{\mathrm{z}}T_{\mathrm{i}}^{3/2}}{n_{\mathrm{i}}m_{\mathrm{i}}^{1/2}Z_{\mathrm{i}}^2Z^2e^4}. \tag{2.88}$$

From this expression it is clear that highly charged impurity ions will tend to be more strongly collisional than bulk plasma ions due to the Z^2 in the denominator.

From the above expression for the impurity-bulk ion collision time, which varies as m_Z/Z^2, and the Larmor radius, which varies as $Z/m_Z^{1/2}$, we see that the rate of classical impurity diffusion is actually independent of particle mass and charge.

The total friction acting on impurity ions, $\mathbf{F}_Z$, is the sum of the friction due to bulk ions, $\mathbf{F}_{Zi}$, and due to electrons, $\mathbf{F}_{Ze}$,

$$\mathbf{F}_Z = \mathbf{F}_{Zi} + \mathbf{F}_{Ze}. \tag{2.89}$$

From the plasma fluid equations [Braginskii, 1965] the relative magnitude of these two contributions may be estimated as [Helander and Sigmar, 2002]

$$\frac{\mathbf{F}_{Ze}}{\mathbf{F}_{Zi}} \sim \frac{m_e n_e \nu_{Ze}}{m_Z n_Z \nu_{Zi}} \sim \sqrt{\frac{m_e}{m_i}} \sim \mathcal{O}\left(10^{-2}\right). \tag{2.90}$$

We therefore find that collisions between impurity and bulk plasma ions are more important than the collisions between impurities and electrons for determining the rate of impurity ion transport. We therefore neglect the later herein and assume that impurity transport is driven solely by collisions with the bulk ions.

Whilst the above condition generally holds for thermal impurities, the treatment of fast particle transport requires the inclusion of a velocity dependent contribution to the collision frequencies presented above [McClements and Hole, 2012]. With this inclusion it is found that electron-impurity collisions are more important than ion-impurity collisions for the fast impurity ions, although as the impurities collide with the electrons and slow-down impurity-ion collisions again dominate. Throughout the present text we assume thermal impurity ions.

2.4.2 Neoclassical transport and collisionality

One prominent result of the preceding discussion of particle orbits in non-uniform magnetic fields is that particles may drift from their initial flux surface. Particularly at high temperatures (for example, in tokamak fusion experiments) the classical diffusion argument is inapplicable since the lower collision frequency allows particles to follow trajectories determined by the global geometry. The existence of trapped particle orbits for example, whose orbits widths which may exceed the Larmor radius, implies that the step size of the diffusion is enhanced.

Neoclassical transport theory is an extension to classical theory which in-

cludes the effects of global magnetic field geometry on collision transport. Three regimes of neoclassical transport may be identified: a high collisionality regime, the *Pfirsch-Schlüter* regime; a low collisionality regime, the *banana* regime; and a regime connecting the two in which there is no dependence on the collision frequency, the so-called *plateau* regime. In each of these regimes the classical mass and charge dependencies persist.

The goal of transport theory is essentially to determine the rates of particle transport in each of these limiting collisionality regimes. Expressions for the diffusion coefficients in each of these regimes are presented below. The magnitude of the diffusion coefficient and the scaling of this coefficient with collisionality is illustrated in figure 2.5.

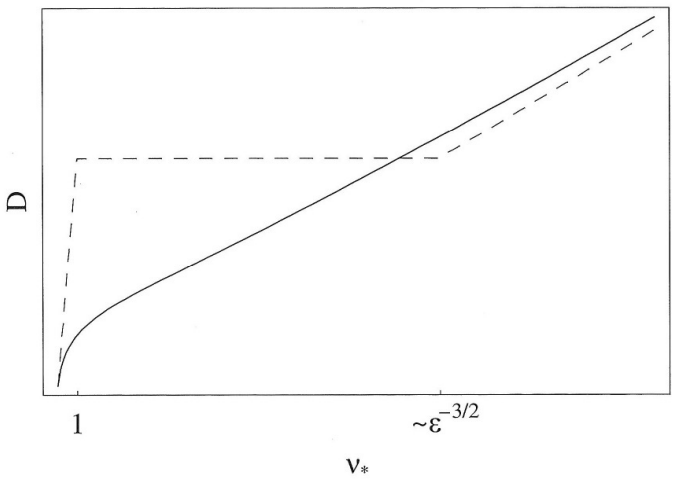

Figure 2.5: An illustration of the dependence of the neoclassical diffusion coefficient on collisionality. In the asymptotic limit $\epsilon \to 0$ (dashed line), with ϵ the inverse aspect ratio, three regimes of transport are evident, the so-called *banana*, *plateau*, and *Pfirsch-Schlüter* regimes. However, even at a relatively large aspect ratio of $\epsilon = 0.2$ (solid line) the plateau regime cannot be identified [Helander and Sigmar, 2002, pp. 150].

The Pfirsch-Schlüter regime

The dominant mechanism of cross surface transport depends on the relative magnitude of the collision frequency, ν, to the thermal transit frequency, $\omega_{\mathrm{T}} = v_{\mathrm{T}}/qR$. If this ratio is large,

$$\frac{\nu}{v_{\mathrm{T}}/qR} \gg 1, \tag{2.91}$$

collisions occur more frequently than the toroidal transiting of thermal particles and particle drift orbits are not completed. This high-collisionality limit is called the *Pfirsch-Schlüter* regime.

Typically the Pfirsch-Schlüter regime is associated with the relatively cool plasma edge, close to the separatrix. Here the plasma is sufficiently collisional to drive particle distributions to close to Maxwellian. Transport in this regime is driven by the variation within a flux surface of the collisional friction between particle species due to toroidal effects. This leads to an enhancement of the classical diffusion coefficient, which gives the Pfirsch-Schlüter diffusion coefficient [Wesson, 2004]

$$D_{\mathrm{PS}} \sim \left(1 + 2q^2\right) \frac{\rho^2}{\tau} = \left(1 + 2q^2\right) D_{\mathrm{cl}}. \tag{2.92}$$

Here q is the *tokamak safety factor*, which is the measure of the local field line pitch, or the rate of change of the toroidal magnetic flux with poloidal flux.

The banana-plateau regime

In the opposite limit,

$$\frac{\nu}{v_{\mathrm{T}}/qR} \ll 1, \tag{2.93}$$

collisions occur infrequently enough so that particles may complete their drift orbits. This limit is called the *banana-plateau* regime. The plateau regime refers to an intermediate regime (between the banana and Pfirsch-Schlüter regimes) in which circulating particles may complete their orbits but trapped particles may not, whereas in the banana regime both classes of particles may complete their full drift orbits before they are collisionally scattered. This subdivision of the banana-plateau regime is

$$\epsilon^{3/2} \ll \frac{\nu}{v_{\mathrm{T}}/qR} \ll 1 \qquad \text{Plateau regime,} \tag{2.94a}$$

$$\frac{\nu}{v_{\mathrm{T}}/qR} \ll \epsilon^{3/2} \qquad \text{Banana regime.} \tag{2.94b}$$

In the banana regime particles may be trapped on the outboard side of the tokamak and undergo trapped, or *banana*, orbits, see figure 2.4. The half-width of such particle orbits is given by [Wesson, 2004]

$$\Delta r = \frac{v_{\parallel}}{\Omega_{\mathrm{p}}} = \frac{q\rho}{\epsilon^{1/2}}, \tag{2.95}$$

which we take as the step size of the trapped particle diffusion. The frequency of the diffusive steps taken is also modified compared to the classical expression to reflect the fact that not all particles are trapped and to account for the trapping and de-trapping of particles by collisions. The effective collision frequency is given by $\nu_{\text{eff}} = \nu\epsilon^{-1}$ [Wesson, 2004]. We therefore take the banana regime diffusion coefficient to be

$$D_{\text{B}} \sim \frac{q^2}{\epsilon^{3/2}}\frac{\rho^2}{\tau} = \frac{q^2}{\epsilon^{3/2}} D_{\text{cl}}. \tag{2.96}$$

This is a factor $q^2/\epsilon^{3/2}$ larger than the classical diffusion given by (2.86) and approximately a factor $1/\epsilon^{3/2}$ larger than the Pfirsch-Schlüter diffusion coefficient. In spherical tokamak a greater proportion of particles are trapped compared to conventional tokamaks due to the larger magnetic field variation across the spherical tokamak device. Thus, spherical tokamaks are ideally suited to the study of neoclassical processes.

The plateau regime bridges the banana and Pfirsch-Schlüter regimes. Transport in this regime is dominated by slowly circulating particles. The plateau regime is an idealisation which relies on the large aspect ratio approximation. Detailed neoclassical transport calculations find that the plateau regime approximations are valid only for a very narrow range of collisionality for realistic values of the inverse aspect ratio (see figure 2.5 and Wesson [2004, sec. 4.7]). For spherical tokamak devices in particular this regime is relatively unimportant and is therefore not considered herein. Typically, modern formalisms of neoclassical transport group the banana and plateau regimes into a single regime.

2.4.3 Impurity ion diffusion in spherical tokamaks

Both the Pfirsch-Schlüter and banana regime diffusivities for impurity ions are actually independent of impurity mass, m_{Z}, and charge, Z. What does affect the rate of diffusion in a tokamak, as one varies Z and m_{Z} is the fractional volume of the plasma in which these two regimes apply: the collision rate varies as Z^2/m_{Z} while the bounce frequency varies as $1/m_{\text{Z}}^{1/2}$. Hence particles are pushed from the Pfirsch-Schlüter regime towards the banana regime if Z is reduced for fixed m_{Z} or if m_Z is increased at fixed Z. Banana regime particles are generally transported radially by collisions more rapidly than Pfirsch-Schlüter regime particles because they are undergoing a random walk with a larger step size, a trapped particle orbit width, which is of the order of the poloidal Larmor radius. This is of course significantly larger than the Larmor radius, which is the step size in the Pfirsch-Schlüter regime.

2.4.4 The test particle limit

In the following chapters we simulate the collisional transport of *test* impurity ions. In simulating test particles we assume that this species has no influence on the evolution and transport of the background main ion and electron species with which the impurities collide. In other words, there exists one or more background species which remain static or evolve independently of the test particle population.

In the previous section we also argued that the collisions between electrons and impurities have a negligible impact on the transport of impurity ions. We therefore assume, for the purpose of investigating the collisional transport of impurities, that there is a single background species, that is the bulk plasma ions or deuterons. In order simulate test impurity ions one must ensure that the density of the simulated impurity species does not exceed that allowed by the *test particle limit*

$$Z^2 n_z \ll n_i \left(\frac{m_e}{m_i}\right)^{1/2}, \tag{2.97}$$

where Z is the impurity ion charge number, n_z is the impurity ion number density, n_i is the bulk ion number density and m_e and m_i are the electron and bulk ion masses respectively. This condition essentially ensures that collisions of bulk ions with impurity ions are sufficiently infrequent that they have a negligible effect on the bulk plasma neoclassical transport and automatically ensures that collisions between impurity ions can be neglected [Helander and Sigmar, 2002].

2.5 Impurity transport in tokamak plasmas: the present work in context

2.5.1 Experimental observations of transport in conventional tokamaks

Neoclassical transport theory provides an irreducible minimum level of transport in toroidal confinement systems. In practice, however, the level of transport in tokamak plasmas greatly exceeds the neoclassical level. This so-called *anomalous* transport is likely to be turbulent transport driven by plasma micro-instabilities at the ion Larmor radius scale, such as the ion temperature gradient (ITG) mode, the trapped electron mode (TEM) and the electron temperature gradient (ETG) mode. The physical picture of these dominant particle transport mechanisms in the core of magnetically confined fusion plasmas is discussed by Angioni et al. [2009] and it is demonstrated that quantitative comparisons between theory and experiment

is possible. Essentially, it may be shown that particle flux is comprised of three terms: a diffusive term, driven by density gradients; a thermo-diffusive term, an off-diagonal term driven by temperature gradients and a purely convective (i.e. not proportional to the gradient of any kinetic profile) pinch term.

The goal of transport studies and fusion experiments is to control or to even fully suppress the level of anomalous transport. If this were achieved the underlying mechanism determining the rate of transport in tokamak plasmas would be collisional and the level of transport would be at its irreducible neoclassical level. This improved particle confinement would lead to higher core ion densities and longer particle and energy confinement times could be achieved, yielding increased fusion reaction rates and improved fusion reactor performance.

Indeed many experiments have demonstrated the routine transition of magnetically confined plasmas from a state of low confinement (L-mode) to a state of higher confinement (H-mode) [Wagner et al., 1982; ASDEX Team, 1989], in which the level of transport is significantly reduced, often to the neoclassical level. A physical picture of this suppression has been developed in recent years (see, for example, the introduction of Stutman et al. [2006] and references therein) with both magnetic shear and $\mathbf{E}\times\mathbf{B}$ flow shear able to regulate the level of anomalous transport. The realisation of H-mode will be crucial for achievement of the operation goals of future tokamak devices [Connor et al., 2004].

Generally the bulk ion rotation and pressure gradient in conventional tokamaks is not sufficient to result in complete $\mathbf{E}\times\mathbf{B}$ shear flow suppression of turbulence. However, in the vicinity of localised strong sheared rotation or large bulk ion pressure gradients there can be a region of enhanced $\mathbf{E}\times\mathbf{B}$ shear flow associated with significantly reduced levels of transport [Rogister, 1998]. These regions are referred to as *internal* or *external transport barriers*, ITBs and ETBs respectively, depending on their location in the plasma. In the vicinity of a transport barrier the level of transport can be close to the neoclassical level [Chen et al., 2001]. In addition, in regions of reversed magnetic shear ion thermal transport is reduced to the neoclassical limit [Levinton et al., 1995; Lazarus et al., 1996].

Of particular interest in the present work is the transport properties of impurity ions. It has been observed that the diffusivity of low charge state ($Z \leqslant 10$) impurity ions is closely related to the level of ion thermal transport [Synakowski et al., 1990; ITER Physics Expert Group on Confinement and Transport et al., 1999] which is generally anomalous in L-mode. For example, Synakowski et al. [1990] demonstrate that the diffusivity of He^{2+} is of the order of the ion momentum and thermal diffusivity in L-mode TFTR plasmas. Giannella et al. [1994] have also

shown that impurities including nickel and iron are transported anomalously, with diffusivities an order of magnitude greater than the neoclassical prediction, in JET L-mode plasmas.

On the other hand, numerous experiments have demonstrated neoclassical transport of impurity ions in H-mode experiments [Wenzel and Sigmar, 1990; Wade et al., 1998; Dux et al., 1999]. For example, in the vicinity of an internal transport barrier in JET H-mode plasmas, it was demonstrated that neoclassical transport was the mechanism for impurity (intrinsic carbon and injected nickel) transport, with quantitative agreement between experiment and theory [Chen et al., 2001].

Therefore, neoclassical mechanisms may dominate impurity ion transport, either in H-mode plasmas with low levels of turbulence or in the vicinity of locally suppressed turbulence or ITBs. However, recently is has also been noted that there is some evidence that anomalous transport is negligible for impurity transport, at least for light impurities, even in conventional tokamaks where ion transport is generally anomalous [Janzer et al., 2010].

A greater understanding of impurity transport (a topic which has received less attention than the transport of bulk ions) and the physical mechanisms at work is crucial in order to predict the overall performance of fusion plasmas [ITER Physics Basis Editors et al., 1999] and numerous open questions remain.

2.5.2 Experimental observations of transport in spherical tokamaks

One of the main predicted benefits of the ST design is a reduced level of turbulent ion transport compared with conventional tokamaks [Stutman et al., 2003]. Whilst the growth rates of the long wavelength micro-instability modes in STs is expected to be comparable with the case of conventional tokamaks, the $\mathbf{E}\times\mathbf{B}$ shearing rate required to suppress turbulence is lower in the lower magnetic field of the ST [Kotschenreuther et al., 2000]. This is supported by observed near neoclassical levels of bulk ion transport in MAST [Akers et al., 2003; Meyer et al., 2004] and NSTX [Stutman et al., 2003; Kaye et al., 2005]. Part of the reason for this relative ease of turbulence suppression in STs compared with conventional tokamaks is the higher levels of rotation achieved in ST plasmas due to their lower moment of inertia.

In addition to $\mathbf{E}\times\mathbf{B}$ shear flow and magnetic shear stabilisation of turbulence, gyrokinetic calculations which include beta gradient effects indicate that ITG and TEM modes should be intrinsically stable in the core of NSTX plasmas having a larger bulk ion temperature than electron temperature [Synakowski et al., 2002]. This effect is related to the gradient of the poloidal beta, which is generally higher in STs than conventional tokamaks. This implies the possibility of intrinsic stabili-

sation of turbulent modes in ST without the need for $\mathbf{E}\times\mathbf{B}$ shear flow stabilisation.

The baseline operating mode in MAST is a quasi-steady state H-mode, sustained through the control of an edge transport barrier (ETB) [Akers et al., 2003]. Transport analysis of such MAST H-mode plasmas indicates that bulk ion transport is close to the neoclassical level, within a factor of 1–3, demonstrating the importance of the collisional loss channel [Akers et al., 2003; Meyer et al., 2004; Kaye et al., 2005] in MAST H-mode plasmas. In L-mode plasmas, the ion transport significantly exceeds the neoclassical level, except in the vicinity of an ITB at mid minor radii [Field et al., 2011]. The combined effects of reduced levels of anomalous transport and enhanced neoclassical processes, due to the relatively large magnetic field variation across the plasma compared with conventional tokamaks, make MAST and other spherical tokamaks ideally suited for the study of neoclassical physics.

Chapter 3

Full orbit particle simulation

3.1 The test particle approach

The test particle approach is a widely used numerical method for analysing the dynamics and transport of particles. In this approach it is generally assumed that the particles being simulated have no effect on the background through which they move. Thus there exists a background field or species of particles which is static, or which evolves independently of, the test particle population.

This approach has been widely employed in fusion and plasma physics applications with many examples available in the literature. For example, the test particle approach has been used in the fusion physics context to determine collisional transport coefficients [Boozer and Kuo-Petravic, 1981; Maluckov et al., 2001; Kononenko and Shishkin, 2008; Kazakov and Kononenko, 2012], the formation and evolution of the radial electric field in tokamaks [Kiviniemi et al., 2000; Heikkinen et al., 2001], the heat loads on plasma facing components [Strumberger, 2000] and the effect of rotation [McKay et al., 2008; McClements and McKay, 2009] and toroidal field ripple [Bustos et al., 2010; McClements, 2005] on particle transport. Furthermore, when coupled with additional codes which solve, for example, for the plasma turbulence the effect of fluctuations of the background plasma may be studied [Romanelli et al., 2011].

One advantage of test particle modelling over analytical treatments is the simplicity of the test particle approach. The particle equations of motion (see section 2.3) can be solved numerically without any restriction on the particle and machine properties, whereas neoclassical theory, for example, typically assumes that the particle Larmor radius and the ratio of the poloidal to toroidal magnetic field components are small parameters. Furthermore, the test particle approach may be

applied to tokamak plasmas with arbitrary collisionality (or arbitrary density and temperature profiles), aspect ratio and magnetic field structure. The later point includes deviation of the magnetic field structure from axisymmetry and nested flux surfaces (due to magnetic islands [Hegna et al., 1993] or regions of stochastic magnetic fields [de Rover et al., 1999]) which are difficult to include in analytic models such as neoclassical theory.

Thus the test particle approach may be used as a rigorous benchmark of analytical theories and in order to test the validity of the approximations and assumptions employed. As noted by Nersisyan et al. [2007]:

> A fully numerical treatment is required for applications beyond the perturbative regime and for checking the validity of the perturbative approach.

One of the limitations of the test particle approach is the assumption that the simulated particles have no influence on the background species. Whilst this is generally the case for impurity ions, tokamak experiments often observe impurity concentrations which impact on the transport and confinement of the bulk ion species. In other words, the test particle limit of section 2.4.4 is not satisfied. In the MAST tokamak, for example, carbon and oxygen are the most abundant impurities, with concentrations of approximately $n_C/n_e \sim 5\%$ and $n_O/n_e \sim 1\%$ respectively [Romanelli et al., 2011]. Here n_C, n_O and n_e are the carbon, oxygen and electron densities respectively. Assuming fully ionised carbon and a bulk ion (and electron) density of 10^{19} m^{-3}, we find that $Z^2 n_Z/n_i \sim 2$ and (2.97) is not satisfied. Thus the test particle approach is strictly valid only for very low concentrations of impurity ions.

In the present chapter we discuss the development of a full orbit particle code which is capable of accurately simulating test particle dynamics in tokamak plasmas over transport time scales. We also discuss how this model may be extended to include the effects of collisions and the calculation of appropriate transport coefficients.

3.2 The CUEBIT full orbit code

The numerical tool used throughout the present thesis is the CUEBIT (CUlham Energy-conserving orBIT) code [McClements et al., 2002; Hamilton et al., 2003], which solves the Lorentz force equation in arbitrary magnetic and electric fields. This code utilises an implicit, second order, finite difference scheme where the derivatives of the particle position and velocity coordinates are discretised according to a

forward differencing scheme. Here the derivative of a function $f(x)$ at a point x is approximated by

$$\frac{\mathrm{d}f}{\mathrm{d}x} = \frac{f(x+h) - f(x)}{h} \tag{3.1}$$

when h is small. Here h is the spacing in the abscissa grid x.

In order to numerically solve for particle motion the Lorentz force equation this second order ordinary differential equation (ODE) is first rewritten as two first order ODEs:

$$\frac{\mathrm{d}\mathbf{v}}{\mathrm{d}t} = \frac{Ze}{m_{\mathrm{z}}} \left[\mathbf{E}(\mathbf{x}) + \mathbf{v} \times \mathbf{B}(\mathbf{x})\right], \tag{3.2a}$$

$$\frac{\mathrm{d}\mathbf{x}}{\mathrm{d}t} = \mathbf{v}. \tag{3.2b}$$

Applying the discretisation (3.1) to the above system of equations we have the integration scheme

$$\mathbf{v}^{i+1} = \mathbf{v}^{i} + \frac{Ze\Delta t}{m_{\mathrm{z}}} \left[\mathbf{E}\left(\frac{\mathbf{x}^{i+1} + \mathbf{x}^{i}}{2}\right) + \left(\frac{\mathbf{v}^{i+1} + \mathbf{v}^{i}}{2}\right) \times \mathbf{B}\left(\frac{\mathbf{x}^{i+1} + \mathbf{x}^{i}}{2}\right)\right], \tag{3.3a}$$

$$\mathbf{x}^{i+1} = \mathbf{x}^{i} + \Delta t \frac{\mathbf{v}^{i+1} + \mathbf{v}^{i}}{2}. \tag{3.3b}$$

to solve. Here the notation x^n denotes the value of the quantity x at a time $t = t_0 + (n-1) \cdot \Delta t$, with t_0 the starting time of the simulation and Δt the time step used to advance the simulation in time.

In the above integration scheme the electric and magnetic fields are evaluated at the averaged particle location $(\mathbf{x}^{i+1} + \mathbf{x}^{i})/2$. This scheme ensures that energy is conserved exactly in the absence of an electric field. This is clearly seen by taking the scalar product of (3.3a) with $\mathbf{v}^{i+1} + \mathbf{v}^{i}$.

It should be noted that the updated particle velocity, $\mathbf{v}^{i+1}$, appears both on the left- and right-hand side of (3.3). The above set of equations is therefore an *implicit* integration scheme and is solved using an iterative approach:

1. an initial guess for $\mathbf{v}^{i+1}$ is made by setting $\mathbf{x}^{i+1} = \mathbf{x}^{i}$ and solving (3.3a) for $\mathbf{v}^{i+1}$;

2. a more accurate estimate of $\mathbf{x}^{i+1}$ is then found by solving (3.3b), which is then used to obtain a more accurate value for $\mathbf{v}^{i+1}$;

3. this process continues until a suitable level of accuracy is reached. In practice, convergence is reached after approximately five iterations.

This numerical scheme is introduced and discussed in detail in McClements et al. [2002].

The time step in the CUEBIT code, Δt, must be chosen such that the shortest time scales in the simulation are well resolved. In the case of a full orbit code the highest frequency is the particle gyro motion. This is one of the major limitations of the full orbit approach [Lee, 1983] and a price to be paid for adopting such a simple approach [Kazakov and Kononenko, 2012], since the frequency of the phenomenon of interest may be several orders of magnitude lower than the cyclotron frequency. However, since we are not solving self-consistently for the fields we can simulate transport time scales (of the order of seconds) with the full orbit approach.

Using the implicit scheme described above a time step of one-tenth of the gyro-period is reasonable (even larger time steps may be used if the background profiles, for example the magnetic field and bulk ion density and temperature, vary on length scales much larger than the particle Larmor radius). It should be noted that the Larmor period varies across the tokamak. Therefore, the step size is specified relative to some reference location, generally taken to be the magnetic axis. By comparison with guiding centre codes, which solve the set of equations 2.63 and 2.64 and typically use a time step of approximately $1/25^{\text{th}}$ of the particle bounce time, full orbit codes require over 50 times more computation time.

The CUEBIT algorithm described above and used throughout this thesis has excellent stability and energy conservation properties, as presently demonstrated. However, since this algorithm is implicit it is not the most efficient scheme available, since at each time step the equations of motion are solved multiple times for each iteration of the solution. A number of alternative explicit integration methods could be used instead, including the Boris rotation [Boris, 1970; Birdsall and Langdon, 1985] and standard explicit Runge-Kutta schemes. However, it has been found while evaluating these alternative schemes that the Boris rotation method does not conserve particle gyro-frequency: the gyration frequency is underestimated by a factor $1 - (\Omega\Delta t)^2/12$, with Ω the particle cyclotron frequency. We may correct for this by replacing the electric and magnetic fields by effective fields where we divide through by this factor. Then, automatically, the gyration frequency is more correctly tracked. Furthermore, energy conservation in the Runge-Kutta scheme is not explicit and numerical errors in the orbit integration will be visible as non-physical drifts of energy. This scheme therefore typically requires orbit corrections at each time step in order to achieve acceptable constancy of the appropriate conserved quantities. For example the ASCOT code [Kiviniemi et al., 2000; Heikkinen et al., 2001] adjusts the particle location computed by the solution of the guiding centre equations of motion

in order to match the energy, magnetic moment and toroidal canonical momentum of the particle at the previous time step to within some prescribed accuracy.

Ideally one would use an explicit *variation symplectic* integration scheme, similar to that used to solve for the guiding centre motion of particles by Qin et al. [2009], since such schemes are constructed in such a way to ensure that the discrete analogous of the conserved quantities derived in section 2.3 are conserved exactly (to machine precision). Qin et al. [2009] demonstrate the advantages of such schemes over non-variational Runge-Kutta methods. The construction of a variational symplectic integration scheme for the full orbit equations of motion in toroidal plasmas is an open area for future work.

3.3 Collisionless particle orbits

The numerical scheme described in brief above is tested by solving for a number of particle orbits in a spherical tokamak equilibrium, see figure 3.1. Here the three main classes of particle orbit in an axisymmetric toroidal magnetic field, *trapped*, *passing* and *potato*, are simulated and projected onto the poloidal tokamak cross section. Figure 3.1 demonstrates an interesting feature of trapped orbits that is unique to spherical tokamaks: that is the widest part of a trapped particle orbit is not necessarily in the outboard mid plane of the device. Here the widest part of the particle orbit is at the vertical extremes of the orbit due to the shaping (vertical elongation) of the plasma.

The plasma equilibrium used in these simulations is the Solov'ev equilibrium derived in section 2.2.3 with $R_0 = 3$ m, $\epsilon = 0.1$, $B_{\mathrm{T},0} = 3$ T, $I_{\mathrm{P}} = 1.5 \times 10^5$ A, and $\kappa = 1$. The magnetic field components required in (3.3a) are computed from the Solov'ev poloidal flux function (2.34). From the general form of the magnetic field vector, (2.8), we have that the magnetic field components in cylindrical components are

$$B_R = -\frac{1}{R}\frac{\partial \Psi}{\partial Z} = \frac{8\Psi_0}{\alpha^2\kappa^2 R_0^4} RZ, \tag{3.4a}$$

$$B_\phi = \frac{f(\Psi)}{R} = \frac{R_0 B_{\mathrm{T},0}}{R}, \tag{3.4b}$$

$$B_Z = \frac{1}{R}\frac{\partial \Psi}{\partial R} = -\frac{4\Psi_0}{\alpha^2 R_0^4}\left(R^2 - R_0^2 + \frac{2Z^2}{\kappa^2}\right). \tag{3.4c}$$

Whilst this equilibrium model is two dimensional CUEBIT solves for the particle dynamics in three dimensions. In three dimensions trapped particle orbits *precess* in toroidal angle, that it the toroidal angle of the particle bounce points drifts over

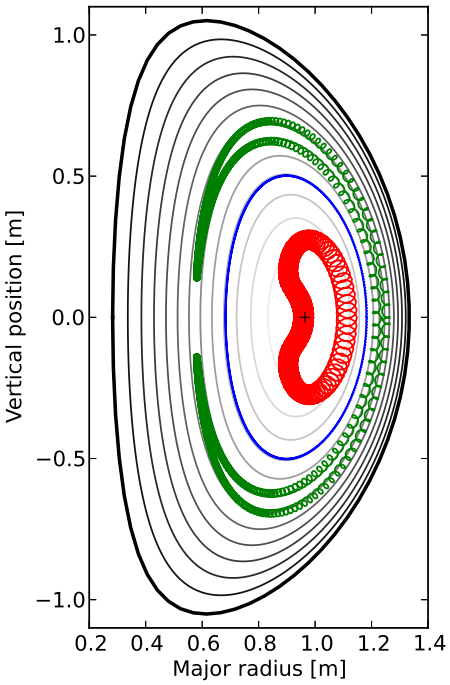

Figure 3.1: Poloidal projections of C^{6+} orbits in a MAST-like Solov'ev equilibrium, as computed by CUEBIT, illustrating the three main classes of particle orbit: a passing particle orbit (blue), a trapped orbit (green) and a potato orbit (red).

adjacent particle bounce orbits [Roach et al., 1995]. The frequency of this *toroidal precession* provides, at large aspect ratio, an additional check on the accuracy of the particle solver.

An important test of a particle following code is the demonstration of the constancy of the conserved quantities derived in section 2.3.2. For the trapped particle orbit presented in figure 3.1 the relative change in particle energy at each time step of the simulation,

$$\Delta E(t_i) = \frac{|E(t_i) - E(t_0)|}{E(t_0)}, \tag{3.5}$$

is presented in figure 3.2. CUEBIT conserves energy to machine accuracy, that is the difference in energy between successive time steps is equal to the difference between floating point numbers of the machine. However, what is important for an accurate code is that these small errors between time steps do not build up over the simulation. Figure 3.2 shows that there is little secular increase in particle energy with time and the maximum relative change is less than approximately 3×10^{-14}.

However, it is not sufficient for the algorithm to conserve just energy. The particle magnetic moment and, for the case of an axisymmetric magnetic field, toroidal canonical momentum are both constants of the particle motion and thus

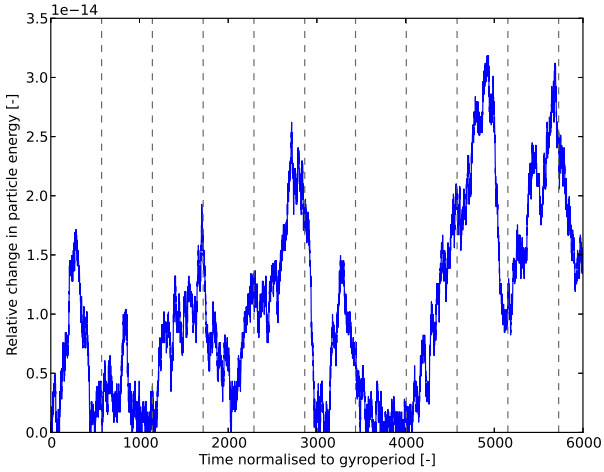

Figure 3.2: Change in particle energy relative to the initial particle energy for the trapped particle orbit presented in figure 3.1. Vertical dashed lines denote bounce periods.

must also be conserved. Generally, it is found that these quantities are not as well conserved as particle energy. However, an acceptable level of accuracy, approximately single precision accuracy, of the toroidal canonical momentum is obtained when the time taken is taken to be equal to or less than one tenth of the Larmor period of the particle, as demonstrated in figure 3.3.

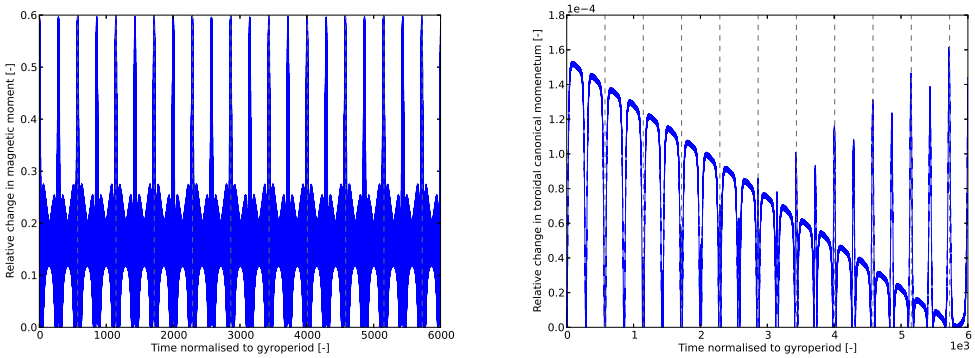

Figure 3.3: Change in particle magnetic moment (left) and toroidal canonical momentum (right) relative to the respective initial values for the trapped particle orbit presented in figure 3.1. Vertical dashed lines denote bounce periods.

From figure 3.3 it is clear that magnetic moment is not particularly well conserved. This reflects that the magnetic moment is an *adiabatic invariant*, rather than an exact constant of the particle motion. The magnetic moment calculated in

section 2.3.2, $\mu = mv_{\perp}/2B$, is simply the first term in an expansion of this quantity. Thus the conservation of this quantity is not a particularly good assumption at tight aspect ratio and one must include higher order terms in the definition of the magnetic moment. One striking consequence of this *non-adiabatic*, or non-constant μ, behaviour at tight aspect ratio is the transition of beam injected particle orbits from trapped to unconfined orbits, even in the absence of collisions, as demonstrated by Akers et al. [2002, Fig. 3]. It has been observed that particle magnetic moment is better conserved in simulations of large aspect ratio tokamaks, where the orderings used to derive this adiabatic invariant are more clearly satisfied.

Figure 3.4 demonstrates that the CUEBIT algorithm is second order accurate in time, that is the accuracy of the solution computed scales with the time step used in the simulation to the second power. It should be noted that since the algorithm is constructed such that energy is conserved exactly (to machine accuracy) it is not possible to deduce the order of the scaling from the scaling in the relative error in the particle energy (energy is conserved exactly regardless of the simulation time step chosen). Thus one can also not use the error in the particle gyroradius. The relative maximum change in toroidal canonical momentum is therefore used in figure 3.4 to determine the order of the CUEBIT algorithm.

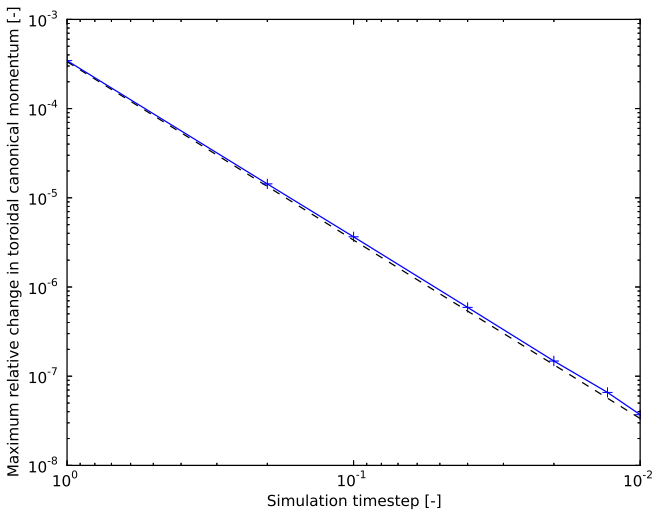

Figure 3.4: Scaling of the maximum relative change in toroidal canonical momentum with simulation time step (solid line). Each simulation is run for 1000 cyclotron periods. The dashed line indicates the scaling expected scaling for second order accuracy.

As a demonstration of the stability of the CUEBIT integration scheme a

trapped particle orbit is simulated for 10^5 gyro periods (approximately 2000 bounce periods or 20 ms) in figure 3.5. It is seen that the relative change in particle energy remains below 10^{-13} for the entire simulation and there is no drift in the particle orbit in configuration space. Thus we may confidently simulate impurity ion dynamics for transport time scales.

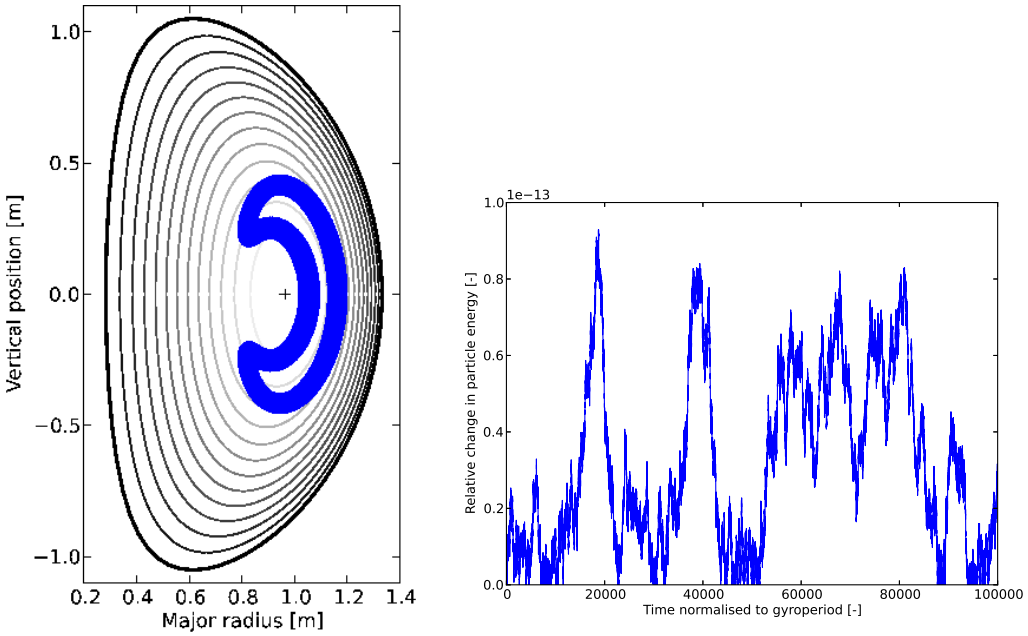

Figure 3.5: Trapped particle orbit (left) simulated for 10^5 cyclotron periods and the corresponding relative change in particle energy (right). It is clear there is no secular increase in particle energy or any drift of the particle orbit.

3.4 Particle orbits in numerical equilibria

During the course of the present work CUEBIT was extended in numerous ways. One of these enhancements is the option to use numerically defined equilibria, from the output of an equilibrium code for example, to prescribe the plasma equilibrium as an alternative to the analytical Solov'ev model. Equilibrium codes such as CHEASE [Lütjens et al., 1992, 1996] generally have an option for outputting the poloidal flux, as computed from the numerical solution of the Grad-Shafranov equation, on a rectilinear grid in the poloidal plane, that is $\Psi(R_i, Z_j)$, where R_i and Z_j are the discrete values of the major radius and vertical position of each of the grid nodes. Using an equilibrium reconstruction code such as EFIT [Lao et al., 1985], which attempts to determine the plasma equilibrium from data acquired from a

suite of tokamak diagnostics, in conjunction with an equilibrium code allows one to match experimental equilibria in CUEBIT simulations. In order to utilise a numerical poloidal flux function, rather than the analytic Solov'ev solution, it is required that methods for interpolating gridded poloidal flux values to arbitrary particle locations using bicubic splines be added to CUEBIT. An example of a trapped particle trajectory computed in a numerically prescribed plasma equilibrium, reconstructed from MAST shot number 26587, is presented in figure 3.6.

It is found that good energy conservation and orbit stability are maintained when using a numerically prescribed equilibrium despite the relatively few grid points used (65×65) in computing the trajectory in figure 3.6. However, the use of numerically prescribed equilibria comes at the expense of a longer simulation running time, since at each time step and for each particle the poloidal flux and magnetic field components must be interpolated from their gridded values, a more costly operation than evaluation of the analytic Solov'ev expressions of section 2.2.3.

On the other hand, use of arbitrary numerical equilibrium lifts some of the limitations of using an analytic Solov'ev equilibrium model (see section 2.2.3). For example, one may simulate plasmas with arbitrary shaping without restriction on the plasma geometry. In particular up-down asymmetric diverted plasmas, which are difficult to model with the Solov'ev solution, can easily be simulated: the experimental shape and conditions of MAST equilibria can therefore be used directly. Furthermore, particle trajectories outside of the plasma separatrix and in the vicinity of X-points (locations of zero poloidal magnetic field) and magnetic field coils may be simulated (these regions are not modelled with the Solov'ev solution). Finally, the effects of plasma rotation on the equilibrium are easily incorporated. The use of numerically defined plasma equilibrium therefore improves the flexibility of CUEBIT since the code is no longer tied to a particular analytical equilibrium model.

3.5 Collisional particle dynamics: the Lorentz-Langevin equation

The Langevin approach is widely used in order to determine the effect of fluctuations in macroscopically known systems [Langevin, 1908; Van Kampen, 1992; Coffey et al., 2004]. These fluctuations, which represent the collisional scattering and slowing-down of particles, are modelled by adding random, or *stochastic*, terms to the equations of motion. Mathematically, this approach is equivalent to the solution of a Fokker-Planck equation but has the advantage of greater simplicity.

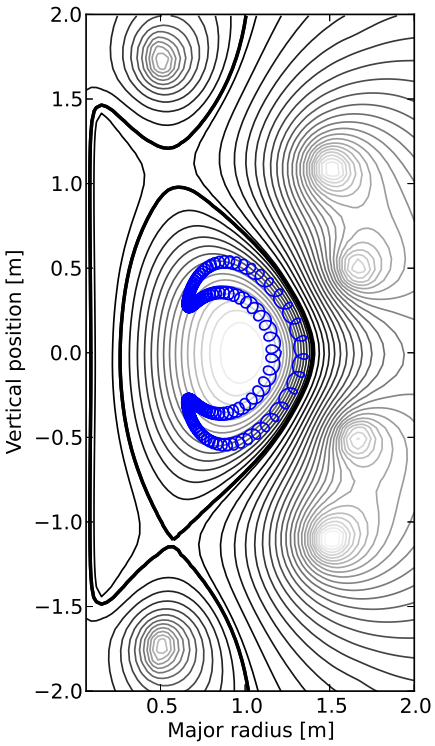

Figure 3.6: Trapped orbit of a 1.7 keV C^{6+} ion in a numerical equilibrium. The equilibrium is reconstructed from MAST shot number 26587 using the equilibrium reconstruction code EFIT and processed by the CHEASE equilibrium code before use as input to CUEBIT.

A Brownian particle of unit mass obeys the equation of motion

$$\dot{v} = -\gamma v + L\left(t\right) \tag{3.6}$$

where the stochastic variable to be considered is the velocity of the particle, v, rather than it's position. The right-hand side of this equation is the force exerted by the particles of the surrounding medium. Whilst this force is unknown we may postulate a number of the physical properties of this force:

1. The force consists of a damping term, linear in v with a constant coefficient γ, plus a remainder $L(t)$. $L(t)$ may be treated as a stochastic process.

2. The stochastic properties of $L(t)$ are prescribed regardless of v, so that $L(t)$ is an external force. The average of this term vanishes

$$\langle L\left(t\right)\rangle = 0. \tag{3.7}$$

3. $L(t)$ is caused by collisions with the particles of the surrounding fluid and varies rapidly. This may be formalised by postulating for its auto correlation

function

$$\left\langle L\left(t\right)L\left(t'\right)\right\rangle = \Gamma\delta\left(t-t'\right), \tag{3.8}$$

with Γ a constant. The idea here is that each collision is practically instantaneous and that successive collisions are uncorrelated. In fact, the delta function should be replaced by a function of $|t-t'|$ that is a sharp peak with a width that is equal to the duration of a single collision. Provided that this is shorter than all other relevant times one may use a delta function for convenience.

A term having the above three properties is called a Langevin force and (3.6) is the Langevin equation. In this name we include the three properties given above.

3.5.1 Solution of the Langevin equation

We now proceed to solve the Langevin equation. Since this equation is a stochastic differential equation, or a differential equation whose coefficients are random functions of time with some given properties, this defines $v(t)$ as a stochastic process. Specifying an initial condition $v(0) = v_0$ we may solve (3.6) explicitly as

$$v\left(t\right) = v_0 e^{-\gamma t} + e^{-\gamma t}\int_0^t e^{\gamma t'}L\left(t'\right)dt'. \tag{3.9}$$

In order to extract useful information from this solution we must average over all possible realizations of $L(t)$. The average of this result for a sub-ensemble of Brownian particles, all with initial velocity v_0, is simply $\langle v(t)\rangle_{v_0} = v_0 e^{-\gamma t}$.

We now derive a relationship between the coefficients of the Langevin equation, γ and L (or equivalently Γ, see point three above). First we square (3.9) and average over a sub-ensemble of particles all with initial velocity v_0:

$$\left\langle v^2\left(t\right)\right\rangle_{v_0} = v_0^2 e^{-2\gamma t} + e^{-2\gamma t}\int_0^t dt'\int_0^t dt'' e^{\gamma(t'+t'')}\left\langle L\left(t'\right)L\left(t''\right)\right\rangle. \tag{3.10}$$

Note that the cross terms vanish because of postulate 2. Using (3.8) we find that

$$\left\langle v^2\left(t\right)\right\rangle_{v_0} = v_0^2 e^{-2\gamma t} + \Gamma e^{-2\gamma t}\int_0^t dt'\int_0^t dt'' e^{\gamma(t'+t'')}\delta\left(t'-t''\right) \tag{3.11a}$$

$$= v_0^2 e^{-2\gamma t} + \Gamma e^{-2\gamma t}\int_0^t dt'' e^{2\gamma t''} \tag{3.11b}$$

$$= v_0^2 e^{-2\gamma t} + \frac{\Gamma}{2\gamma}\left(1-e^{-2\gamma t}\right). \tag{3.11c}$$

We now identify the previously unspecified function Γ by noting that for long times,

$t \to \infty$, the mean square velocity must have the known thermal value

$$\lim_{t\to\infty} \left\langle v^2 \right\rangle = \frac{\Gamma}{2\gamma} = k_{\mathrm{B}} T. \tag{3.12}$$

We have now related the size of the fluctuating term Γ to the damping term γ. This is the simplest form of the general fluctuation-dissipation theorem. The success of the Langevin approach is due to this: the noise term in the Langevin equation is fully expressed by the macroscopic damping constant, together with the temperature.

The physical picture of the Langevin approach is that random kicks tend to spread out the velocity v, while the damping terms tend to bring v back to zero. The balance between these two opposing tendencies is the equilibrium distribution.

Equation (3.12) tells use that wherever there is a damping there must be fluctuations. These fluctuations are small on the macroscopic scale because of the factor $k_{\mathrm{B}}T$. In practice they only appear when magnified in some way. For example, the velocity fluctuations in (3.11c) are not seen, but they build up a mean square displacement which may be observed. This will be used to determine the transport properties of impurities in tokamak plasmas in later chapters.

The Fokker-Planck (FP) equation describes the time evolution of the probability density function of the velocity of a particle. One would expect that (3.6) is equivalent to the FP equation [Van Kampen, 1992]. However, this is not strictly the case, since the FP equation fully specifies the stochastic process $v(t)$, whereas the Langevin equation determines only the first two moments of this process (since the higher order moments were not discussed in postulates 1-3). One therefore usually supplements these postulates with the additional condition:

4. L(t) is a Gaussian, in other words all odd moments vanish.

Formally the Langevin equation, with this supplementary postulate, describes the characteristics of the Fokker-Planck equation, and many realisations of the Langevin equation gives a distribution of particle velocities which is a solution to the Fokker-Planck equation (see figure 3.7).

3.6 Applying the Langevin approach to collisional particle transport studies

To describe a system with fluctuations using the Langevin approach we apply this approach as follows:

1. write the deterministic macroscopic equations of motion of the system,

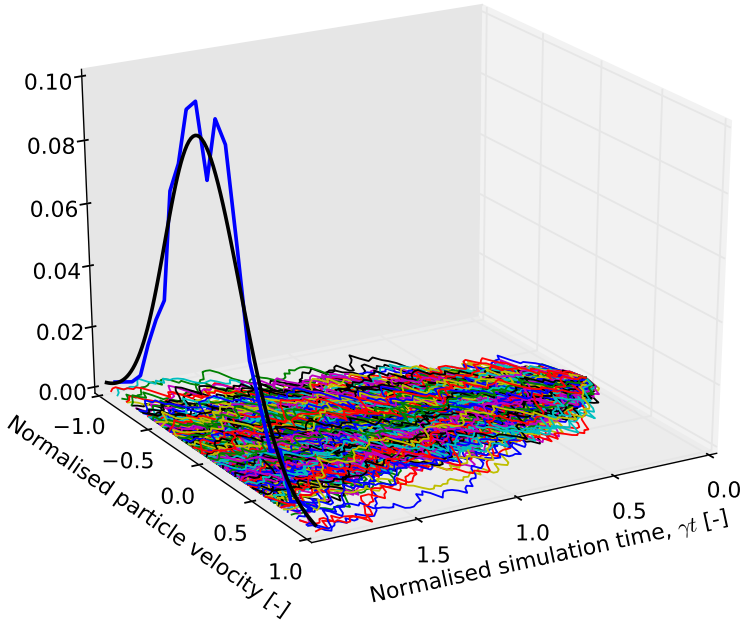

Figure 3.7: Multiple realisations of the Langevin equation (3.6) with $\gamma = k_{\mathrm{B}}T = 1$. Each curve in the velocity-time plane represents the time evolution of particle velocity determined from an independent solution of the Langevin equation. The thick blue curve is the distribution of all particle velocities at the end of the simulation and the thick black curve is the expected velocity profile. The deviation of the simulated solution from the expected solution is due to the finite number of realisations.

2. add a Langevin force with the properties described above,

3. adjust the fluctuating term Γ such that the stationary solution reproduces the correct mean square fluctuations known from statistical mechanics.

The coefficient of the damping in (3.6) for the case of test impurity ions colliding with a bulk ion species is the impurity-ion collision frequency given by (2.88). These collisions cause a particle to thermalise to the temperature of the background species with which it is colliding. Thus (3.12) gives an expression for the autocorrelation function of the fluctuating term in (3.6) of

$$\Gamma = \frac{2k_{\mathrm{B}}T_i}{\tau_{\mathrm{zi}}}, \tag{3.13}$$

with T_i the bulk ion temperature.

With these results and following the procedure above we arrive at the *Lorentz-Langevin* equation,

$$m_{\mathrm{z}}\frac{\mathrm{d}\mathbf{v}}{\mathrm{d}t} = m_{\mathrm{z}}\left(\mathbf{E}+\mathbf{v}\times\mathbf{B}\right) - \frac{m_{\mathrm{z}}}{\tau_{\mathrm{zi}}}\left(\mathbf{v}-\mathbf{u}\right) + m_{\mathrm{z}}\mathbf{a}_r, \tag{3.14}$$

which describes the dynamics of test particle ions colliding with a prescribed fluid background which is moving with velocity $\mathbf{u}$. This is the equation which is solved in order to investigate the collisional dynamics of test particles in tokamak plasmas throughout the remainder of the present thesis.

In the above equation $\mathbf{a}_r$ represents the random velocity kicks due to collisions with the background bulk ion plasma and is assumed to follow a Gaussian distribution (see postulate 4 above). Thus this term is a set of three random numbers chosen independently for each particle and at each time step from a Gaussian distribution with zero mean and variance

$$\sigma^2 = \frac{\Gamma}{\Delta t} = \frac{2k_{\mathrm{B}}T_i}{\tau_{\mathrm{zi}}\Delta t}. \tag{3.15}$$

Here the delta function of (3.8) has been replaced with the finite simulation time step, Δt, used in CUEBIT. Although the instantaneous collisions are taken to be isotropic, the cumulative effect of these over an impurity Larmor orbit naturally reflects the effects of gradients in the bulk ion temperature and density profiles (leading to, for example, thermal forces), which in turn leads to anisotropy in the collisions. This is not the case in guiding center codes, which generally add these effects *a posteriori*.

The combined effects of the addition of the Langevin terms to the Lorentz equation is to, in the absence of an electric field, ensure that the impurities relax to a drifting Maxwellian distribution with a temperature T_i and flow velocity $\mathbf{u}$ which matches that of the bulk ions and to cause a scattering of particle velocity vectors. The relaxation of the temperature of the impurity species distribution, T_Z, to the temperature of the main ion species, T_i, is demonstrated in figure 3.8. Here the impurity distribution of 5×10^4 C^{6+} ions is initialised with a temperature of 330 eV and equilibrates to the bulk ion temperature of 250 eV with a characteristic time scale equal to the prescribed impurity-ion collision time.

The scattering of particle velocity vectors due to the Langevin terms leads to a diffusion of the impurity particle ensemble in space. This is demonstrated in figure 3.9, in which 10^4 C^{6+} ions are initially uniformly distributed on the flux surface labelled by a normalised poloidal flux of 0.5 and with a Maxwellian velocity distribution. The collisional terms in the Lorentz-Langevin equation cause the en-

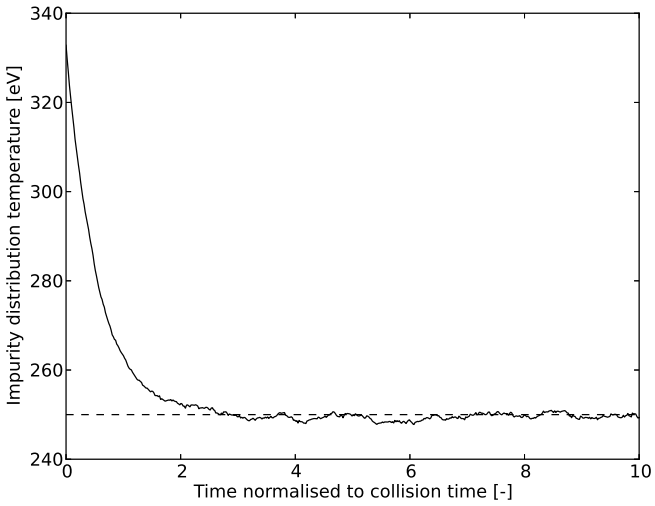

Figure 3.8: Equilibration of the impurity species temperature (solid line) with the background ion temperature (dashed line) in a uniform magnetic field and with a prescribed collision time of 0.08 ms. The simulation time is normalised to the impurity-ion collision time (2.88).

semble of particles to diffuse in space and after approximately 500 collision times the particles have largely filled the tokamak volume.

In the simulations of figure 3.9 and for the remainder of the present work, the bulk ion density and temperature profiles are prescribed to have the forms

$$n_i(s) = (n_{\text{core}} - n_{\text{edge}})\,(1-s)^{\alpha} + n_{\text{edge}}, \tag{3.16a}$$

$$T_i(s) = (T_{\text{core}} - T_{\text{edge}})\,(1-s)^{\beta} + T_{\text{edge}}, \tag{3.16b}$$

with n_{core}, n_{edge} and α, and the equivalent parameters for the temperature profile, free parameters and $\psi = 1 - \Psi/\Psi_{\text{axis}}$ is the normalised poloidal flux. Here the parameters α and β control the gradient of the profiles, with $\alpha = \beta = 0$ corresponding to flat (constant) bulk ion profiles and $\alpha = \beta = 1$ corresponds to a linear variation of the bulk ion profiles with normalised minor radius. This later case is the standard set of values of α and β used throughout the remainder of this thesis. The bulk ion density and temperature profiles above couple the bulk ion and impurity species through the collision time, τ_{zi} [given by (2.88)], present in the test impurity equation of motion, (3.14).

Figure 3.9 demonstrates another enhancement of the CUEBIT code implemented during the course of the present work, that is the loading of test particles

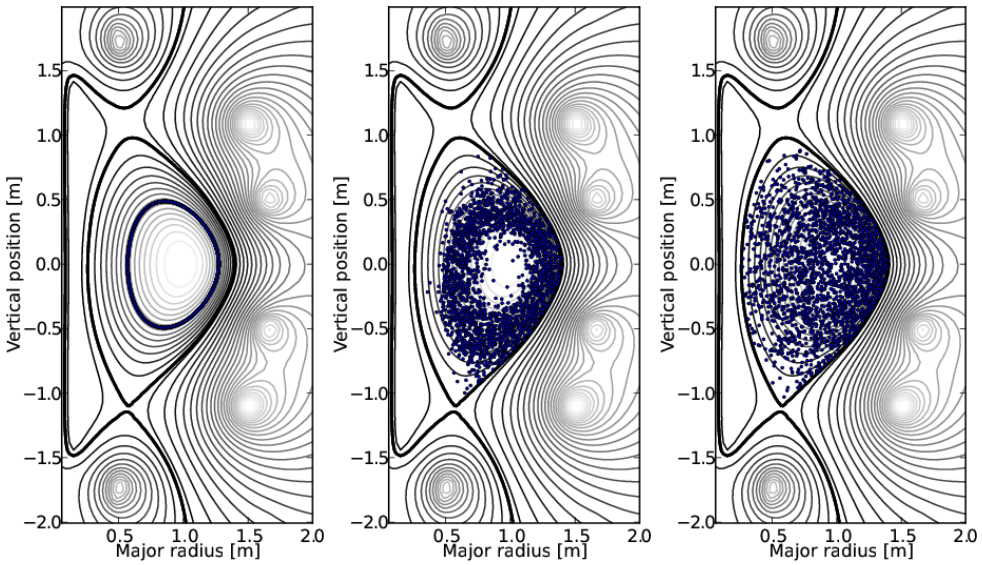

Figure 3.9: Diffusion of 2×10^3 C^{6+} ions in configuration space. Initially all ions are distributed uniformly on a flux surface labelled by a normalised poloidal flux of 0.5 (left). Collisions cause particles to diffuse radially (centre) and after 10 ms, or approximately 500 collision times, the ions have filled the tokamak volume (right).

in phase-space. Early versions of CUEBIT initialised all particles at the magnetic axis. Each simulation therefore began with a transient phase which allowed particles to diffuse to fill the tokamak volume. This is clearly a waste of computation time, particularly for the simulations presented in the later parts of the current thesis, which concern the effects of a radial electric field located near the plasma edge on impurity particle transport. To reduce this computation time we therefore implemented a Hammersley (uniform, low discrepancy [Hammersley, 1960; Halton, 1960]) loading of particles in toroidal coordinates $\{\Psi, \theta, \phi\}$). This allows the user to specify a range of normalised poloidal flux values, between which impurity ions are uniformly loaded. However, the equations of motion, (3.2), are solved in Cartesian coordinates, which requires the derivation and implementation of the inverse coordinate transformation $(\Psi, \theta, \phi) \rightarrow (R, \phi, Z) \rightarrow (x, y, z)$ for the case of the Solov'ev equilibrium model. In the case of numerically prescribed equilibrium bisection is used to perform this transformation.

In addition, the treatment of boundary conditions employed in CUEBIT has been improved. With the addition of the treatment of collisions to the CUEBIT numerical scheme particles may undergo a random walk out of the plasma. Previously particles were simply removed from the simulation if they crossed the last closed flux surface. This leads to a gradual depletion in the number of particles simulated

and therefore a reduction in the quality of the statistical information which may be determined from the evolution of the ensemble of particles.

In the present version of CUEBIT the user is free to specify an inner and an outer boundary by specifying the minimum and maximum normalised poloidal flux of interest (with the range $[0, 1]$ describing the entire tokamak volume). When the radial location of a particle's guiding centre is outside of this range the sign of the poloidal angle of the particle is changed, $\theta \rightarrow -\theta$, and the radial location of the guiding centre is constrained to be in the allowed range. The allows just an annulus of the tokamak to be simulated, increasing the density of simulated particles in the region of interest and reducing the required computation time. One of the major advantages of this treatment of particle boundaries is that the number of simulated particles is constant and, in principle, steady state distributions of impurity ions may be determined.

3.6.1 The parallel friction force

In addition to the usual Langevin terms, there is an additional term which has been added to (3.14), that is $-m_z\mathbf{u}/\tau_{zi}$. The term $-m_z\nu_{zi}\left(\mathbf{v}-\mathbf{u}\right)$ is often referred to as an *Einstein drag* term, or simply a drag term. The effect of such a term is to cause particles to tend to the velocity $\mathbf{u}$ with a typical time scale of τ_{zi}. This is easily seen by solving the equation

$$\frac{\mathrm{d}\mathbf{v}}{\mathrm{d}t} = -\nu_{zi}\left(\mathbf{v}-\mathbf{u}\right) \tag{3.17}$$

with $\mathbf{u}$ assumed to be constant. This equation has the solution (this type of equation is solved in more detail in section 5.4.2)

$$\mathbf{v} = \mathbf{u} + \mathbf{v}_0 e^{-\nu_{zi}t}. \tag{3.18}$$

with $\mathbf{v}_0$ determined by the imposing of initial conditions. Thus for $t \rightarrow \infty$ we find that $\mathbf{v} \rightarrow \mathbf{u}$.

Previous work has used this term to investigate the role of bulk plasma rotation on impurity transport in spherical tokamaks [McKay et al., 2008; McClements and McKay, 2009]. Here $\mathbf{u}$ was prescribed to match typical rotation values of the bulk ions in MAST plasmas.

However, in the present work this term is used to investigate the correspondence between conventional neoclassical theory and the numerical treatment described above in order to ensure that the CUEBIT code is reproducing the collisional transport of impurity ions in tokamak plasmas correctly. Specifically, this term is used to model the *parallel friction force* exerted on impurity ions due to a

non-Maxwellian distribution of bulk ions [Helander and Sigmar, 2002]. This force arises when the bulk ion species is in the banana regime, since the collisionality is sufficiently low that particles may complete drift orbits determined by the global geometry of the magnetic field which causes the distribution of particles to vary across a flux surface. This deviation from Maxwellian leads to an additional friction between the bulk and impurity ion species which acts parallel to the magnetic field [Helander and Sigmar, 2002]. This parallel friction force is simulated in CUEBIT by prescribing

$$\mathbf{u} = -\frac{RB_\phi}{Zen_iB}\frac{\mathrm{d}p_i}{\mathrm{d}\Psi}\mathbf{b}. \tag{3.19}$$

Here R is the major radial coordinate, n_i is the bulk ion density, $\mathrm{d}p_i/\mathrm{d}\Psi$ is the bulk ion pressure gradient, B and B_ϕ are the total and toroidal magnetic field strengths respectively and $\mathbf{b} = \mathbf{B}/B$ is the unit vector parallel to the magnetic field. This term is investigated in the next chapter.

In this chapter we have demonstrated the construction and verification of a test particle, full orbit code which is suitable to use for the investigation of the collisional dynamics of test impurity ions in global spherical tokamak plasmas. In the remaining chapters we benchmark CUEBIT against neoclassical theory and use the code to investigate the effect of a particular feature of high performance tokamak experiments on impurity transport, that is a sheared radial electric field.

Chapter 4

Comparison of full orbit and neoclassical codes

The standard theory of collisional transport in toroidal plasmas, neoclassical theory [Hirshman and Sigmar, 1981], has been extensively studied. However, in high-performance tokamak discharges, particularly in those with strong transport barriers, various effects including rotation, finite ion orbits, steep plasma gradients and boundary conditions can challenge the analytical expressions of neoclassical theory.

Typically transport in tokamaks is anomalous and greatly exceeds neoclassical predictions. However, in improved confinement regimes transport can remain near the neoclassical level [Chen et al., 2001]. Since collisional processes provide an irreducible minimum level of transport, an accurate estimate of the collisional contribution to transport is required in order to asses the relative importance of neoclassical and anomalous transport under given plasma conditions.

In spherical tokamak geometry it has been demonstrated that the collisional transport of particles may exceed the predictions of neoclassical theory due to finite Larmor radius effects [Gates et al., 2004; Romanelli et al., 2011] and due to finite drift orbit effects [Wang et al., 2006]. In such geometries the standard drift-ordering, used in the derivation of the averaged equations of particle motion in section 2.3, is no longer applicable and it is not possible to treat particle motion analytically. There is therefore a need for a reliable numerical simulation of collisional plasmas which can include the strong gradients associated with transport barriers and complex spherical tokamak geometries. The purpose of the present chapter is two fold: to develop a scheme for solving the standard set of neoclassical equations for a tokamak of arbitrary poloidal cross section and to use this scheme to compare the results of the Monte Carlo particle code CUEBIT against neoclassical theory.

4.1 Neoclassical transport codes

The neoclassical diffusion coefficients presented in section 2.4 are rather simplified. Rigorous calculation of neoclassical transport requires the self-consistent determination of the particle and heat fluxes of all plasma species in a manner that includes a description of the toroidal geometry and which is valid for all collisionality regimes. The modern approach to the solution of the neoclassical transport problem is the reduced charge state fluid description of Hirshman and Sigmar [1981], as reviewed by Helander and Sigmar [2002]. It is this approach that is typically adopted by neoclassical transport codes.

In general, classical fluxes are driven by perpendicular friction forces whilst neoclassical fluxes are driven by parallel forces, reflecting the different transport mechanisms of each of these processes. One may view neoclassical transport as originating from the collisional relaxation of the distribution of guiding centres, see section 2.3, to a Maxwellian, whereas the classical fluxes arise due to the gyro motion deviation from this guiding centre Maxwellian. Whilst both of the neoclassical fluxes are driven by a combination of toroidal curvature and particle collisions they are driven by different physical mechanisms [Helander and Sigmar, 2002]:

- in the Pfirsch-Schlüter regime, toroidal curvature gives rise to a vertical guiding centre drift, which drives a parallel return flow. Inter-particle collisions then impede (and dissipate) this flow, creating a parallel friction force and a parallel pressure gradient;
- in the banana-plateau regime, toroidal curvature and the related magnetic well produce an anisotropic guiding centre distribution. The resulting difference in parallel and perpendicular pressures produces a parallel viscous force.

Thus particle flux is typically expanded into classical (Cl), and banana-plateau and Pfirsch-Schlüter (BP and PS) neoclassical contributions:

$$\Gamma_\Psi = \langle \boldsymbol{\Gamma} \cdot \nabla \Psi \rangle = \Gamma_{\mathrm{BP}} + \Gamma_{\mathrm{PS}} + \Gamma_{\mathrm{Cl}}, \tag{4.1}$$

(a similar decomposition is made for the heat flux). Each of these contributions to the neoclassical fluxes remain distinguishable throughout all collisionality regimes. A number of codes have been written in order to solve the set of neoclassical transport equations for the particle flux and related transport coefficients, including NEOART [Peeters, 2000; Dux and Peeters, 2000] and NCLASS [Houlberg et al., 1997], which may be used in conjunction with plasma equilibrium codes in order to solve for the collisional transport coefficients is arbitrarily shaped plasma. The

typical procedure for determining the total particle flux for each plasma species is reviewed by Hirshman and Sigmar [1981] and the numerical implementation is summarised by Peeters [2000] and Houlberg et al. [1997].

The closure of the fluid equations typically employed in neoclassical theory makes a number of assumptions, the strongest of these is axisymmetry. Moreover, the closure assumes thin drift orbit widths, such that particles don't deviate very far form their initial flux surface, and small Larmor radius. This ensures that neoclassical transport is *local* and so solves for the radial transport of plasma species *for a single flux surface.*

During the present work the neoclassical transport code NCLASS [Houlberg et al., 1997] is used and extended in a number of ways. First, NCLASS is extended to solve for multiple (independent) radial grid points, allowing the calculation of transport coefficients across the plasma minor radius. Secondly, NCLASS is extended to allow for the specification of required flux surface geometry information using the CHEASE equilibrium code [Lütjens et al., 1992, 1996]. Previously, NCLASS assumed a simplified circular concentric flux surfaces model in order to calculate the geometric information describing the local flux surface of interest (required to solve the set of neoclassical equations). The assumption of concentric circular flux surfaces is clearly a poor approximation for the highly shaped MAST plasma.

In addition to the interface between the CHEASE and NCLASS codes, an interface between the CHEASE and EFIT [Lao et al., 1985] codes is developed to allow the use of experimentally determined equilibria. Thus a chain of codes, figure 4.1, is available which allows for the fast calculation of neoclassical transport coefficients for numerical, experimental or analytic plasma equilibria.

In should be noted that in addition to the assumptions made in neoclassical theory a number of further approximations are made in NCLASS. For example, it is assumed that a species flow velocity is small compared to the species thermal velocity. This is generally valid for bulk ions and electrons. However, particularly at tight aspect ratio, rotation is often supersonic when compared with impurity ion thermal speeds. Furthermore, NCLASS uses an approximate collision operator which yield viscosity coefficients which agree to within 20% of those calculated using a full collision operator [Houlberg et al., 1997]. So whilst neoclassical transport codes such as NCLASS allow a quick and flexible solution of the neoclassical equations for an arbitrary number of plasma species and tokamak geometry, one must be aware of a number of caveats and approximations employed in deriving the equations solved by such codes.

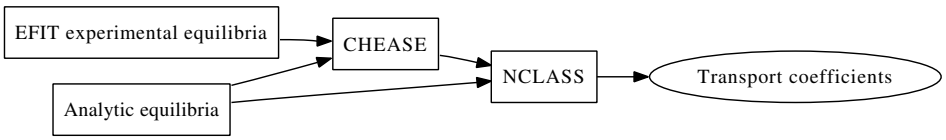

Figure 4.1: Chain of codes developed during the present work in order to solve for collisional transport coefficients. The interface between the CHEASE and NCLASS codes allows for the solution of the neoclassical transport equations for arbitrarily shaped tokamak plasmas, whether the equilibrium is specified analytically or from the reconstruction of experimental data.

4.2 Characterising transport in CUEBIT

CUEBIT solves the full orbit, single particle equation of motion and simply follows the trajectories of charged particles. With the addition of the Langevin terms discussed in the previous chapter the collisional dynamics of trace impurity ions may be solved for. In order to determine the transport resulting from these collisional terms and in order to compare this level of transport to the predictions of neoclassical theory a number of diagnostics have been incorporated into CUEBIT during the course of the present work.

4.2.1 Mean squared particle displacement

The first of these measures of transport is the mean squared particle displacement, which characterises the deviation of an ensemble of particles from their initial mean position [Tsang et al., 1975; Wong and Cheng, 1989] and can be related to the particle diffusion coefficient, D, through (see, for example, [Balescu, 2005, Chp. 11])

$$D = \lim_{t\to\infty} \frac{\mathrm{d}}{\mathrm{d}t} \left\langle \delta r^2(t) \right\rangle = \lim_{t\to\infty} \frac{\mathrm{d}}{\mathrm{d}t} \left\langle \left[r(t) - \langle r(t_0) \rangle \right]^2 \right\rangle . \tag{4.2}$$

Here r is a measure of the minor radius of the plasma, t is the simulation time, δr^2 is the *mean square displacement* of a particle and the angle brackets denote an average of the particle ensemble. For purely collisional transport the mean square displacement behaves linearly in time in the limit of long time [Balescu, 2005].

Clearly particle diffusivity is a function of the local rate of collisions. With gradients in the bulk ion density or temperature the diffusion coefficient becomes a function of space. In order to determine the diffusion coefficient locally on a flux surface the calculation must therefore be limited in time so that particles are not transported far from the flux surface of interest and so as not to calculate a configuration space averaged diffusion coefficient. Figure 4.2 demonstrates the

mean squared particle displacement of 10^4 C^{6+} ions initially released from a mid minor radius, demonstrating the linear behaviour of the mean square displacement in time.

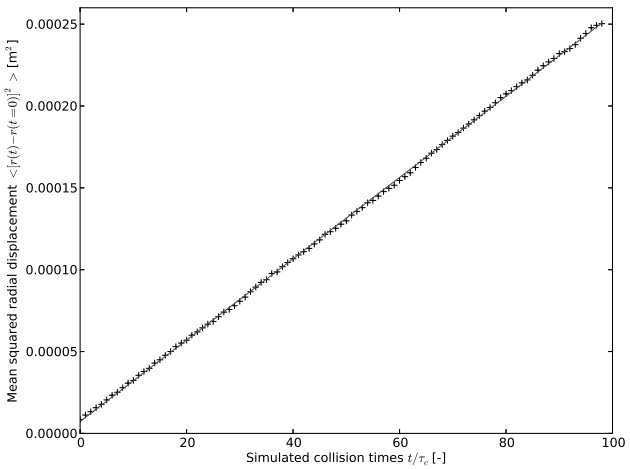

Figure 4.2: Mean squared displacement calculated for 10^4 C^{6+} ions in a MAST-like Solov'ev equilibrium. Time is normalised to the impurity-ion collision time.

4.2.2 Particle fluence

In addition to measuring the diffusion of particles directly we can also estimate this quantity from the flux of particles passing through a magnetic surface. In order to compute this particle flux CUEBIT is extended to include a Monte Carlo calculation of the particle *fluence*, that is the time integral of the particle flux [Kiviniemi et al., 2000; Heikkinen et al., 2001]. The particle fluence is calculated by counting the number of particles crossing a particular flux surface in a unit time and using the equation

$$\mathcal{F}(\Psi) = \frac{w_p \Delta\mathcal{N}}{\mathcal{A}(\Psi)\Delta t}. \tag{4.3}$$

Here $\Delta\mathcal{N}$ is the total number of particles crossing the flux surface Ψ during one integration time step, Δt, and $\mathcal{A}(\Psi)$ is the area of this flux surface. A positive value of $\Delta\mathcal{N}$ indicates that more particles which have crossed the flux surface are travelling radially outwards than radially inwards and a negative $\Delta\mathcal{N}$ indicating the opposite case. The particle weight, w_p, is taken simply to be the reciprocal of the total number of particles simulated and is the same for all particles, which ensures that the particle fluence calculated is independent of the number of test particles in the

simulation. This is demonstrated in the convergence study presented in figure 4.3. More generally this quantity may be different for each particle. Typically it is defined such that arbitrary initial density profiles may be simulated whilst reducing statistical noise: particles are loaded uniformly in phase-space, ensuring that all regions are simulated and there are no sparse volumes, and a weight is assigned to particle to give a prescribed density profile.

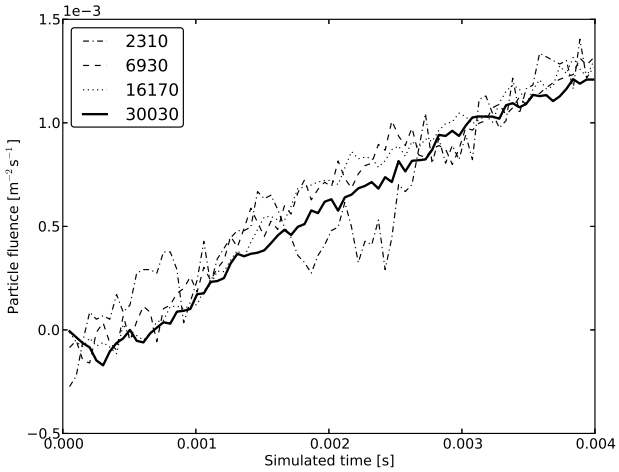

Figure 4.3: Convergence of the particle fluence with increasing number of simulated particles.

Rather than computing particle flux as the time derivative of the fluence, many guiding centre and gyrokinetic particle codes compute the particle flux directly as the flux surface average of the radial velocity component of particles which lie on that surface using

$$\Gamma_\Psi = \left\langle \frac{w_p \mathbf{v} \cdot \nabla\Psi}{\nabla\Psi} \right\rangle . \tag{4.4}$$

However, this was found to be a poor method to use in CUEBIT, since the gyro motion was a significant contribution to this quantity (in guiding centre codes, for example, only the slower drift motion contributes to this flux). During one gyro-period a particle will contribute for half this time an outward flux and for the other half a large inward flux, which makes it difficult to discern the smaller average cross surface flux.

4.3 Comparison to neoclassical theory

Having developed both a code which solves for the collisional dynamics of test ions in arbitrary tokamak geometries and the interfaces between a collection of codes to solve the set of neoclassical transport equations the present section aims to compare the collisional diffusivities calculated using CUEBIT and NCLASS in order to test the treatment of collisions in CUEBIT. In this section a more thorough neoclassical benchmarking of the CUEBIT code than in the work of Romanelli et al. [2011], which compared the diffusion coefficients calculated by CUEBIT in the case of large aspect ratio with the simple heuristic estimates of the particle transport coefficients discussed in section 2.4, is presented.

4.3.1 Large aspect ratio comparison

CUEBIT uses a Solov'ev plasma equilibria model, as detailed in section 2.2.3, whereas NCLASS does not assume a particular model but requires a number of geometric properties of the flux surface of interest. The example driver program provided with NCLASS however assumes a circular concentric flux surfaces model [Lapillonne et al., 2009]. In the first comparison presented here, that of a large aspect ratio plasma, we use this simplified model as input to NCLASS. It must therefore be ensured that the equilibrium models employed in the two codes match as closely as possible. In figure 4.4 we plot the average difference in the total magnetic field strength on a flux surface between the Solov'ev and circular surfaces models for the parameters given in table 4.1. Since the toroidal magnetic field employed in both models is identical the difference arises from the poloidal magnetic field, the strength of which is controlled by the specification of q_0, the on axis safety factor values, in the circular surfaces model used by NCLASS and I_P, the total toroidal current, in the Solov'ev model.

The toroidal plasma current in the Solov'ev model was chosen to minimise, as far as possible, this difference between the magnetic field strengths in the two models. The increasingly significant discrepancy with minor radius between the two models arises from the safety factor profile employed: in calculating the ad-hoc model quantities a flat safety factor profile was used, which is not a valid solution to the Grad-Shafranov (GS) equation. The Solov'ev solution is strictly a solution to GS equation and so will not exactly match the circular surfaces model. However, at the flux surface of interest, with a normalised minor radius of 0.5, the difference between the two models is $\lesssim 1\%$.

In order to compare the results of CUEBIT with the impurity diffusion coeffi-

	Circular surfaces model	Solov'ev model
R_0 [m]	3	3
ϵ [-]	0.1	0.1
$B_{\mathrm{T},0}$ [T]	3	3
q_0 [-]	-3	—
I_p [A]	—	-1.5×10^5
κ [-]	—	1

Table 4.1: Parameters used to achieve a correspondence between the circular surfaces and Solov'ev models in the case of a large aspect ratio tokamak equilibrium.

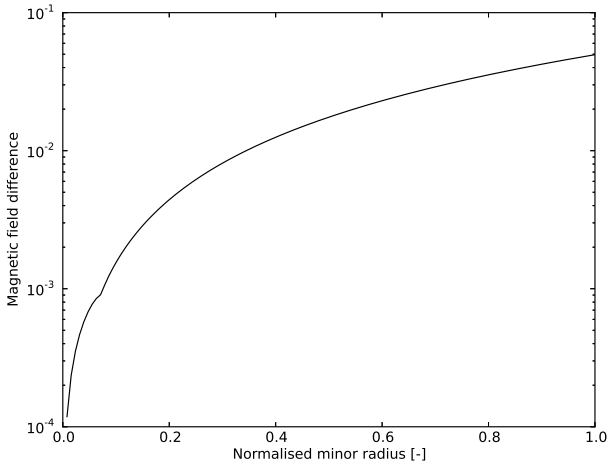

Figure 4.4: Comparison of the total magnetic field strength calculated for a large aspect ratio tokamak equilibrium using the ad-hoc concentric circular flux surfaces model and the analytic Solov'ev model. The measure of the difference between the magnetic field strengths between the two models is calculated as $\Delta B(r_i) = \frac{1}{n_\theta} \sum_{i=1}^{n_\theta} |B(r_i, \theta_i)^{\mathrm{Solov'ev}} - B(r_i, \theta_i)^{\mathrm{circular}}|$.

cient calculated by NCLASS 10^4 C^{6+} ions, all released from the flux surface $\psi = 0.5$ (with ψ the normalised poloidal flux) with a uniform distribution in poloidal angle, were simulated using CUEBIT. The mean squared displacement of the ions was then used, as described above, to compute the corresponding diffusion coefficient, see figure 4.5. This comparison between CUEBIT and NCLASS was repeated for a range of values of the bulk ion density and with zero density gradient and fixed values of the bulk ion temperature, 2 keV, and temperature gradient, -0.14 keV m^{-1}. The bulk ion density was varied from 4×10^{18} m^{-3} to 10^{21} m^{-3}. This yields a scaling of the diffusion coefficient with the normalised collision frequency (see section 2.4.2), which is in the range 0.006 to 5.556 for the bulk ion density and temperature values

quoted here.

It is found that the calculations of CUEBIT in the Pfirsch-Schlüter regime underestimate the diffusion coefficient, compared with the NCLASS prediction, when the parallel friction force of section 3.6.1 is included in the simulation. Rerunning these particular simulations without the parallel friction force, which is strictly valid only in the banana regime, yields a broad agreement between the two codes, see figure 4.5. We therefore find that the scaling of the impurity diffusion coefficient calculated by CUEBIT is as expected from neoclassical theory and the NCLASS simulations. Plotting this figure on a linear scale reveals the expected scaling from figure 2.5. We may therefore have confidence that CUEBIT is capturing the key features of collisional impurity transport in large aspect ratio tokamak plasmas.

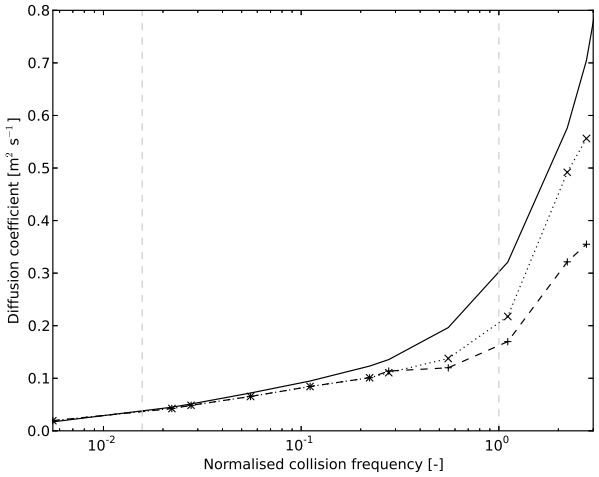

Figure 4.5: Comparison of particle diffusion coefficients calculated by NCLASS (solid line) and CUEBIT (broken lines) in a simplified, large aspect ratio concentric circular flux surface equilibrium. Diffusion coefficients were calculated both with (- - - -) and without ($\cdots\cdots$) the parallel friction force included in CUEBIT.

One area for further investigation is the investigation of the minor radial variation of transport coefficients. CUEBIT and NCLASS are in broad agreement for this large aspect ratio case. However the model employed by NCLASS in known to be limited close the the magnetic axis and plasma edge, quoting Houlberg et al. [1997]:

> It must be cautioned that although the model [employed in NCLASS] takes a step toward a more self-consistent treatment of neoclassical effects, it is still incomplete. First, none of the models considered here are

> applicable within a banana width of the plasma edge because ion orbit losses violate the assumptions made in the derivation of the viscosity... Second, near the axis real ion orbits are also not well represented by the approximation of orbits concentric about the axis and thin relative to the minor radius made in the kinetic determination of the viscosity.

It would be interesting to observe whether the agreement between NCLASS and CUEBIT diverges near the plasma edge or core.

4.3.2 Spherical tokamak comparison

We continue to compare the treatment of collisional transport in CUEBIT against NCLASS, this time at tight aspect ratio. In this case the CHEASE code, using the plasma boundary and equations for the pressure gradient and ff' from the Solov'ev equilibrium model as inputs, is used to calculate and prescribe the flux surface information required by NCLASS. In this case we are therefore using the same equilibrium model in both CUEBIT and NCLASS, with the model parameters listed in table 4.2. Again comparing the diffusion coefficients as calculated by NCLASS and CUEBIT for a range of normalised collision frequencies we see from figure 4.6 that the discrepancy between the two codes is larger than in the large aspect ratio case. In this case the bulk ion density was varied between 1.3×10^{18} m^{-3} and 1.25×10^{20} m^{-3} and the bulk ion density gradient, temperature and temperature gradient were fixed at 0, 0.2 keV and -0.246 keV m^{-1} respectively.

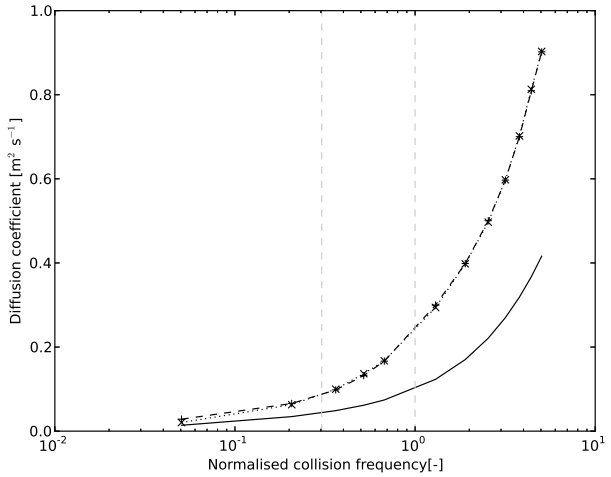

Figure 4.6: Comparison of particle diffusion coefficients calculated by NCLASS (solid line) and CUEBIT (broken lines) for a tight aspect ratio plasma equilibrium.

In order to ensure that this discrepancy was not due to the use of an equilibrium code in NCLASS the correct treatment of CHEASE equilibria in NCLASS was verified. The diffusion coefficient computed for 10^4 Ne^{10+} ions in both an analytically and a numerically prescribed large aspect ratio circular tokamak equilibrium were compared, with the numerical CHEASE solution matched exactly to the circular surfaces model at the plasma boundary. We see from figure 4.7 that the diffusion coefficient and advection velocity match in both cases. Thus we can be confident that the discrepancy between NCLASS and CUEBIT in this spherical tokamak comparison case is a result of moving to tight aspect ratio, rather than due to the use of the numerical CHEASE equilibria, which was not used in the large aspect ratio case.

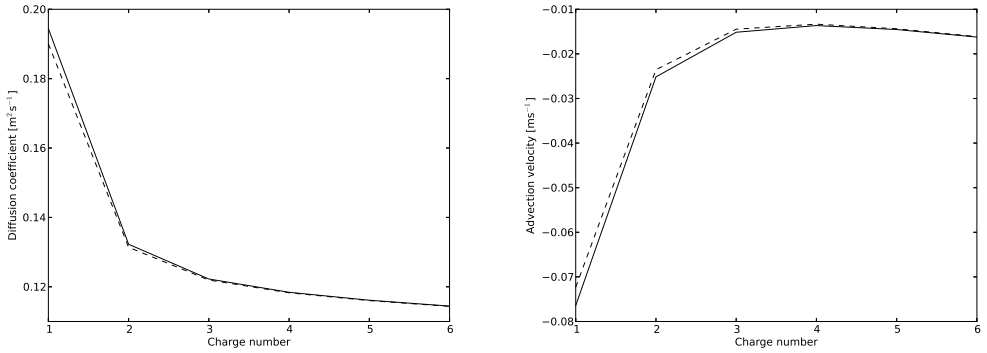

Figure 4.7: Comparison of diffusion coefficient (left) and advection velocity (right) for 10^4 Ne^{10+} ions calculated using NCLASS with a simplified concentric circular flux surface equilibrium (solid line) and an equilibrium calculated using CHEASE (dashed line).

This discrepancy between the CUEBIT and NCLASS results at tight aspect ratio is consistent with other investigations of collisional transport in global spherical tokamak geometries. For example, Gates et al. [2004] demonstrated that finite Larmor radius effects can enhance the rate of collisional transport by over a factor of 2 compared with that calculated using a guiding centre code. This is because at tight aspect ratio particle Larmor radii can be comparable to drift orbit widths. Essentially, at tight aspect ratio, the level of classical transport can be comparable to neoclassical transport, enhancing the overall level of collisional transport significantly. Furthermore, Wang et al. [2006] demonstrated that finite drift orbit widths can also enhance the level of observed collisional transport if particle drift orbit widths are a significant fraction of the plasma minor radius. This demonstrates a limitation of the local calculations employed in NCLASS and other neoclassical

codes at tight aspect ratio.

Furthermore, at transport barriers the bulk ion temperature or density profiles can vary strongly on the scale of the ion orbit width, requiring a global (non-local) calculation that does not rely on the conventional neoclassical expansion. A number of attempts have been made recently in order to incorporate the effects of finite drift orbit widths in neoclassical calculations in both particle-in-cell (PIC) codes [Wang et al., 2006] and in continuum codes [Landreman and Ernst, 2012a,b] in order to overcome these limitations we mention and have demonstrated in the present chapter.

Plasma equilibrium parameters	
Major radius, R_0 [m]	3
Inverse aspect ratio, ϵ [-]	0.65
Normalising magnetic field, $B_{\mathrm{T},0}$ [T]	0.4
Plasma current, I_{p} [A]	-1×10^6
Plasma elongation, κ [-]	2

Table 4.2: Solov'ev equilibrium parameters used to model the MAST plasma. Except where noted these parameters are used throughout the remainder of the present thesis to represent a tight aspect ratio plasma.

4.3.3 Diffusion coefficient error estimate

The tight aspect ratio simulations of the previous section corresponding to a normalised collision frequency, ν^*, of 0.2066, 0.5188, 1.2993 and 2.5481 were repeated a further ten times, each with different initial random seeds, in order to estimate the error associated with the results presented above. The results of averaging the computed diffusion coefficient for each of these sets of ten simulations are presented in the table below. We see that the use of 10^4 test particles and an average over ten realisations provides an accurate estimate of the test particle diffusion coefficient.

ν^*	Diffusion coefficient [$\mathrm{m}^2\ \mathrm{s}^{-1}$]
0.2066	0.065 ± 0.001
0.5188	0.135 ± 0.003
1.2993	0.294 ± 0.003
2.5481	0.498 ± 0.007

Table 4.3: Particle diffusion coefficients and associated error estimates, each calculated as the standard deviation of 10 realisations of CUEBIT.

Chapter 5

Full orbit simulations of collisional impurity transport in spherical tokamak plasmas with strongly-sheared electric fields

In the previous chapters the development of a test particle transport code which includes finite Larmor radius effects and is applicable to global spherical tokamak (ST) geometries is described. The correspondence between the results of this code and the predictions of neoclassical theory was demonstrated. In the present chapter we apply this code in order to investigate the impact of strong, sheared electric fields on the transport of impurity ions in a MAST-like equilibrium. The key results from this chapter have been submitted for publication to *Plasma Physics and Controlled Fusion* and have appeared in the 38^{th} proceedings of the EPS Conference on Plasma Physics.

5.1 The radial electric field

The radial electric field is an important feature of high performance tokamak discharges due to it's role in the regulation of anomalous transport and the transition from low to high confinement modes [Rogister, 1998] and will likely be a feature of the baseline operating regime for ITER [Shimada et al., 2007]. The structure of the electric field determines the rate of $\mathbf{E} \times \mathbf{B}$ shear flow stabilisation of turbulent transport, thought to be the underlying mechanism generating transport barriers [Meyer et al., 2011], that is regions of the plasma with reduced levels of transport.

The origin of the radial electric field may been seen from the fluid momentum force balance equation, which can be written in the form (see, for example [Braginskii, 1965; Ida, 1998; Callen et al., 2010])

$$m_s n_s \frac{\mathrm{d}\mathbf{V}_s}{\mathrm{d}t} = n_s Z_s e \left(\mathbf{E} + \mathbf{V_s} \times \mathbf{B}\right) - \nabla p_s - \nabla \cdot \pi_s + \mathbf{F}_s + \mathbf{S}_s, \tag{5.1}$$

where s denotes the plasma species, $\mathbf{V}_s$ is the species flow velocity and p_s, π_s and $\mathbf{F}_s$ are pressure, viscosity and the friction force acting on species s and $\mathbf{S}_s$ denotes a source of this species. Neglecting the inertia, friction, viscosity and sources the radial electric field is approximated by the pressure gradient and Lorentz terms [Meyer et al., 2008],

$$E_r \simeq \frac{1}{n_s Z_s e}\frac{\mathrm{d}p}{\mathrm{d}r} + V_s^{\varphi} B_\theta - V_s^{\theta} B_\varphi. \tag{5.2}$$

We therefore find that a radial electric field is supported by a radial pressure gradient and toroidal and poloidal flows of the plasma. It should be noted that whilst there is an equation of the form (5.2) for each plasma species, the electric field which appears in these equations is the same for all species. In order to determine the radial electric field one typically uses impurity rotation velocities, determined using Doppler spectrometry, the pressure gradient determined using the same diagnostic and the poloidal and toroidal magnetic field components determined by equilibrium reconstruction, using, for example, EFIT [Meyer et al., 2008].

In MAST a strongly-sheared, inward directed radial electric field is observed close to the plasma edge in H-mode (see figure 5.1a), consistent with the general observation of a strong radial electric field during H-mode on other tokamak devices [ASDEX Team, 1989; Ida, 1998; McDermott et al., 2009; Meyer et al., 2011]. We see from figure 5.1a the evolution of the edge radial electric field through an L-H transition, that is the transition from L-mode to H-mode, during which the electric field strength increases to a peak value of approximately -15 kVm^{-1} with a full width at half maximum of the order of the bulk ion Larmor radius. In L-mode the radial electric field has a peak value of less than -5 kVm^{-1} and is broader than in H-mode, figure 5.1b. The contributions to the electric field in L-mode are indicated on this figure: we see that the radial electric field is closely approximated by the sum of the diamagnetic and Lorentz terms of the momentum balance equation, justifying our neglect of the viscosity, inertia and friction terms from (5.2).

In the remainder of this chapter we neglect bulk rotation of the main ions and therefore assume that the radial Lorentz force is sub-dominant to the pressure gradient term in the radial component of the bulk ion fluid momentum balance equation. This assumption is consistent with reported measurements of temperatures,

densities and flows in the vicinity of ETBs in MAST L-mode plasmas, as presented in figure 5.1b and reported elsewhere [Meyer et al, 2009; Field et al., 2009]: the pressure gradient is typically several tens of kPa m^{-1} whereas the contributions of poloidal and toroidal flows to the radial component of the Lorentz force are typically around one or two kPa m^{-1} at most.

CUEBIT has previously been used to study the influence of bulk plasma rotation on impurity transport [McKay et al., 2008; McClements and McKay, 2009]. In order to separate the physics of the radial electric field and plasma rotation we consider only the former herein. It should be noted however, that whilst the radial electric field is close to the diamagnetic term in the ion momentum force balance in L-mode, in H-mode a significant $\mathbf{V} \times \mathbf{B}$ contribution can arise (see, for example [Burrell et al., 1994]).

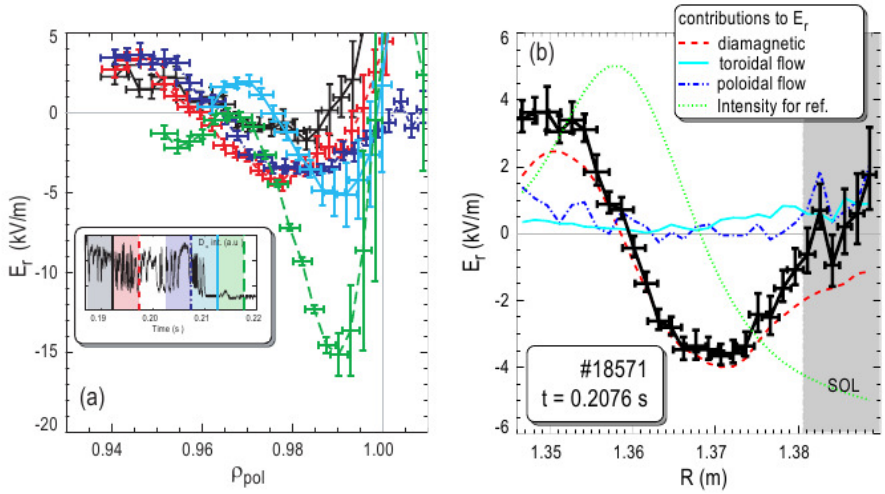

Figure 5.1: (a) Time evolution of the radial electric field in the edge of a MAST plasma through the L-H transition, measured in L-mode (red, black and blue curves) and H-mode (light blue and green curves). A negative, strongly sheared radial electric field develops in H-mode. (b) The contributions to the radial electric field in an L-mode MAST plasma, demonstrating the key role of the pressure gradient term in (5.2), [Meyer et al., 2008].

5.2 Orbit squeezing

The motion of a charged particle in electromagnetic fields is fundamental to many theories in plasma physics, including neoclassical theory. Generally, analytic discussions of such motion rely on the guiding centre approximation, as discussed in section 2.3, which decomposes the particle motion into parallel streaming along the

magnetic field, fast gyro motion about the field and a slower drift motion across the field. This treatment of the guiding-centre problem, however, is valid only for a strong but slowly varying magnetic field, possibly combined with a small and slowly varying electric field. These idealised assumptions and not generally valid, particularly in tokamak plasmas where strongly sheared electric fields are often employed to improve plasma performance, and the standard drift ordering,

$$\frac{\rho}{L_B} \ll 1, \quad \frac{\rho_p}{L_E} \ll 1 \tag{5.3}$$

with $L_n = (\mathrm{d}\ln n/\mathrm{d}r)^{-1}$ the gradient length scale of the quantity n, fails to be satisfied. As discussed above, electric fields in tokamaks can vary on scales approaching the ion banana width, either close to a transport barrier or in the plasma edge, where there may be steep electrostatic potential gradients. The electric field is then able to distort particle orbits, a phenomenon referred to as *orbit squeezing* or *orbit shrinking*, depending on the effect on the orbit. The influence of the radial electric field on trapped particles trajectories is most prominent for ripple-trapped particles [Itoh and Itoh, 1996]. However, the banana orbit [Shaing and Hazeltine, 1992; Krasheninnikoy and Yushmanoy, 1994; Hinton and Kim, 1995] and the gyro motion [Shaing et al., 1998] can both be modified if the electric field gradient becomes strong enough. This can have important consequences for the transport of particles and heat in advanced tokamak operation regimes. Since strong radial electric field gradients squeeze banana orbits all neoclassical processes, including ion thermal conduction, particle diffusivity and the bootstrap current, are correspondingly modified [Burrell et al., 1994; Shaing and Zarnstor, 1997; Rogister, 1998].

In the present chapter we elucidate the effects of a strongly sheared electric field on particle trajectories in spherical tokamaks and the consequences for collisional transport, motivated by the observation of the role of a strongly-sheared electric field in the L-H transition and in transport barrier formation. A number of authors have previously discussed the present problem. However, it shall be demonstrated that their analytical results tend to be rather limited when attempting to apply these results to experimental observations of the radial electric field.

5.2.1 Gyro motion squeezing

Conventional magnetised orbit theory, see section 2.3, is not applicable in the case of strongly sheared electric fields if the field variation length scale is of the order of the particle gyro-radius [Shaing et al., 1998]. Thus we return to the exact equation

of motion of a charged particle, the Lorentz force law,

$$\frac{\mathrm{d}\mathbf{v}}{\mathrm{d}t} = \frac{Ze}{m_z}\left(-\nabla\Phi + \mathbf{v}\times\mathbf{B}\right), \tag{5.4}$$

where m_z is the particle mass and Ze is the particle charge. In the following we use Cartesian coordinates, (x, y, z), and assume a uniform magnetic field, $\mathbf{B} = B\hat{\mathbf{z}}$. Furthermore, we assume that the electrostatic potential varies only in x, which yields an $\mathbf{E}\times\mathbf{B}$ drift velocity

$$\mathbf{v}_{\mathrm{E}\times\mathrm{B}} = \frac{\Phi'(x)}{B}\hat{\mathbf{y}}, \tag{5.5}$$

where the prime indicates a spatial derivative in the x-direction. The x and y components of (5.4) are

$$\frac{\mathrm{d}v_x}{\mathrm{d}t} = +\frac{Ze}{m_z}v_y B - \frac{Ze}{m_z}\Phi', \tag{5.6a}$$

$$\frac{\mathrm{d}v_y}{\mathrm{d}t} = -\frac{Ze}{m_z}v_x B. \tag{5.6b}$$

Differentiating the y-component with respect to time, we find that

$$\ddot{v}_y = -\Omega^2\left[v_y - \frac{\Phi'}{B}\right]. \tag{5.7}$$

where $\Omega = ZeB/m_z$ is the usual cyclotron frequency. Repeating this procedure for the x-component, we have

$$\ddot{v}_x = -Ze\frac{\mathrm{d}\Phi'}{\mathrm{d}t} + ZeB\dot{v}_y = -\Omega^2\left[1 + \frac{\Phi''}{\Omega B}\right]v_x. \tag{5.8}$$

where we have used that $d\Phi'/dt = \Phi'' v_x$. We define an effective cyclotron frequency

$$\Omega_* = \Omega\sqrt{1 + \frac{\Phi''}{\Omega B}}. \tag{5.9}$$

It is clear from (5.8) that the effect on particle motion by a sheared electric field will become important when the shear parameter, $\Phi''/\Omega B$, approaches minus unity [Tao et al., 1993]. We therefore find that, in the y-direction, we have the usual gyro motion plus the $\mathbf{E}\times\mathbf{B}$ drift. However, in the x-direction we have defined an effective cyclotron frequency. Particle motion in this direction is therefore not simply described by the usual circular periodic motion.

5.2.2 Drift-orbit squeezing

In addition to the gyro-motion distortion derived above, particle drift orbits may also be distorted by a sheared radial electric field. In order to demonstrate this we return to the particle constants of motion and the averaged gyro-averaged particle description of 2.3. Extending the derivation of the trapped particle orbit width outlined at the end of section 2.3.3 to include an electrostatic potential $\Phi(r)$, following Hazeltine [1989] and Hinton and Kim [1995], we find that the width of the banana orbit is modified such that

$$r - r_0 = -\frac{2v_{\parallel,0}}{S\Omega_p} \tag{5.10}$$

in the outboard mid-plane. In contrast to the width derived in the absence of an electrostatic potential, (2.85), the above expression is dependent on the *orbit squeezing factor*

$$S = 1 + \frac{m\Phi''}{ZeB_{\mathrm{P}}}. \tag{5.11}$$

When this factor is greater than 1, the width of a trapped particle orbit is smaller than the corresponding width in the case where $\Phi'' = 0$. In addition to the shrinking of drift orbit widths, the inclusion of a sheared electric field in the particle equations of motion leads to a modification of the trapped-passing particle boundary [Shurygin and Dewar, 1995].

5.3 Collisionless orbits and a sheared electric field

The effect of a sheared radial electric field, leading to both gyro-orbit and drift-orbit distortion, is illustrated in figure 5.2. Here an inward direction, sheared radial electric field, $\mathbf{E} = -\nabla\Phi$, has been simulated in a MAST-like plasma equilibrium using a flux function electrostatic potential of the form

$$\Phi(\Psi) = \Phi_0 \arctan\left(\frac{\Psi - \Psi_1}{\Delta\Psi}\right), \tag{5.12}$$

where Ψ_0, Ψ_1 and $\Delta\Psi$ are the potential barrier height, location in Ψ space and width in Ψ space, respectively. The measurements reported by Meyer et al. [2008] of edge radial electric fields in MAST H-mode plasmas (see figure 5.1, above) indicate that the corresponding potential profile is approximately of the form given by (5.12) and that these constants have typical values of $\Psi_0 = 60$ V and $\Delta\Psi = 1.35 \times 10^{-3}$ Tm^2. We choose, for the time being, to centre the electric field structure on $\Psi_1 = 0.6\Psi(R_0, 0) = -0.4$ Tm^2.

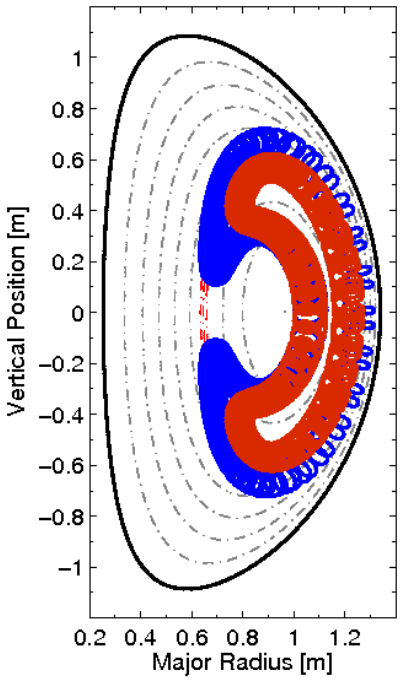

Figure 5.2: Comparison of the trajectory of an Ar^{12+} ion in a MAST-like equilibrium without (blue solid curve) and with (red solid curve) a sheared radial electric field, demonstrating both orbit and qyro motion squeezing. Red dashed curves indicate the positions of the peak and full width at half maximum of the radial electric field.

For our particular choice of equilibrium, characterised by the parameters given in table 4.2, these quantities correspond to a physical location and width in the outboard mid plane ($Z = 0$) plane of $R_1 = 1.2$ m and $\Delta R = 1.1$ cm respectively. The corresponding peak electric field strength, E_0, is -10.5 kVm^{-1}, which is close to measured values in MAST ETBs [Meyer et al., 2008]. The form of this prescribed electric field along the outboard mid plane is shown in figure 5.3, which clearly illustrates a limitation of using the orbit squeezing model discussed above, namely, which value of the squeeze factor to use when characterising the impact of the electric field on particle motion. In addition to a radial electric field, the inward Ware pinch [Ware, 1970] is modelled approximately with a $1/R$ dependency of the toroidal electric field, with $E_\phi = -0.3$ Vm^{-1} at the magnetic axis.

We note that no attempt is made to model a self-consistent bulk ion distribution. For example, the bulk ion temperature and density profiles and the equilibrium pressure gradient are chosen independently. Furthermore, this pressure gradient, assumed to be a linear function of the poloidal flux in the derivation of the Solov'ev solution, is not consistent with the strongly sheared radial electric field derived from (5.12), although it has been chosen to be of the correct magnitude to support such values of the radial electric field. In the present work we are concerned with the role of a strongly sheared radial electric field on test impurity transport, not on the

combined effects of such a field and strong gradients in the background bulk ion distribution. Future quantitative investigations will need to consider a self-consistent background plasma equilibrium.

Solving for the trajectory of an Ar^{12+} ion using CUEBIT, both with and without the prescribed electric field of a shrinking of the particle gyro-orbit in the outboard mid plane and the change in location of the orbit bounce points are clearly visible, see figure 5.2.

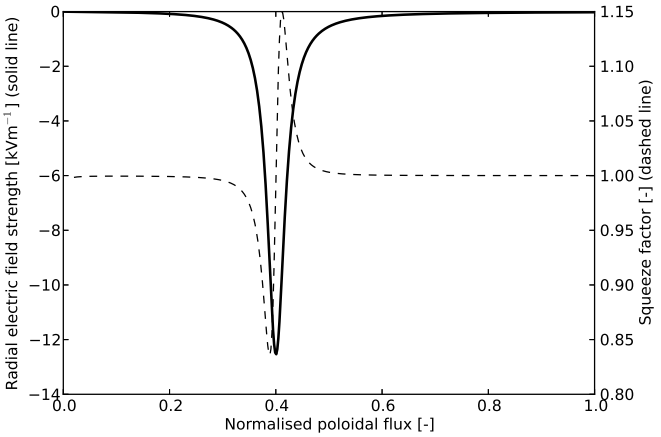

Figure 5.3: Form of the prescribed electric field (solid line) and corresponding squeeze factor for a C^{6+} (dashed line) ion in the outer mid-plane of a MAST-like equilibrium. The full-width half-maximum of the radial electric field is chosen to be equal to the bulk ion gyroradius evaluated at the location of maximum electric field. The squeeze factor is calculated from $S = 1 + Ze\Phi''(r)/m_z\Omega_p^2$.

It is also found that just-passing particles can become trapped under the influence of a sheared electric field. We therefore find that the effect of a sheared radial electric field on *collisionless* particle orbits is to increase the trapped particle fraction and reduce the orbit width of trapped ions. For the remainder of the present chapter we are interested in the role of a sheared radial electric field on the *collisional* dynamics of test particle ions.

5.4 Collisional particle dynamics and the radial electric field

5.4.1 Preliminary simulations

Given the prescribed electric field derived from (5.12) we investigate the effect of this field on the the collisional dynamics of ions of various species. We simulate separately 10^4 He^{2+}, C^{6+}, Ne^{10+} and W^{20+} ions, with each initialised on the magnetic axis and allowed to diffuse and fill the plasma volume, interacting with the inward radial electric field. The flux surface averaged test particle densities after 100 ms (approximately 1000 collision times) are presented in figure 5.4, both with and without the electric field.

It is clear that in the absence of the electric field, figure 5.4a, the distribution of the test particles of all species are broadly the same, as expected from neoclassical theory. However, in the presence of the electric field, figure 5.4b, a step in the density profiles is observed with the greatest step occurring for the high mass, high charge state W^{20+} ions. This indicates that the inward radial electric field is acting to impede the outward diffusion of the test particles, increasing the confinement of the particles. This is further evident in the poloidal distribution of the He^{2+}, Ne^{10+} and W^{20+} ions in the presence of the electric field, figure 5.5.

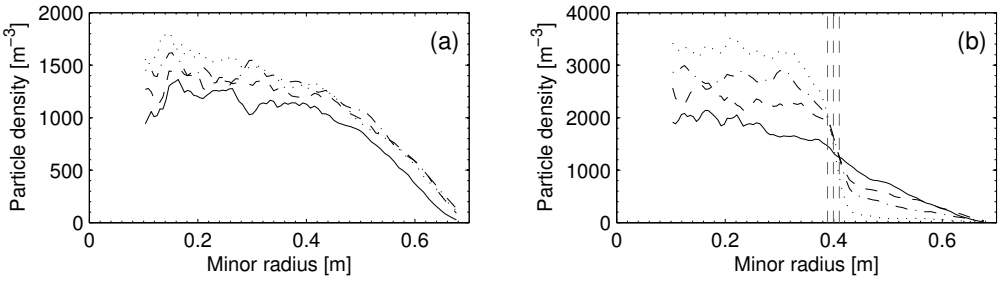

Figure 5.4: Test impurity ion density profiles against minor radius, both without (a) and with (b) a sheared radial electric field. Simulated ions are He^{2+} (——), C^{6+} (– – –), Ne^{10+} (— · —) and W^{20+} (· · · · · ·). Vertical lines in (b) indicate the peak strength and full-width half-maximum positions of the sheared radial electric field.

5.4.2 Characterising transport: the drag force drift

In order to begin to explain the particle species dependency of the effect of the radial electric field on the outward diffusion of test particles we return to the single particle picture of collisional particle dynamics, that is the Lorentz-Langevin equation of

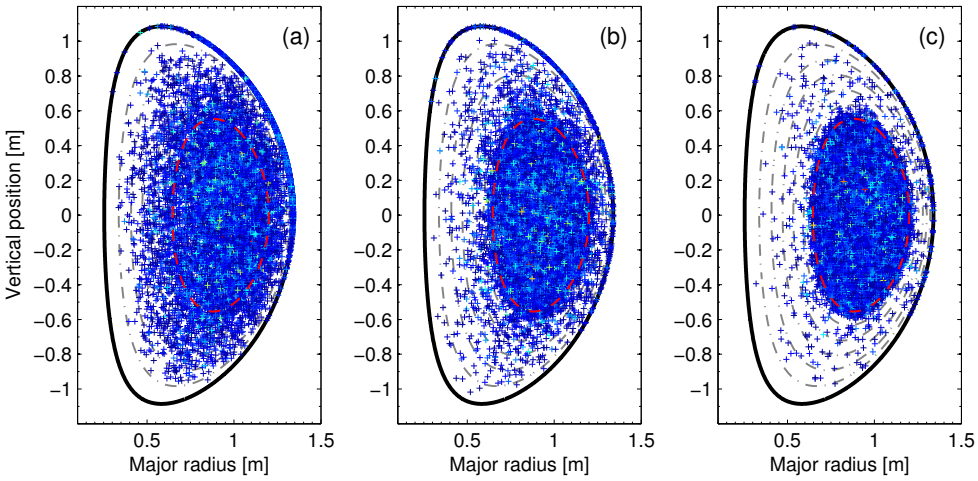

Figure 5.5: Poloidal distribution of (a) He^{2+}, (b) Ne^{10+} and (c) W^{20+} ions in a MAST-like equilibrium with a radially sheared electric field, the position of which is indicated by a dashed red line.

section 3.5,

$$m\frac{\mathrm{d}\mathbf{v}}{\mathrm{d}t} = Ze\left(\mathbf{E}+\mathbf{v}\times\mathbf{B}\right) - \frac{m}{\tau_{\mathrm{zi}}}\left(\mathbf{v}-\mathbf{u}\right) + m\mathbf{a}_r. \tag{5.13}$$

In order to proceed analytically we neglect the stochastic term $\mathbf{a}_r$ and assume a constant bulk rotation of the plasma, in other words $\mathbf{u} = \textit{constant}$. Noting that an ODE of the form

$$\frac{\mathrm{d}x}{\mathrm{d}t} + ax = 0 \tag{5.14}$$

may be re-written as

$$e^{-at}\frac{\mathrm{d}}{\mathrm{d}t}\left(e^{at}x\right) = 0, \tag{5.15}$$

we rearrange the above equation of motion to read

$$\frac{\mathrm{d}\mathbf{w}}{\mathrm{d}t} = \mathbf{w}\times\boldsymbol{\Omega} + \mathbf{F}e^{\nu_{\mathrm{zi}}t}, \tag{5.16}$$

where we have introduced $\mathbf{w} = \exp\left(\nu_{\mathrm{zi}}t\right)\left(\mathbf{v}-\mathbf{u}\right)$ and $\mathbf{F} = \mathbf{u}\times\boldsymbol{\Omega}+\Omega B^{-1}\mathbf{E}$. Assuming that $\mathbf{B} = B\hat{\mathbf{z}}$ and $\mathbf{E} = E_\perp\hat{\mathbf{x}}$ we may write

$$\dot{\omega}_{\mathrm{x}} = \Omega\omega_{\mathrm{y}} + F_{\mathrm{x}}e^{\nu_{\mathrm{zi}}t}, \tag{5.17a}$$

$$\dot{\omega}_{\mathrm{y}} = -\Omega\omega_{\mathrm{x}} + F_{\mathrm{y}}e^{\nu_{\mathrm{zi}}t}. \tag{5.17b}$$

Solving the above equations for $\Omega_{\rm x}$ and $\Omega_{\rm y}$ we find that

$$\omega_{\rm x} = C\sin\Omega t + D\cos\Omega t + \frac{\nu_{\rm zi}F_{\rm x} + \Omega F_{\rm y}}{\nu_{\rm zi}^2 + \Omega^2}e^{\nu_{\rm zi}t}, \tag{5.18a}$$

$$\omega_{\rm y} = -C\cos\Omega t + D\sin\Omega t + \left[\frac{F_{\rm y}}{\nu_{\rm zi}} - \frac{\Omega}{\nu_{\rm zi}}\frac{\nu_{\rm zi}F_{\rm x} + \Omega F_{\rm y}}{\nu_{\rm zi}^2 + \Omega^2}\right]e^{\nu_{\rm zi}t}. \tag{5.18b}$$

Solving for $v_{\rm x}$ and $v_{\rm y}$, rather than $\omega_{\rm x}$ and $\omega_{\rm y}$, and applying appropriate initial conditions we find that

$$v_{\rm x} = v_\perp e^{-\nu_{\rm zi}t}\cos\Omega t + \frac{E_\perp}{B}\frac{\nu_{\rm zi}}{\Omega}\frac{1}{1+\nu_{\rm zi}^2/\Omega^2} + \left(u_{\rm x}\frac{\nu_{\rm zi}}{\Omega} + u_{\rm y}\right)\frac{\nu_{\rm zi}}{\Omega}\frac{1}{1+\nu_{\rm zi}^2/\Omega^2}, \tag{5.19a}$$

$$v_{\rm y} = v_\perp e^{-\nu_{\rm zi}t}\sin\Omega t - \frac{E_\perp}{B}\frac{1}{1+\nu_{\rm zi}^2/\Omega^2} + \left(u_{\rm x} + u_{\rm y}\frac{\nu_{\rm zi}}{\Omega}\right)\frac{\nu_{\rm zi}}{\Omega}\frac{1}{1+\nu_{\rm zi}^2/\Omega^2}. \tag{5.19b}$$

We see that the effect of adding the Langevin terms to the Lorentz force equation is to dampen the particle gyro motion and to cause ions to move with the background flow velocity $\mathbf{u}$. Moreover, we have, in addition to the (modified) $\mathbf{E}\times\mathbf{B}$ drift in the y-direction, an electric field dependent term in the x-component of the collisional particle equation of motion. In tokamaks plasmas we invariably have that $\nu_{\rm zi}^2 \ll \Omega^2$, that is the collision frequency is much smaller than the particle cyclotron frequency. In this limit, we are left with the usual $\mathbf{E}\times\mathbf{B}$ drift in the y-direction, found in the solution of the usual Lorentz force equation, and an additional "*drag force drift*" in the x-direction, which arises from the inclusion of a collisional drag in the test particle equation of motion. Substituting for the impurity-ion collision frequency, given by (2.88), we find that the drag force drift velocity can be written as

$$v_{\rm d} \simeq Z\frac{E_{\rm x}}{B^2}\frac{n_{\rm i}}{T_{\rm i}^{3/2}}\frac{m_{\rm i}^{1/2}e^3\ln\Lambda}{6\sqrt{2}\pi^{3/2}\epsilon_0^2}. \tag{5.20}$$

This is independent of test particle mass but proportional to test particle charge. Identifying the x-direction as a proxy for the radial direction in tokamak geometry the above equations imply an inward-pinch in the presence of a negative radial electric field. This has important implications for impurity particle transport in the vicinity of radial electric fields, as we presently investigate.

We note that the perpendicular flux, $nv_{\rm x}$, with n the particle number density and $v_{\rm x}$ derived above, is part of the classical particle flux [Braginskii, 1965; Helander and Sigmar, 2002], which for electrons has the form

$$n_{\rm e}\mathbf{v}_\perp = -\frac{1}{m_{\rm e}\Omega_{\rm e}^2\tau_{\rm ee}}\left(\nabla_\perp p_{\rm e} + n_{\rm e}e\mathbf{E}_\perp - \frac{3}{2}n_{\rm e}\nabla_\perp T_{\rm e}\right). \tag{5.21}$$

This contains contributions due to the electron pressure gradient, describing the expansion of the electron species in the direction $-\nabla p_{\rm e}$, the temperature gradient and the electric field. Whilst (5.21) is typically derived using a fluid model, we find that the electric field contribution is identical to the drag force drift velocity derived from the single particle Lorentz-Langevin equation above in the limit that $\nu_{\rm zi}^2 \ll \Omega^2$. The other contributions to the classical particle flux may also be derived from this test particle equation of motion by retaining the stochastic Langevin term, $\mathbf{a}_r$ in (5.13), and Taylor expanding this term about the guiding centre position.

In order to relate the impact of this collisional drag force drift on particle transport we consider the *stationary* one-dimensional transport equation

$$\frac{\mathrm{d}}{\mathrm{d}x}\left\{D\frac{\mathrm{d}n_{\rm z}}{\mathrm{d}x} + \frac{vn_{\rm z}}{1+(x/\Delta x)^2}\right\} = 0, \tag{5.22}$$

where v is the peak value of the drag drift, $v_{\rm d}$. Here we have assumed a form of the spatial variation of $E_{\rm x}$ that is consistent with the electrostatic potential given in (5.12), with x the displacement from the peak electric field ($x \equiv \bar{\Psi} - \bar{\Psi}_1$) and Δx a measure of the electric barrier width ($\Delta x \equiv \Delta\bar{\Psi}$). We neglect all spatial variations in $v_{\rm d}$ except for that occurring due to its dependence on $E_{\rm x}$. We also assume that the impurity ion Larmor radii are small compared to Δx and that particle drifts in the x-direction are due solely to the drag effect derived above. The above form of the transport equation ensures that the test particle flux, which we assume is composed of the usual diffusive and advective terms,

$$\Gamma_{\rm z} = -D\frac{\mathrm{d}n_{\rm z}}{\mathrm{d}x} - v_{\rm d}n_{\rm z}, \tag{5.23}$$

is constant. Introducing a dimensionless spatial variable $\xi = x/\Delta x$ and a Péclet number $\mathrm{Pe} = v\Delta x/D$, (5.22) becomes

$$\frac{\mathrm{d}n_{\rm z}}{\mathrm{d}\xi} + \frac{\mathrm{Pe}n_{\rm z}}{1+\xi^2} = -\gamma, \tag{5.24}$$

where $\gamma = \Gamma_{\rm z}\Delta x/D$. This has the exact solution

$$n_{\rm z}(\xi) = n_0 \exp\left(-\mathrm{Pe}\tan^{-1}\xi\right)\left[1 - \gamma\int_0^{\xi}\exp\left(\mathrm{Pe}\tan^{-1}\eta\right)\mathrm{d}\eta\right] \tag{5.25}$$

where n_0 is the particle density at $x = 0$, the position of peak electric field and drag

force drift. For $\xi \ll 1$, or $x \ll \Delta x$, this reduces to

$$n_{\rm z}(x) = n_0 \exp\left(-\frac{{\rm Pe}x}{\Delta x}\right) - \frac{\Gamma_{\rm z}}{v}\left[1 - \exp\left(-\frac{{\rm Pe}x}{\Delta x}\right)\right]. \tag{5.26}$$

It follows that, at $x = 0$, we have

$$D_{\rm eff} \equiv -\frac{\Gamma_{\rm z}}{dn_{\rm z}/dx} = \frac{D}{1 + vn_0/\Gamma_{\rm z}}. \tag{5.27}$$

Identifying v with the drag force drift velocity and noting that $n_{\rm z}/\Gamma_{\rm z}$ is essentially constant between CUEBIT simulations we therefore find that the local effective particle diffusion coefficient scales with test particle charge as

$$D_{\rm eff} = \frac{D}{1 + \alpha Z}, \tag{5.28}$$

where

$$\alpha = \frac{E_{\rm x}}{B^2}\frac{n_0 n_{\rm i}}{T_{\rm i}^{3/2}}\frac{m_{\rm i}^{1/2} e^3 \ln\Lambda}{6\sqrt{2}\pi^{3/2}\epsilon_0^2 \Gamma_{\rm z}}, \tag{5.29}$$

and is independent of both the test particle mass and charge. Despite the approximations used to derive (5.28), we will show in the next section that it provides a fairly accurate description of impurity ion transport at an ETB in full toroidal geometry.

5.4.3 Diffusion coefficient scaling with particle parameters

We now present CUEBIT simulation results for a number of impurity species in order to determine, from first principles, the scaling of the effect of the radial electric field with particle parameters and to verify the scaling suggested in the previous section.

A number of impurity ion species were simulated, both with and without the inclusion of a radial electric field, for a fixed plasma equilibrium and fixed bulk ion density and temperature profiles. In table 5.1 we list the normalised collision frequency for each of the impurity species simulated. We also list the diffusion coefficients calculated for each species both with and without the inclusion of an inward directed, sheared radial electric field.

In the absence of an electric field we expect collisional particle transport to be purely diffusive [Helander and Sigmar, 2002]. For tokamak plasmas with slowly-varying profiles, transport coefficients may be deduced empirically from moments of the spatial distribution of test particles [Wong and Cheng, 1989; McClements and McKay, 2009] (see section 4.2.1). However, in the case of narrow transport barriers,

Impurity species	ν^*	D_0	D_{eff}
Ne^{2+}	0.017	0.271	0.033
Ne^{3+}	0.038	0.306	0.029
Ne^{4+}	0.067	0.295	0.028
Ne^{5+}	0.105	0.277	0.024
Ne^{6+}	0.152	0.261	0.022
Ne^{7+}	0.206	0.238	0.020
Ne^{8+}	0.270	0.228	0.017
Ne^{9+}	0.341	0.213	0.017
Ne^{10+}	0.421	0.205	0.015
Si^{10+}	0.356	0.210	0.016
Ar^{10+}	0.298	0.217	0.016
Mo^{10+}	0.196	0.224	0.019
W^{10+}	0.139	0.213	0.019

Table 5.1: Normalised collision frequency for impurity ions simulated with computed effective diffusion coefficients, (5.30), without, D_0, and with, D_{eff}, a sheared radial electric field as given by (5.12). For both D_0 and D_{eff} the associated error is of the order of 5×10^{-3}.

with plasma properties varying on length scales down to the Larmor radius, it is not possible to infer local transport coefficients using this method. In such cases a local effective diffusivity D_{eff} may be deduced directly from the local radial particle flux, Γ_Z, and density gradient, $\partial n_Z/\partial\rho$ as

$$D_{\text{eff}} = -\frac{\Gamma_Z}{\partial n_Z/\partial\rho}, \tag{5.30}$$

with the particle flux calculated as the time derivative of the particle fluence (see section 4.2.2). Here n_Z is the flux surface-averaged minority ion density and $\rho = \rho(\Psi)$ is the flux surface minor radius, defined as

$$\rho(\Psi) = \frac{R_+ - R_-}{2}, \tag{5.31}$$

with R_- and R_+ the minimum and maximum major radial extents of the flux surface Ψ along the mid plane [for the case of an analytic Solov'ev equilibrium, this is given by (2.26)]. To quantify the impact of sheared electric fields on particle transport the value of D_{eff} is normalised to the value of the diffusion coefficient measured in the absence of any electric field, D_0.

Clearly D_{eff} is a simplified formulation of the particle diffusion coefficient since we assume that particle flux scales linearly with the minority ion density gradient. However, the impurity ion flux Γ_Z, which appears in (5.30), is the full particle

flux as computed by CUEBIT. This includes the effects of transport driven by bulk ion gradients, including the thermal force arising from the bulk ion temperature gradient (see, for example, Helander and Sigmar [2002, equation 5.9]). Such a force arises from the variation of the collision frequency across a Larmor orbit and, unlike guiding centre and fluid calculations, this force appears naturally in full orbit particle simulations. The subscript *eff* is intended to emphasise this point.

In the absence of an electric field both the mean square displacement and the particle fluence measurements can be used to calculate particle diffusion coefficients. This allows one to verify one measurement against the other. With the inclusion of the electric field only the particle fluence measurement, discussed above, is available.

In simulating the impurity species listed in table 5.1 test particles were initialised uniformly in configuration space, with initial normalised poloidal flux values between 0.3 and 0.5. Particles which left this region were reintroduced on the same flux surface but with the sign of their poloidal angle changed. Unlike the preliminary simulations of the previous section, in which all particles were released from the magnetic axis, the current scheme is more computationally efficient, since particles begin interacting with the electric field immediately. Each simulation is run until the particle flux and density gradient at the peak of the electric field have each reached a stationary value, except for noise fluctuations arising from the use of a finite number of test particles. Whilst this is not a global steady-state solution since the core impurity density will be continually depleted in the absence of a particle source, locally to the radial electric field a stationary equilibrium is achieved, consistent with the assumption of zero divergence of the particle flux used from (5.22) onwards, since transport due to the radial electric field occurs on a shorter timescale than the losses due to collisional transport (as shall be demonstrated in the following chapter).

In figure 5.6a the normalised diffusion coefficient is plotted for particle mass numbers in the range 20 (neon) to 184 (tungsten) all with Z=10. We see that the diffusion coefficient is essentially independent of mass number. In figure 5.6b the test particle mass number is held fixed at 20 but the charge state is varied from Z=2 to Z=10. Equation (5.28) predicts that the quantity $D/D_{\text{eff}} - 1$ varies linearly with particle charge number, which we see is in good agreement with the results shown in figure 5.6b.

The results presented in table 5.1 and figure 5.6 demonstrate that, despite its relative simplicity, the analytical model presented in the previous section appears to capture the key effects and scaling of a MAST ETB-like, inward directed radial electric field on collisional impurity transport and is in good agreement with the

results of the first principles, global collisional transport results of the CUEBIT code.

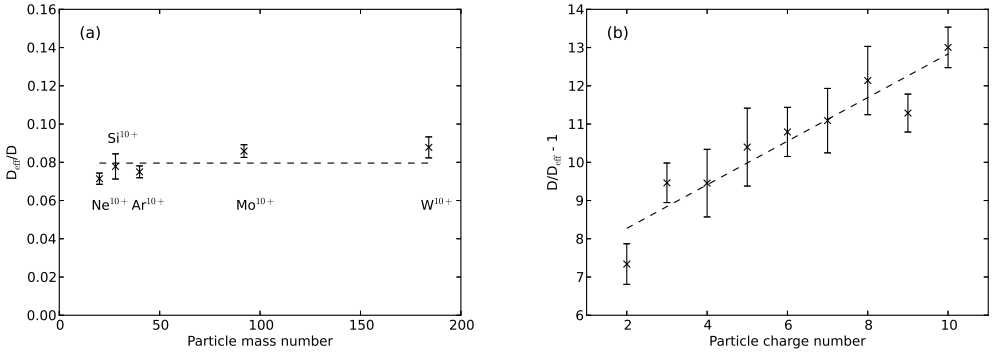

Figure 5.6: Scaling of particle diffusion coefficient with particle parameters: (a) scaling with test particle mass with constant charge number Z=10; (b) scaling with test particle charge for constant mass number of 20 (neon).

5.4.4 Diffusion coefficient scaling with electric field strength and width

We also investigate the scaling of the change in particle transport with the model parameters of the electric field, that is the electric field width and strength. For the following discussion 10^4 C^{6+}, Ne^{10+}, Ar^{15+} and Mo^{20+} were simulated for radial electric field profiles with parameter in the ranges $0.5\rho_{\mathrm{Li}} \leqslant \Delta R \leqslant 4\rho_{\mathrm{Li}}$ and $-0.65\ \mathrm{kVm}^{-1} \leqslant E \leqslant -7.65\ \mathrm{kVm}^{-1}$ for all impurity species, with ρ_{Li} the bulk ion Larmor radius. Figure 5.7 shows the variation with electric field width and height of the effective diffusion coefficient for C^{6+} ions. We see that the particle diffusion coefficient is most strongly reduced for the largest and widest electric field structures simulated.

Plotting the C^{6+} normalised effective diffusivity against electric field width for constant electric field heights, we find a a power law scaling between effective diffusivity and electric barrier width. The coefficients of this fit themselves scale linearly with barrier height. Thus the scaling of diffusion coefficient with electric field width and strength may be expressed in the form

$$D_{\mathrm{eff}} = D_0 \left[\frac{\Delta R}{\Delta R_0} \right]^{E/E_0} \ \mathrm{m}^2\mathrm{s}^{-1}, \tag{5.32}$$

where ΔR is the full width at half maximum (FWHM) of the electric field in the

outer mid-plane and E is the peak height of the radial electric field barrier. We see that the diffusion coefficient scales as the width of the electric field barrier to a power of the electric field strength, with the width of the barrier normalised to a fraction of the bulk ion Larmor radius. In the limit of no electric field this scaling recovers the effective diffusivity as found in simulations without an electric field barrier. The scaling parameters for various species are listed in table 5.2.

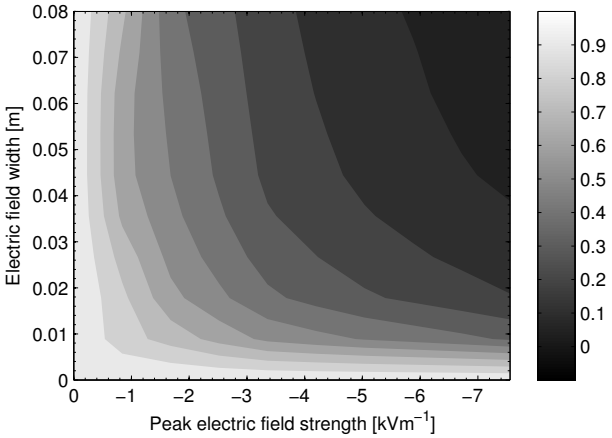

Figure 5.7: Contours of constant normalised effective diffusion coefficient for C^{6+} ions against radial electric field height and width.

Unlike (5.28) the empirical expression for D_{eff} given by (5.32) does in fact depend on the barrier width, implying limits in the validity of the approximations used to derive the former. We expect that for large $\Delta R/\rho_{\text{Li}}$, the effective diffusion coefficient will no longer have a power law scaling but will tend asymptotically to a result similar to (5.28).

We note from table 5.2 that ZE_0 and ΔR_0 are broadly constant. Therefore, the dependency of impurity transport on the shape of the electric field barrier depends approximately only on the charge state of the species, not on the species mass. Thus, we can approximate this scaling as

$$D_{\text{eff}} \simeq D_0 \left(\frac{\Delta R}{0.2\rho_{\text{Li}}} \right)^{ZE/57} . \tag{5.33}$$

Equation (5.33) provides a simple empirical formula which may be used as a rule of thumb to estimate the likely reduction of transport of test impurity ions with the introduction of a radial electric field.

Impurity species	D_0 ($\mathrm{m^2 s^{-1}}$)	ΔR_0	E_0 ($\mathrm{kV m^{-1}}$)
C^{6+}	8.3 ± 0.4	$(0.17 \pm 0.02)\,\rho_{\mathrm{Li}}$	8.1 ± 0.4
Ne^{10+}	3.4 ± 0.4	$(0.21 \pm 0.03)\,\rho_{\mathrm{Li}}$	5.7 ± 0.4
Ar^{15+}	2.0 ± 0.6	$(0.20 \pm 0.02)\,\rho_{\mathrm{Li}}$	4.2 ± 0.4
Mo^{20+}	1.6 ± 0.8	$(0.22 \pm 0.03)\,\rho_{\mathrm{Li}}$	2.9 ± 0.6

Table 5.2: Scaling of computed effective diffusion coefficient, (5.30), with electric field strength, E, and width, ΔR, for several impurity species.

5.5 Discussion

In this chapter we have simulated realistic radial electric field profiles in a spherical tokamak equilibrium and investigated the impact on collisional impurity transport of the strength and width of the electric field profile for a variety of impurity species. It has been shown that a strongly-sheared radial electric field can significantly increase the confinement of test particle ions. This effect has been explained in terms of a drift arising from the drag between impurity and bulk ions, with the direction of the drift given by the radial electric field and its strength determined by the impurity charge.

Clearly, the negative implication of this work is the enhanced confinement of highly ionized impurity species in the vicinity of strong, negative radial electric fields, such as those in the edge of MAST plasmas. This is in addition to the neoclassical impurity accumulation [Helander and Sigmar, 2002], which is driven by gradients in the bulk ion temperature and density. In high performance tokamak discharges, with both strong edge radial electric fields and a steep pedestal in the bulk ion density, we would expect that, in the absence of anomalous transport, both neoclassical effects and the drag force drift will lead to the accumulation of impurity ions in the plasma core.

Whilst the effect of bulk plasma rotation was neglected in the present study, one would expect the edge radial electric field to be associated with flows of the bulk ions in H-mode plasmas, as discussed at the start of this chapter. For impurity ions in particular inertial effects will become important in rotating plasmas. As shown by McClements and McKay [2009], strong toroidal rotation can cause heavy, incompletely-ionised impurities such as W^{20+} to undergo rapid collisional transport, due to the combined effect of trapping in a centrifugal potential well and a modification to the effective magnetic field arising from the Coriolis force. One would therefore expect a competition between this enhanced transport due to rotation and the improved confinement resulting from sheared radial electric fields.

We note that the effect of improved confinement due to a sheared radial

electric field is more important for spherical tokamak plasmas than for conventional tokamaks, primarily due to the strong B dependence in (5.20). For example, in the MAST-like equilibrium used throughout, we have that the Ware pinch velocity is of the order $v_{\mathrm{Ware}} \simeq qE_\phi/\epsilon B \sim 5.6$ ms^{-1} and the drag force drift velocity is of the order $v_{\mathrm{d}} \sim 8.2$ ms^{-1} for C^{6+} (where we have used $B = 0.4$ T, $E_x = -10$ kVm^{-1}, $E_\phi = -0.3$ Vm^{-1}, $n_i = 3 \times 10^{19}$ m^{-3}, $T_i = 500$ eV, $q = 3$ and $\epsilon = 0.4$). Typical values for a large conventional tokamak such as JET, on the other hand, are $v_{\mathrm{Ware}} \sim 0.4$ ms^{-1} and $v_{\mathrm{d}} \sim 0.02$ ms^{-1} (assuming $B = 3$ T, $E_x = -20$ kVm^{-1}, $E_\phi = -0.04$ Vm^{-1}, $n_i = 3 \times 10^{19}$ m^{-3}, $T_i = 5$ keV, $q = 3$ and $\epsilon = 0.1$ [Tala et al., 2007]). Thus, the drag force drift is therefore less significant than the Ware pinch under typical conventional tokamak conditions.

Finally, we note that in our derivation of the drag force drift given by (5.20) we neglected both spatial variations in the radial electric field and toroidal geometry. However, the scaling of effective diffusivity with Z inferred from using this drift velocity in a simple slab model of the transport barrier, (5.28), is in agreement with our test-particle simulations in which no approximations are made with regard to finite Larmor radius or toroidal effects. This suggests that test-particle transport in the immediate vicinity of the barrier is not strongly-dependent on the effects of toroidal geometry or the collisionality regime (in other words the value of ν^*). This further indicates that finite Larmor radius effects are relatively unimportant. One would expect electric field shear on length scales approaching the particle Larmor radius to result in a modified drag force drift velocity, analogous to the $\mathbf{E} \times \mathbf{B}$ drift with finite Larmor radius correction discussed by Tao et al. [1993]. However, this requires further study.

Chapter 6

Test particle simulations of the role of time varying radial electric fields on collisional transport

In the previous chapter the effects of a stationary radial electric field on the collisional transport of impurity ions is investigated. However, in simulations of realistic tokamak plasmas one should include the fluctuations of the radial electric field arising from a number of processes, including instabilities in the plasma and turbulent processes. For example, the radial electric field has been observed to fluctuate due to geodesic acoustic mode (GAM) oscillations [Krämer-Flecken et al., 2009; Temple et al., 2009]. These are sound waves which arise from toroidal coupling between *zonal* ($m = n = 0$) potential fluctuations and $m = 1$, $n = 0$ density fluctuations, with m and n the toroidal and poloidal mode numbers of the fluctuations. Furthermore, in fluid simulations of the COMPASS-D tokamak it has been observed that the H-mode radial electric field close to the plasma edge changes from being negative between edge localised modes (ELMs), ballooning-like MHD instabilities driven by steep pressure gradients in the plasma edge, to positive during an ELM [Thyagaraja et al., 2010]. Typically ELMs are associated with H-mode plasmas and an ELMy H-mode is likely to be the baseline operating regime for ITER [Shimada et al., 2007]. In the context of the results of the previous chapter one would expect the direction of the drag force drift to switch between inward and outward directed, which could have important implications for impurity accumulation and the transport of particles at transport barriers.

Moreover, whilst the structure of the radial electric field, E_r, is likely to be important in determining the rate of $\mathbf{E} \times \mathbf{B}$ shear flow suppression of turbulent transport and in the formation of transport barriers, it is thought that it is fluctuations of the radial electric field, $\tilde{E}_r$, rather than the mean field which is important for the transition from low- to high-confinement modes of operation [Estrada et al., 2009; Meyer et al., 2011].

The flexibility of the full orbit approach means that oscillatory or even turbulent electric (and magnetic) fields can be readily incorporated into numerical studies of impurity transport. In the present chapter we therefore investigate the transport of impurity ions in the presence of a time varying edge electric field. First, we investigate the impact of an oscillatory electric field, maintaining the same functional form of the radial electric field as used in the previous chapter, intended to model a generic rapid collapse and reformation of the edge radial electric field. These preliminary simulations inform subsequent simulations of two specific scenarios, that of an ELM event and the L-H transition. In both of these scenarios the time variation of the edge radial electric field is matched to the observed behaviour of this field in the edge of the MAST plasma for these two distinct scenarios. We then close this chapter with a brief comparison to experimental observations of impurity density profiles on MAST.

6.1 Preliminary simulations

In order to gain insight into the effect of time variations of the edge radial electric field we modulate the radial electric field of the previous chapter with a simple periodic time dependence and compare the results of these simulations to simulations with no electric field and with the stationary electric field of this previous chapter. In figure 6.1 the flux surface averaged density profiles of C^{6+} ions as a function of time and normalised minor radius is presented for these cases. In all cases approximately 10^4 test ions are initialised uniformly across the plasma minor radius and a flat bulk ion number density profile to avoid neoclassical impurity accumulation. In each of these simulations, and in the remainder of the simulations presented in this chapter, the bulk ion density is held fixed at 1.25×10^{19} m^{-3} and the bulk ion temperature at the magnetic axis and at the plasma edge are 240 eV and 140 eV respectively.

In the case of no radial electric field, figure 6.1a, the test particle density remains broadly flat for the entire simulation. This is in contrast to the case of the static electric field of the previous chapter, figure 6.1b. In this case we find that there is an inward convection of test ions in the vicinity of the radial electric field,

with a minimum in the test ion density at the location of the peak radial electric field.

Introducing a time dependence of the radial electric field of the form

$$\mathbf{E}_{\mathrm{r}}(R,Z,t) = \mathbf{E}_{\mathrm{r}}(R,Z)\sin^2(\pi\Omega_{\mathrm{E}}t). \tag{6.1}$$

With $\Omega_{\mathrm{E}} = 2000\ \mathrm{s}^{-1}$ (corresponding to a period of variation of approximately 0.3 ms), figure 6.1c, we see that the confinement of the test ions is significantly weakened by the introduction of a time variation of the electric field. One would expect that this case broadly corresponds to the case of a stationary radial electric field whose magnitude is equal to the averaged magnitude of this time varying field, although this has not been verified.

Finally we simulate the case of a time variation of the form

$$\mathbf{E}_{\mathrm{r}}(R,Z,t) = \mathbf{E}_{\mathrm{r}}(R,Z)\left[\frac{3}{4}\cos(2\pi\Omega_{\mathrm{E}}t) + \frac{1}{4}\right]. \tag{6.2}$$

This is so that the magnitude of the electric field oscillates between it's peak negative value and a smaller positive value. Thus, we would expect that the drag force drift force of the previous section will oscillate from being inward to outward directed during each period of the electric field oscillation. In this final case the peak of the radial electric field was moved out to the plasma edge to more closely approximate the radial electric field of MAST. We find in this case that the density profile of the test ions is largely indistinguishable from the case of no electric field.

6.2 Oscillatory radial electric fields: simulating edge localised modes

The steep edge temperature and density gradients in H-mode plasmas lead to a specific MHD instability, the so-called edge localized mode (ELM), a ballooning-like mode which expels energy and particles from the plasma edge [Zohm, 1996; Loarte et al., 2003; Huysmans and Czarny, 2007]. The ELMy H-mode is an operating regime obtained in many diverted tokamak plasmas which has has acceptable energy confinement at the high densities required in future tokamak devices. In many experiments, it has been found that stationary H-mode discharges could only be obtained in ELMy H-mode [Zohm, 1996]. However, a significant drawback of this operating regime is the large periodic power loads on plasma facing components associated with the ELMs [Loarte et al., 2003]; these cause fast losses of energy (in

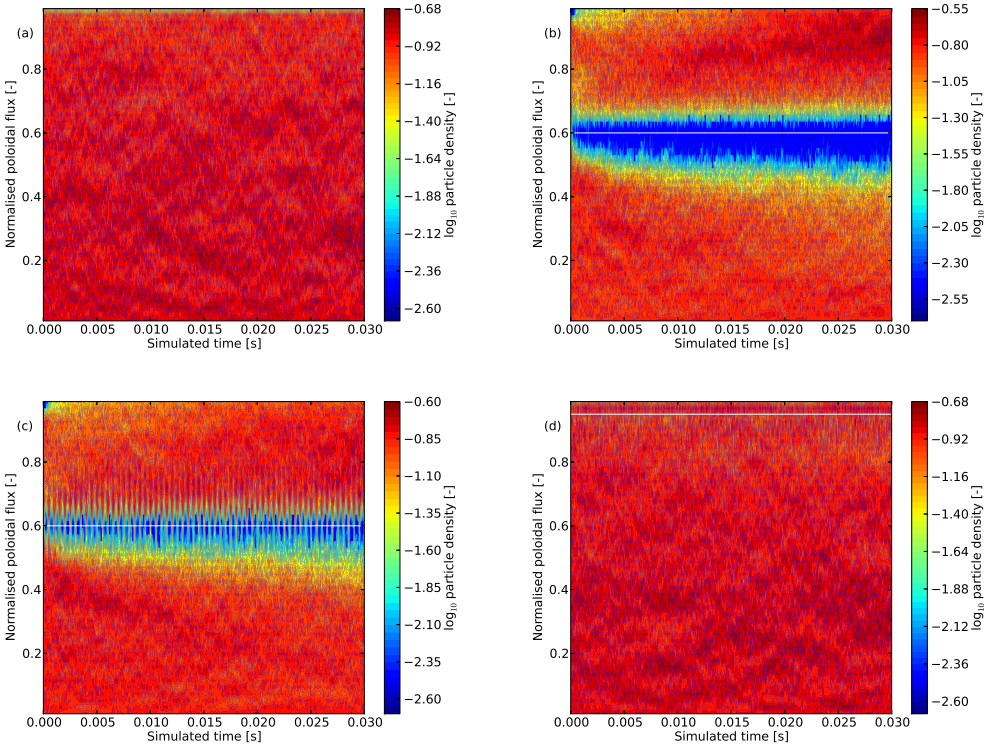

Figure 6.1: Simulated C^{6+} test ion density profiles against normalised minor radius and simulation time, both with and without a radial electric field included in the CUEBIT simulations: (a) no radial electric field; (b) stationary radial electric field with prescribed electrostatic potential of the form (5.12); (c) time varying radial electric field of the form (6.1); and (d) time varying electric field of the form (6.2).

several hundred microseconds) from the confined plasma that amount, typically, to a few per cent of the total plasma energy [Zohm, 1996]. Extrapolating the size of the ELMs towards ITER based on existing experiments leads to an excessive predicted ELM size [Huysmans and Czarny, 2007], in the sense that the energy flux directed towards the first wall and divertor could damage these plasma facing components.

Measurements of the edge radial electric field, E_r, in MAST H-mode plasmas through an ELM event [Meyer et al., 2011] demonstrate the collapse of the radial electric field during the ELM, see figure 6.2. From this figure it can be seen that the ELM destroys the shear layer in E_r during its rise time before E_r recovers more slowly.

In order to simulate the effect of such a collapse of the radial electric field on the transport of test particle ions we introduce a time variation of the electric field chosen to model this asymmetric fall and rise of this field. From Meyer et al. [2011]

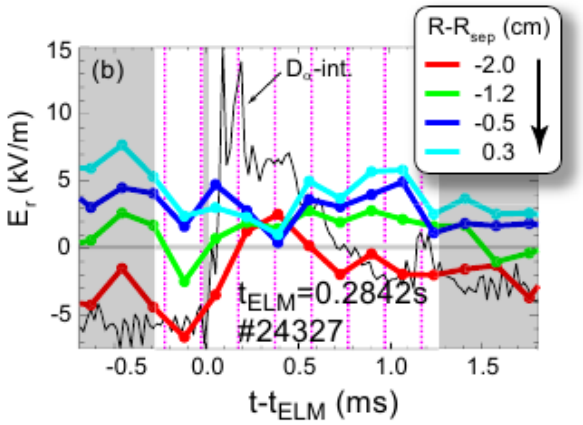

Figure 6.2: Evolution of the edge radial electric field in MAST during an edge localised mode [Meyer et al., 2011].

the spatial variation of the electric field remains well approximated by the form used in the previous chapter, (5.12). From the preliminary simulations presented in the previous section we may expect that a collapse in the radial electric field would lead to an outward flux of particles, similar to a single period of the oscillation of figure 6.1c.

Motivated by this case we model the response of the particle distribution to a time varying electric field using the equation

$$\frac{\mathrm{d}f}{\mathrm{d}t} + \frac{f - f_0}{\tau} = F(t). \tag{6.3}$$

Here $F(t)$ is a term describing the time variation of the electric field and the time constant τ characterises the time response of the particle distribution to a constant electric field. In the absence of a time variation, with $F(t) = 0$, we find that (6.3) has the solution $f = f_0 + k \exp(-t/\tau)$ with k a constant. Thus, the as yet unspecified quantity f tends to a value f_0 with a characteristic time scale τ. In the following we use the particle fluence (section 4.2.2) to characterise the effect of a time variation of the radial electric field on test particle transport and as the dependent variable in (6.3). Alternatively, we may use the flux surface averaged density, as plotted in figure 6.1.

Equation (6.3) may easily be solved using the same technique as used to solve the Langevin equation, section 5.4.2. Writing

$$\exp\left(-\frac{t}{\tau}\right)\frac{\mathrm{d}}{\mathrm{d}t}\left[\exp\left(\frac{t}{\tau}\right)(f - f_0)\right] = F(t) \tag{6.4}$$

we find that

$$f = f_0 + \exp\left(-\frac{t}{\tau}\right)\int_0^t \exp\left(\frac{t'}{\tau}\right)F(t')dt'. \tag{6.5}$$

A first attempt at modelling an ELM-like perturbation to the radial electric field was simulated by prescribing a log-normal variation in time to the electric field. However, there are no closed form solutions to the above equation when $F(t)$ is a log-normal distribution. A similar functional form to the log-normal distribution may be constructed from the product of the normal, or Gaussian, distribution with a linear function of the independent variable. We therefore choose to model $F(t)$ as

$$F(t;\mu,\sigma) = \frac{(t-\mu)}{\sigma\sqrt{2\pi}}\exp -\frac{1}{2}\frac{(t-\mu)^2}{\sigma^2}. \tag{6.6}$$

Here we note that $F(t)$ is simply related to the derivative of the Gaussian function. Denoting the normal distribution by $\mathcal{N}$,

$$\mathcal{N}(t;\mu,\sigma) = \frac{1}{\sigma\sqrt{2\pi}}\exp -\frac{1}{2}\frac{(t-\mu)^2}{\sigma^2}, \tag{6.7}$$

we have that

$$F(t;\mu,\sigma) = -\sigma^2\frac{\mathrm{d}\mathcal{N}}{\mathrm{d}t}. \tag{6.8}$$

The functional form of this expression is illustrated in figure 6.3. Here this choice of the form of $F(t)$ can be justified by comparing to figure 6.2: the form of (6.8) for $t > 0$ is an idealisation of the time evolution of the edge radial electric field at $R - R_{\mathrm{sep}} = -2.0$ cm of figure 6.2.

The turning points of this function defined in (6.8) occur at $t = \mu \pm \sigma$. Normalising this function to equal ± 1 at these points and redefining F such that $F = 0$ for $t \leqslant \mu$ we finally arrive at an equation for the time variation of the radial electric field

$$F(t;\mu,\sigma) = \begin{cases} \frac{(t-\mu)}{\sigma}\exp\left[\frac{1}{2} - \frac{1}{2}\frac{(t-\mu)^2}{\sigma^2}\right] & t > \mu \\ 0 & t \leqslant \mu. \end{cases} \tag{6.9}$$

Now μ determines the start time of the rise of the function and $\mu + \sigma$ defines the location of the peak of this function, $F(t = \mu + \sigma) = 1$.

With the functional form of F derived above, (6.9), we have an analytical

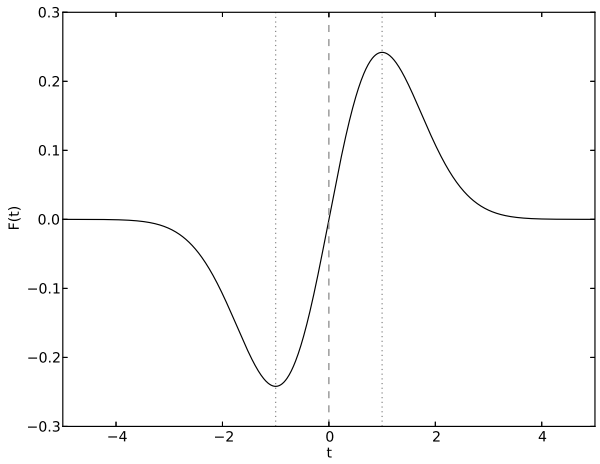

Figure 6.3: Functional form of the prescribed time variation to the edge radial electric field, (6.8), with $\mu = 0$ and $\sigma = 1$.

solution to (6.3). First we evaluate

$$\begin{aligned}\int_0^t \exp\left(\frac{t'}{\tau}\right) F(t')dt' =& -\sigma^2\sqrt{2\pi}e^{1/2}\int_0^t \exp\left(\frac{t'}{\tau}\right)\frac{\mathrm{d}\mathcal{N}}{\mathrm{d}t}dt' \\ =& -\sigma^2\sqrt{2\pi}e^{1/2}\left\{\left[\exp\frac{t'}{\tau}\mathcal{N}(t')\right]_0^t\right. \\ & \left.-\frac{1}{2\tau}\exp\left(\frac{\mu\tau+0.5\sigma^2}{\tau^2}\right)\left[\mathrm{erf}\left(\frac{t'-\sigma^2/\tau-\mu}{\sqrt{2}\sigma}\right)\right]_0^t\right\}. \quad (6.10)\end{aligned}$$

Here erf is the error function, that is the integral of the Gaussian function. The solution to (6.3) is therefore found to be

$$\begin{aligned}f(t) =& f_0 - \sigma\exp\left[\frac{1}{2}-\frac{1}{2}\frac{(t-\mu)^2}{\sigma^2}\right] - \sigma\exp\left(\frac{1}{2}-\frac{t}{\tau}-\frac{\mu^2}{2\sigma^2}\right) \\ & -\sqrt{\frac{\pi}{2}}\frac{\sigma^2}{\tau}\exp\left(\frac{1}{2}+\frac{\mu\tau+0.5\sigma^2}{\tau^2}\right)\left[\mathrm{erf}\left(\frac{t-\sigma^2/\tau-\mu}{\sqrt{2}\sigma}\right)-\mathrm{erf}\left(\frac{-\sigma^2/\tau-\mu}{\sqrt{2}\sigma}\right)\right]. \quad (6.11)\end{aligned}$$

We therefore postulate that the response of the particle fluence to a time variation of the radial electric field may be modelled by this above expression.

We first determine the value of the time constant τ. This is achieved by running a simulation with a step function time variation of the electric field. That is, the electric field, initially zero, is increased to it's maximum value in a single

time step. The introduction of the radial electric field causes an inward flux of test ions due to the drag force drift. Fitting to the increase in magnitude of the particle fluence following the introduction of the electric field we find that τ, for the case of C^{6+} ions and the electric field profile of the previous chapter, has a value of 2000 s. Clearly one would expect the value of this constant to change with test ion species and, possibly, with changing characteristics of the electric field structure, such as the extent and magnitude of the electric field. One would need to recalculate this quantity for each new scenario simulated.

We now introduce a time variation of the radial electric field of the form

$$\mathbf{E}_{\mathrm{r}}(R, Z, t) = [1 - F(t)]\, \mathbf{E}_{\mathrm{r}}(R, Z), \tag{6.12}$$

with $F(t)$ given by (6.9). Here μ and σ are chosen to be 5 ms and 1 ms respectively in order to approximate the time variation of figure 6.2. This start time of the 'ELM' is chosen such that the response of the particle density profile to the collapse of the radial electric field is well separated from the initial inward pinch due to the electric field.

The time evolution of the flux surface averaged test particle density and the time evolution of the particle fluence at the flux surface of the peak in the spatial variation of the electric field (indicated by the solid horizontal line) are presented in figure 6.4 for an ensemble of approximately 3×10^4 C^{6+} ions. We see from the particle density profile that test ions diffuse outwards with the fall of the radial electric (indicated by the leftmost vertical dashed line) field in order to fill the void left by the initial inward convention due to the drag force drift. This corresponds to an increase in the particle fluence (and a corresponding increase in the outward particle flux). As the radial electric field begins to rise (after reaching it's minimum value at the rightmost vertical dashed line) the inward pinch again starts to become increasingly important and the time derivative of the particle fluence, the particle flux, changes sign. Overlaid on the plot of particle fluence is a fit to the fluence of the form of (6.11). We find that the above derivation is able to approximate the response of the test particle distribution to a time varying electric field.

One advantage of the procedure described above is that multiple 'ELM' events may easily be simulated by imposing multiple independent time variations of the radial electric field. The solution (6.11) is easily generalised to describe the response to a time varying electric field, $F(t)$, which is a sum of functions of the form (6.9).

Throughout the above discussion we have modelled only the effect of a time

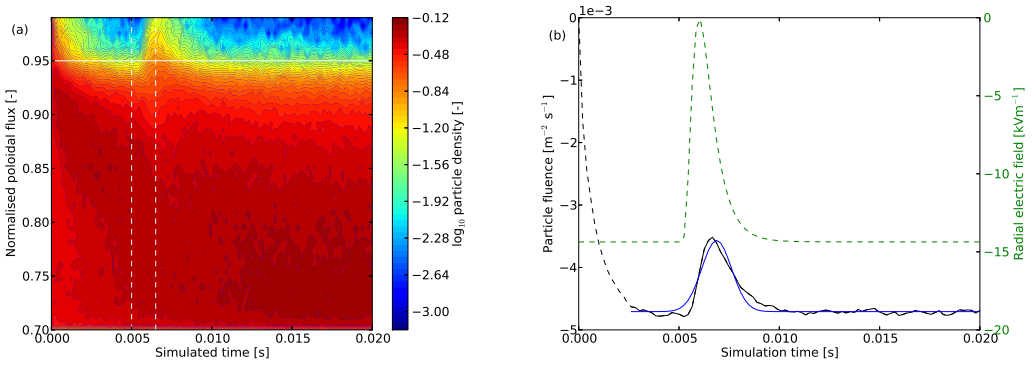

Figure 6.4: The response of a distribution of C^{6+} ions to a time varying electric field of the form (6.12). Shown is the time variation of the flux surface averaged particle density as a function of time (a) and the particle fluence at the location of the peak electric field (b). The time variation of the electric field begins at 5 ms [leftmost dashed vertical line in (a)] and the electric field reaches it's minimum value at 6 ms [rightmost dashed vertical line in (a)]. The location of the peak electric field is indicated by the solid horizontal line in (a). Superimposed on (b) is the time evolution of the maximum value of the peak radial electric field (green dashed line).

varying radial electric field on the transport of test particles, with the time variation chosen to model the observed variation due to an ELM. However, transport in the plasma edge is dominated by intermittent three dimensional helical filaments, coherent structures which are localized perpendicular to the magnetic field, but extend much longer distances along it [Ben Ayed et al., 2009]. These coherent structures require a self-consistent simulation and have not been modelled here. However, one could in principle incorporate CUEBIT into a non-linear MHD simulation in order to determine effect of filaments on the transport of test impurity ions. This is a potential area for future work.

6.3 Simulating the L-H transition: a comparison with experiment

The second case we consider is a model of the transition from low- to high-confinement modes. Meyer et al. [2011] demonstrate that a sheared edge radial electric field develops through the L-H transition, see figures 5.1 and 6.5. After 1.5 ms from the onset of the L-H transition a well in the electric field develops which is broadly the same as the initial electric field in figure 6.2.

We again simulate approximately 3×10^4 C^{6+} ions, uniformly distributed in

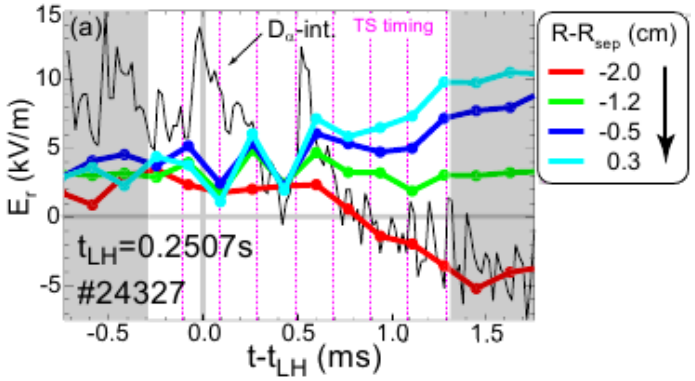

Figure 6.5: Evolution of the edge radial electric field during an L-H transition in MAST [Meyer et al., 2011].

configuration space. The radial electric field strength is increased linearly over a period of 1.5 ms to a peak value of approximately -5.5 kVm^{-1}. By observing the time variation of test ion density profile (figure 6.6), we find that the inward pinch of these ions increases with the radial electric field strength, reducing the density of the impurity species in the vicinity of the peak of the radial electric field.

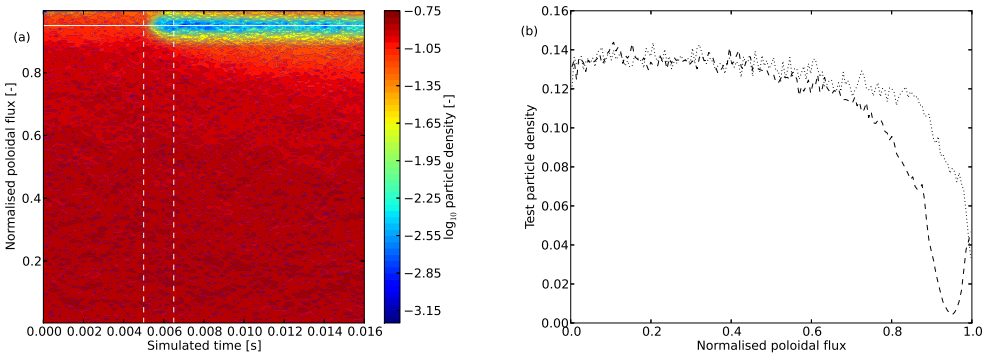

Figure 6.6: (a) Variation of test C^{6+} ion density with normalised minor radius and simulation time due to a radial electric field whose strength is linearly increasing in time. The radial electric field initially increases from zero at 5 ms [leftmost dashed vertical line in (a)] to a peak value of -5.5 kVm^{-1} at 6 ms [rightmost dashed vertical line in (b)]. The location of the peak electric field is indicated by the solid horizontal line in (a). (b) initial (dotted line) and final (dashed line) test ion density profiles.

One motivation for studying this particular case is that recent MAST experiments have yielded data for the density profiles of injected carbon and helium in both L-mode and H-mode plasmas. Thus we may attempt to make at least qualitative comparisons with experiment. First, the time evolution of the density profile

of carbon through an L-H transition is presented in figure 6.7. We see that in the vicinity of the edge radial electric field (at a major radius of approximately 1.25 m in figure 6.7) a minimum in the particle density forms as the edge electric field develops. This is similar to figure 6.6b where the minimum in test particle density coincides with the peak of the radial electric field.

There are however a number of differences between the two plots. The experimental density profile is initially strongly peaked and flattens in the core as the plasma enters H-mode, whereas the simulation of figure 6.6 is initialised with a flat impurity ion density profile. We are, however, interested only in the behaviour of the test particle ions in the vicinity of the edge radial electric field. The pump out of impurity ions in the plasma core in the experimental data is likely to be linked to anomalous transport of the impurity ions, which we make no attempt to simulate. Furthermore, there is a strong peak in the impurity ion density between a major radius of 1.3 and 1.4 m in figure 6.7 which is not captured in figure 6.6. This peak is likely to be due to an influx of carbon from the plasma facing components of MAST due to MHD activity which we again make no attempt to simulate.

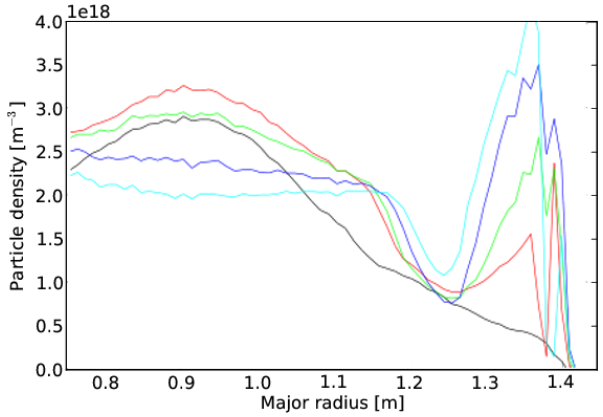

Figure 6.7: Time evolution of the density of Carbon in MAST during an L-H transition [McCone, 2011]. The density profiles are measured in L-mode at 275 ms (black line) and in H-mode at 285, 290, 300 and 310 ms (red, green, dark blue and blue lines respectively).

More detailed experimental data with improved time resolution of the evolution impurity density profiles has recently been obtained by Henderson [2012] for both injected carbon and helium. This work also attempts to determine the diffusion coefficient and convective velocity of these species, both in L-mode and H-mode plasmas. Figure 6.8 shows the computed diffusion coefficient and convective velocity for carbon in a H-mode MAST plasma. There is a large, inward convective velocity

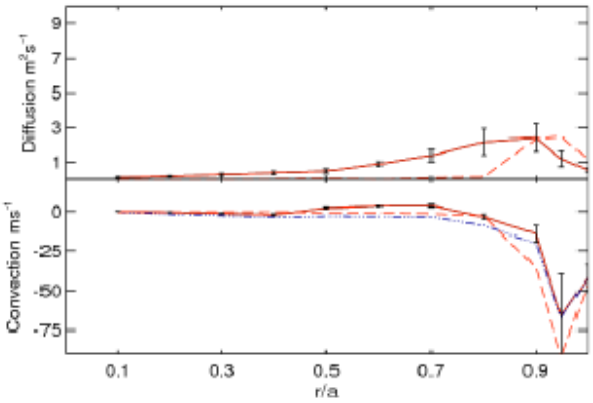

Figure 6.8: Computed diffusion coefficient (upper) and convection velocity (lower) computed using the SANCO code [Giroud et al., 2007] for a H-mode MAST plasma. The solid and dashed lines represent the different models used to match these coefficients to experimental observations [Henderson, 2012].

at the plasma edge in the vicinity of the peak of the edge radial electric field (this is also the case for helium in a H-mode plasma). This inward velocity is larger in H-mode than in L-mode [Henderson, 2012]; this is consistent with the theory of the drag force drift assuming a more negative edge electric field in the H-mode plasma than the L-mode case, as suggested by [Meyer et al., 2011] (see figure 5.1).

The diffusion coefficients for carbon and helium are similar in comparative experiments, as would be expected from neoclassical theory. The CUEBIT simulation presented in figure 6.6 implies a core diffusion coefficient, using the effective diffusivity of the previous chapter, of < 1 m^2 s^{-1} which rises to approximately 5 m^2 s^{-1} at the plasma edge. This is broadly consistent, although somewhat higher than, the figures of figure 6.8. Dedicated simulations which attempt to match the magnetic geometry, bulk ion density and temperature profiles, radial electric field and bulk ion rotation profiles would be required in order to attempt a quantitative comparison with experiment. This is an area for future work.

A qualitative comparison of the time evolution of the carbon density profile with simulation reveals significant differences between these results and CUEBIT simulations, reflecting the simplicity of the model employed in the present work. The CUEBIT model currently neglects any MHD activity, anomalous transport and fluctuations of the radial electric field, which will all affect the transport of impurity ions. Furthermore, the experimental results are strongly influenced by the position of injection of the impurities, whereas the simulated impurity ions are initialised with a uniform distribution across the plasma minor radius.

Chapter 7

Concluding remarks

The present thesis has detailed the development and application of a test particle, full orbit code for the investigation of collisional transport of impurity ions in spherical tokamak fusion plasmas. This may be extended and improved upon in a number of ways. We present in this final part of this thesis a summary of the key results and a number of possible future studies; this is by no means an exhaustive list.

7.1 Thesis summary

The key results of the present work are concerned with the modifications to the collisional transport of test impurity ions due to a radial electric field. It has been shown that such an electric field can significantly increase the confinement of test ions. This effect has been characterised in terms of a drag force drift, which is independent of particle mass but dependent on particle charge, Z, as derived analytically from the Lorentz-Langevin equation and verified numerically using the CUEBIT code in chapter 5. This effect has important consequences for the confinement of impurity ions in tokamak plasmas; since high-performance tokamak discharges tend to be associated with steep density and temperature profiles and large edge radial electric fields one would expect a significant impurity accumulation in the plasma core due to neoclassical impurity accumulation and additionally, in the context of the present work, due to the drag force drift in stationary H-mode plasmas. However, whilst a static radial electric field has been shown to lead to a significant enhancement of impurity ions, particularly for high-Z ions, the introduction of a time dependency of this field, due to, for example, edge localised modes, has been shown to minimise or even eliminate the accumulation due to the drag-force drift, as demonstrated in chapter 6. Further work is required in order to determine the scaling with mass and

charge of the effect of a time varying electric field on collisional transport coefficients.

7.2 Topics for future work

One of the key motivations for the application of the test particle approach to the problem of the radial electric field and collisional transport was the limitation of the previous theories of gyro- and drift-orbit squeezing for describing the predicted role of radial electric fields of the form observed in the edge of MAST plasmas. However, in the present work, whilst we have included radial electric field profiles which have been chosen to resemble the edge electric field observed in MAST, we have concentrated on the effect of the strength of the edge radial electric field since the drag force drift, as derived in section 5.4.2, depends only on the magnitude of this field. We may nevertheless extend the previous discussion to include a spatial variation of the electric field. Repeating the calculation of section 5.4.2 but allowing for such a spatial variation we find that the solution of the Lorentz-Langevin equation, again assuming Cartesian coordinates with $\mathbf{B} = B\hat{\mathbf{z}}$ and $\mathbf{E} = E_\perp \hat{\mathbf{x}}$, is given by

$$v_{\mathrm{x}} = u_{\mathrm{x}} + |v_\perp| e^{-\nu_{\mathrm{zi}} t} \cos\sqrt{S}\Omega t + \frac{E_\perp}{B}\frac{\nu_{\mathrm{zi}}}{\Omega}\frac{1}{S + \nu_{\mathrm{zi}}^2/\Omega^2}, \tag{7.1a}$$

$$v_{\mathrm{y}} = u_{\mathrm{y}} + \sqrt{S}|v_\perp| e^{-\nu_{\mathrm{zi}} t} \sin\sqrt{S}\Omega t - \frac{E_\perp}{B}\frac{1}{1 + S\nu_{\mathrm{zi}}^2/\Omega^2}. \tag{7.1b}$$

Here S is the squeeze factor introduced in section 5.2,

$$S = 1 - \frac{ZeE'_\perp}{m_{\mathrm{Z}}\Omega^2} = 1 - \frac{Ze\Phi''}{m_{\mathrm{Z}}\Omega^2}. \tag{7.2}$$

The modification to the cyclotron motion in (7.1) is exactly as found in section 5.2. Again assuming that $\nu_{\mathrm{zi}}^2 \ll \Omega^2$ we recover the usual $\mathbf{E}\times\mathbf{B}$ drift in the y-direction and a modified drag velocity in the x-direction. This differs from the result of section 5.2 by the squeeze factor in the denominator of this term. We therefore find that the drag force drift velocity is correspondingly modified and is no longer independent of particle mass. Consequently, the modified diffusion coefficient used throughout section 5.2, D_{eff}, is also no longer independent of particle mass. We instead find that the extent of the modification of D_{eff} due to the radial electric field depends on the sign of the electric field shear, Φ'', with $S > 1$ decreasing the significance of this modification and $S < 1$ increasing it. An interesting course of future work could be to determine a suitable parametrisation of the spatial variation of the radial electric field and to determine the role of this variation on the collisional transport of test ions. One could then also attempt to demonstrate the correspondence between the

Langevin approach of the present work with the previous theories of orbit-squeezing.

Throughout the present work it is assumed that the radial electric field can be modelled using a flux surface function for the electrostatic potential [see (5.12)]. In reality however MHD and ELM activity will lead to a time variation in the magnetic vector potential and thus an additional contribution to the electric field. The mode structure of the MHD activity will lead to a modification of the poloidal structure of the radial electric field; currently the only poloidal variation of the electric field included in CUEBIT is due to plasma shaping. It would be interesting to investigate the role of the poloidal structure of the radial electric field on impurity ion transport and the distribution of particle losses with a time variation of this field. Generally, diagnostics of the edge radial electric field provide information on the electric field close to the outboard mid-plane and not the poloidal structure of the field, so a direct comparison with experiment would be difficult.

One of the key experiences gained during the course of the present work is the appropriate benchmarking of the CUEBIT code against neoclassical theory, which is crucial if one is to have confidence in the results obtained with this code. Chapter 4 demonstrates the correspondence between the CUEBIT test particle code and the neoclassical transport code NCLASS at large aspect ratio. At tight aspect ratio the agreement is not as good due to finite drift orbit and finite system size effects, as outlined in section 4.3.2. A more complete neoclassical benchmarking could investigate the scaling of this disagreement with aspect ratio and determine the limit of applicability of the NCLASS (and similar) codes. The derivation of the model employed in NCLASS utilises a number of assumptions. To quote from Houlberg et al. [1997]:

> ... none of the models considered [in NCLASS] are applicable within a banana width of the plasma edge... Second, near the axis real ion orbits are also not well represented by the approximation of orbits concentric about the axis and thin relative to the minor radius made in the kinetic determination of the viscosity.

It would therefore be interesting to compare calculations of impurity ion transport coefficients across the entire plasma minor radius in order to to determine the level of correspondence between NCLASS and CUEBIT across the minor radius for a range of aspect ratios, rather than the local calculations presented in chapter 4. Particularly in tight aspect ratio devices the ion banana orbit width can be a significant fraction of the minor radius of the device, suggesting that the application of NCLASS to the study of collisional transport in MAST may be questionable for

a significant fraction of the MAST plasma. In a similar vein it would be fruitful to compare CUEBIT to more complete neoclassical models, such as the global neoclassical codes of Wang et al. [2006] and Landreman and Ernst [2012a,b], in order to validate the results of CUEBIT at tight aspect ratio.

The use of the full orbit approach discussed in the present work is not only applicable to the study of impurity ions but also to the study of fast, non-thermal, bulk and minority ions. It has previously been demonstrated that non-adiabatic particle motion at tight aspect ratio (that is particle motion which does not demonstrate conservation of the first order expansion of the magnetic moment, μ) can lead to trapping and de-trapping of fast injected bulk ions even in the absence of collisions [Akers et al., 2002]. CUEBIT is well suited to the study of such ions since no assumption on the constancy of μ is made (unlike in guiding centre codes). However, the previous statement is made with the caveat that an improved, velocity dependent collision operator must be implemented in place of the model of collisions presented in section 3.5. Such an extension of the CUEBIT model has recently been implemented [McClements and Hole, 2012], which therefore extends the applicability of CUEBIT to the investigation of fast particle physics on collisional slowing-down time scales, a critical issue for ITER. The inclusion of a velocity dependent friction force in CUEBIT allows for a wide range of future investigations of fast particle physics.

Throughout the discussion of the radial electric field in the present work it was assumed that the pressure gradient term in the momentum balance equation (5.1) was the dominant contribution to the radial electric field. Thus the contribution from the bulk plasma rotation was neglected. However, in reality there is a contribution from plasma rotation that must be included in a complete simulation of transport barriers in tokamak plasmas. Rotation is particularly important for minority ions compared with bulk plasma ions since the bulk ion rotation velocity can be comparable to or greater than the thermal velocity of impurity species. The effect of the rotation of the bulk plasma ions on minority ion transport has previously been studied using CUEBIT [McKay, 2008; McClements and McKay, 2009]. It has been shown that rotation of the bulk ions can significantly increase the rate of collisional impurity ion transport, particularly for incompletely ionised, heavy impurities. This is likely to offset the enhanced confinement of test impurity ions due to the drag force drift demonstrated in the present work.

Finally, the incorporation of numerical equilibria in the present work (see section 3.4) and the work of previous authors [Romanelli et al., 2011] has demonstrated the ease with which the CUEBIT test particle code may be incorporated

with and used with other numerical models. One area of potential future study is the investigation of transport driven by turbulent fluctuations of the electric and magnetic fields. Romanelli et al. [2011] coupled CUEBIT with a fluid turbulence code (CUTIE, [Thyagaraja, 2000]), which was used to compute fluctuating electric and magnetic fields used as inputs to CUEBIT. This study demonstrated that fluctuating magnetic fields lead to non-diffusive and non-local transport of test ions. Since transport is no longer diffusive, and the mean square displacement measurement is no longer applicable, the authors therefore characterised the effect of field fluctuations solely by the confinement time of the test ions, that is the time taken for the number of particles lost through the last closed flux surface to reach a fraction of $1/e$ of their initial number. The definition of an effective diffusion coefficient or the particle fluence and particle flux measurement of section 4.2.2 would provide additional diagnostics to quantify the role of fluctuations on impurity ion transport.

An alternative to the inclusion of a turbulence code would be to extend the Langevin equation used throughout this work to include fluctuations of the electric and magnetic fields, given a suitable description of the turbulent spectrum of fluctuations of these quantities, in a manner similar to the work of Thyagaraja et al. [1985] and Hannibal [1993].

The incorporation of CUEBIT into a suite of codes which treat separate physics issues, such as an equilibrium code, as demonstrated in the present work, and, for example, turbulence and plasma wave codes, would allow one to determine impurity ion transport coefficients in a more complete model of tokamak plasmas. The use of CUEBIT to determine transport coefficients is particularly important for plasma conditions in which the validity of the NCLASS model is not strictly valid, for example at tight aspect ratio, as demonstrated in the present work (see 4.3.2), or in plasmas with large plasma rotation. Additional codes could be used to model the contribution to the plasma species transport coefficients due to, for example, turbulence and MHD activity.

These transport coefficients could then, in principle, be used to solve for the evolution of the temperature and density profiles of the plasma species in addition to the evolution of plasma equilibrium quantities such as the flux surface geometry and the radial electric field, creating a self-consistent loop which describes the long-time evolution of these quantities. The codes described above could be used to solve for the instantaneous plasma transport coefficients, given a fixed plasma equilibrium. These transport coefficients then determine the evolution of the respective density

profiles through, for example, the continuity equation [Helander and Sigmar, 2002]

$$\frac{\partial n_s}{\partial t} = -\nabla \cdot \Gamma_s, \tag{7.3}$$

which can be solved with significantly larger time step than may be used in, for example, CUEBIT, which is limited in time step by the particle cyclotron frequency. Finally, these evolved plasma profiles can then feedback into the solution of a new plasma equilibrium and the whole process repeated. In order to facilitate this numerical scheme the spline interpolation routines used in the solution of particle orbits in numerically defined equilibria (see section 3.4) have been extended in order to allow for the numerical prescription of the bulk ion profiles and the radial electric field. Preliminary simulations have been successfully performed with the plasma equilibrium, the bulk ion density and temperature profiles and the radial electric field all prescribed numerically.

Bibliography

R J Akers, L C Appel, P G Carolan, N J Conway, G F Counsell, M Cox, S J Gee, M P Gryaznevich, R Martin, A W Morris, M P S Nightingale, A Sykes, M Mironov, and M J Walsh. Neutral beam heating in the START spherical tokamak. *Nuclear Fusion*, 42:122–35, 2002.

R J Akers et al. Transport and confinement in the Mega Ampère Spherical Tokamak (MAST) plasma. *Plasma Physics and Controlled Fusion*, 45:A175–A204, 2003.

P Alexandroff and H Hopf. *Topologie*. Verlag Julius Springer, Germany, 1935.

H Alfvén. On the motion of a charged particle in a magnetic field. *Arkiv för Matematik, Astronomi och Fysik*, 27A:1–20, 1940.

C Angioni, E Fable, M Greenwald, M Maslov, A G Peeters, H Takenaga, and H Weisen. Particle transport in tokamak plasmas, theory and experiment. *Plasma Physics and Controlled Fusion*, 51:124017, 2009.

ASDEX Team. The H-mode of ASDEX. *Nuclear Fusion*, 29:1959–2040, 1989.

C V Atanasiu, S Günter, K Lackner, and I G Miron. Analytical solutions to the Grad-Shafranov equation. *Physics of Plasmas*, 11:3510–8, 2004.

R Balescu. *Aspects of anomalous transport in plasmas*. Series in Plasma Physics. Institute of Physics, UK, 2005.

A Baños. The guiding centre approximation in lowest order. *Journal of Plasma Physics*, 1:305–16, 1967.

N Ben Ayed, A Kirk, B Dudson, S Tallents, R G L Vann, H R Wilson, and the MAST team. Inter-ELM filaments and turbulent transport in the Mega-Amp Spherical Tokamak. *Plasma Physics and Controlled Fusion*, 51:035016, 2009.

R J Bickerton, J W Connor, and J B Taylor. Diffusion driven plasma currents and bootstrap tokamak. *Nature Physical Science*, 229:110–2, 1971.

C K Birdsall and A B Langdon. *Plasma physics via computer simulation*. McGraw-Hill, New York, 1985.

A H Boozer and G Kuo-Petravic. Monte Carlo evaluation of transport coefficients. *Physics of Fluids*, 24:2851–9, 1981.

J P Boris. Relativistic plasma simulation — optimization of a hybrid code. In *Proceedings of the 4th Conference on Numerical Simulation of Plasmas*, pages 3–67, Washington, DC, 1970.

C M Braams and P E Stott. *Nuclear Fusion: Half a Century of Magnetic Confinement Fusion Research*. Series on Plasma Physics. Institute of Physics, UK, 2002.

S I Braginskii. Transport processes in a plasma. In *Reviews of Plasma Physics*, volume 1, pages 205–311. Consultants Bureau, New York, 1965.

K H Burrell, E J Doyle, P Gohil, R J Groebner, J Kim, R J La Haye, L L Lao, R A Moyer, T H Osborne, W A Peebles, C L Rettig, T H Rhodes, and D M Thomas. Role of the radial electric field in the transition from L (low) mode to H (high) mode to VH (very high) mode in the DIII-D tokamak. *Physics of Plasmas*, 1: 1536–44, 1994.

A Bustos, F Castejón, L A Fernández, J García, V Martin-Mayor, J M Reynolds, R Seki, and J L Velasco. Impact of 3D features on ion collisional transport in ITER. *Nuclear Fusion*, 50:125007, 2010.

J D Callen, C C Hegna, and A L Cole. Transport equations in tokamak plasmas. *Physics of Plasmas*, 17:056113, 2010.

J R Cary and A J Brizard. Hamiltonian theory of guiding-center motion. *Reviews of Modern Physics*, 81:693–738, 2009.

J R Cary and R G Littlejohn. Noncanonical Hamiltonian mechanics and its application to magnetic field line flow. *Annals of Physics*, 151:1–34, 1983.

A J Cerfon and J P Freidberg. "One size fits all" analytic solutions to the Grad-Shafranov equation. *Physics of Plasmas*, 17:032502, 2010.

H Chen, N C Hawkes, L C Ingesson, N J Peacock, and M G Haines. Impurity transport with strong and weak internal transport barriers in JET optimized shear plasmas. *Nuclear Fusion*, 41:31–46, 2001.

W T Coffey, Yu P Kalmykov, and J T Waldron. *The Langevin equation: with applications to stochastic problems in physics, chemistry, and electrical engineering.* World Scientific, Singapore, 2nd edition, 2004.

J W Connor, T Fukuda, X Garbet, C Gormezano, V Mukhovatov, M Wakatani, the ITB Database Group, and the ITPA Topical Group on Transport and Internal Barrier Physics. A review of internal transport barrier physics for steady-state operation of tokamaks. *Nuclear Fusion*, 44:R1–R49, 2004.

M Cox and the MAST team. The mega amp spherical tokamak. *Fusion Engineering and Design*, 46:397–404, 1999.

M de Rover, A M R Schilham, A Montvai, and N J Lopes Cardozo. Test particle transport in perturbed magnetic fields in tokamaks. *Physics of Plasmas*, 6:2443–51, 1999.

W D D'haeseleer, W N G Hitchon, J D Callen, and J L Shohet. *Flux coordinates and magnetic field structure: a guide to a fundamental tool of plasma theory.* Springer-Verlag, Berlin, 2001.

R Dux and A G Peeters. Neoclassical impurity transport in the core of an ignited tokamak plasma. *Nuclear Fusion*, 40:1721–9, 2000.

R Dux, A G Peeters, A Gude, A Kallenbach, R Neu, and ASDEX Upgrade Team. Z dependence of the core impurity transport in ASDEX Upgrade H mode discharges. *Nuclear Fusion*, 39:1509–22, 1999.

J W Edenstrasser. Unified treatment of symmetric MHD equilibria. *Journal of Plasma Physics*, 24:299–313, 1980.

T Estrada, T Happel, L Eliseev, D López-Bruna, E Ascasíbar, E Blanco, L Cupido, J M Fontdecaba, C Hidalgo, R Jiménez-Gómez, L Krupnik, M Liniers, M E Manso, K J McCarthy, F Medina, A Melnikov, B van Milligen, M A Ochando, I Pastor, M A Pedrosa, F L Tabarés, D Tafalla, and TJ-II Team. Sheared flows and transition to improved connement regime in the TJ-II stellarator. *Plasma Physics and Controlled Fusion*, 51:124015, 2009.

A R Field, J McCone, N J Conway, M Dunstan, S Newton, and M Wisse. Comparison of measured poloidal rotation in MAST spherical tokamak plasmas with neo-classical predictions. *Plasma Physics and Controlled Fusion*, 51:105002, 2009.

A R Field et al. Plasma rotation and transport in MAST spherical tokamak. *Nuclear Fusion*, 51:063006, 2011.

J P Freidberg. Ideal magnetohydrodynamic theory of magnetic fusion systems. *Reviews of Modern Physics*, 54:801–902, 1982.

J P Freidberg. *Ideal Magnetohydrodynamics*. Plenum, New York, 1987.

A A Galeev and R Z Sagdeev. Transport phenomena in a collisionless plasma in a toroidal magnetic system. *Soviet Physics JETP*, 26:233–40, 1968.

D A Gates, H E Mynick, and R B White. Collisional transport in a low aspect ratio tokamak. *Physics of Plasmas*, 11:L45, 2004.

R Giannella, L Lauro-Taroni, M Mattioli, B Alper, B Denne-Hinnov, G Magyar, J O'Rourke, and D Pasini. Role of current profile in impurity transport in JET L mode discharges. *Nuclear Fusion*, 34:1185–202, 1994.

C Giroud, R Barnsley, P Buratti, I H Coffey, M von Hellermann, C Jupen, K D Lawson, A Meigs, M O'Mullane, and A D Whiteford. Method for experimental determination of Z dependence of impurity transport on JET. *Nuclear Fusion*, 47:313–30, 2007.

H Grad and H Rubin. Hydromagnetic equilibria and force-free fields. In *Proceedings of the 2nd United Nations International Conference on the Peaceful Uses of Atomic Energy, Geneva*, 1958.

L Guazzotto and J P Freidberg. A family of analytic equilibrium solutions for the Grad-Shafranov equation. *Physics of Plasmas*, 14:112508, 2007.

V K Gusev, F Alladio, and A W Morris. The basics of spherical tokamaks and progress in European research. *Plasma Physics and Controlled Fusion*, 45:A59–A82, 2003.

J Halton. On the efficiency of certain quasirandom sequences of points in evaluating multidimensional integrals. *Numerische Mathematik*, 2:84–90, 1960.

B Hamilton, K G McClements, L Fletcher, and A Thyagaraja. Field-guided proton acceleration at reconnecting X-points in flares. *Solar Physics*, 214:339–52, 2003.

J M Hammersley. Monte-Carlo methods for solving multivariable problems. *Annals of the New York Academy of Science*, 86:844–74, 1960.

L Hannibal. Test particle transport in stochastic magnetic
elds modeled by stochastic processes. *Physics of Fluids B*, 5:3551–7, 1993.

R D Hazeltine. Self-consistent radial sheath. *Physics of Fluids B*, 1:2031–9, 1989.

C C Hegna, J D Callen, T A Gianakon, W X Qu, A I Smolyakov, and J P Wang. Magnetic islands and their effects in tokamak plasmas. *Plasma Physics and Controlled Fusion*, 35:987–1002, 1993.

J A Heikkinen, T P Kiviniemi, T Kurki-Suonio, A G Peeters, and S K Sipilä. Particle simulation of the neoclassical plasmas. *Journal of Computational Physics*, 173: 527–48, 2001.

P Helander and D J Sigmar. *Collisional transport in magnetized plasmas*. Cambridge monographs on plasma physics. Cambridge University Press, UK, 2002.

S Henderson. Private communication, 2012.

F L Hinton and R D Hazeltine. Theory of plasma transport in toroidal confinement systems. *Reviews of Modern Physics*, 48:239–308, 1976.

F L Hinton and Y B Kim. Poloidal rotation in tokamaks with large electric field gradients. *Physics of Plasmas*, 2:159–66, 1995.

S P Hirshman and D J Sigmar. Neoclassical transport of impurities in tokamak plasmas. *Nuclear Fusion*, 21:1079–201, 1981.

W A Houlberg, K C Shaing, S P Hirshman, and M C Zarnstorff. Bootstrap current and neoclassical transport in tokamak of arbitrary collisionality and aspect ratio. *Physics of Plasmas*, 4:3230–42, 1997.

G T A Huysmans and O Czarny. MHD stability in X-point geometry: simulation of ELMs. *Nuclear Fusion*, 47:659–66, 2007.

K Ida. Experimental studies of the physical mechanism determining the radial electric field and its radial structure in a toroidal plasma. *Plasma Physics and Controlled Fusion*, 40:1429–88, 1998.

ITER Physics Basis Editors, ITER Physics Expert Group Chairs and Co-Chairs, and ITER Joint Central Team and Physics Integration Unit. ITER Physics Basis Chapter 1: Overview and summary. *Nuclear Fusion*, 39:2137–6389, 1999.

ITER Physics Expert Group on Confinement and Transport, ITER Physics Expert Group on Confinement Modelling and Database, and ITER Physics Basis Editors. ITER Physics Basis Chapter 2: Plasma confinement and transport. *Nuclear Fusion*, 39:2175–249, 1999.

K Itoh and S I Itoh. The role of the electric field in confinement. *Plasma Physics and Controlled Fusion*, 38:1–49, 1996.

M A Janzer et al. Investigating impurity transport in the plasma edge at ASDEX upgrade. In *TTG*, page 10.03, September 2010.

S M Kaye et al. Progress towards high performance plasmas in the National Spherical Torus Experiment (NSTX). *Nuclear Fusion*, 45:S168–S180, 2005.

Y O Kazakov and Z S Kononenko. Test particle modelling of ion collisional transport in tokamaks. *Nukleonika*, 57:43–7, 2012.

T P Kiviniemi, J A Heikkinen, and A G Peeters. Test particle simulation of non-ambipolar ion diffusion in tokamaks. *Nuclear Fusion*, 40:1587–96, 2000.

Zh S Kononenko and A A Shishkin. Impurity ion dynamics near magnetic islands in the drift optimized stellarator configuration of Wendelstein 7-X. *Ukrainian Journal of Physics*, 53:437–41, 2008.

M Kotschenreuther, W Dorland, Q P Liu, M C Zarnstorff, R L Miller, and Y R Lin-Liu. Attaining neoclassical transport in ignited tokamaks. *Nuclear Fusion*, 40:677–84, 2000.

A Krämer-Flecken, S Soldatov, D Reiser, M Kantor, and H R Koslowski. Investigation of geodesic acoustic modes and related zonal flows at TEXTOR. *Plasma Physics and Controlled Fusion*, 51:015001, 2009.

S I Krasheninnikoy and P N Yushmanoy. The influence of a radial electric field on neoclassical orbits and ion prompt losses from tokamak edge plasmas. *Physics of Plasmas*, 1:1186–94, 1994.

L D Landau and E M Lifshitz. *Mechanics*. Course of theoretical physics. Butterworth-Heinemann, 1976.

M Landreman and D R Ernst. Changes to neoclassical flow and bootstrap current in a tokamak pedestal. arXiv, June 2012a. http://arxiv.org/abs/1206.5912v1.

M Landreman and D R Ernst. Local and global fokker-planck neoclassical calculations showing flow and bootstrap current modification in a pedestal. arXiv, July 2012b. http://arxiv.org/abs/1207.1795v1.

P Langevin. Sur la theórie du mouvement brownien. *Comptes rendus de l'Académie des Sciences*, 146:530–3, 1908.

L L Lao, H St. John, R D Stambaugh, A G Kellman, and W Pfeiffer. Reconstruction of current profile parameters and plasma shapes in tokamaks. *Nuclear Fusion*, 25: 1611–22, 1985.

X Lapillonne, S Brunner, T Dannert, S Jolliet, A Marinoni, L Villard, T Görler, F Jenko, and F Merz. Clarifications to the limitations of the s-α equilibrium model for gyrokinetic computations of turbulence. *Physics of Plasmas*, 16:032308, 2009.

J D Lawson. Some criteria for a power producing thermonuclear reactor. *Proceedings of the Physical Socieity*, B70:6–10, 1957.

E A Lazarus et al. Higher fusion power gain with current and pressure profile control in strongly shaped DIII-D tokamak plasmas. *Physical Review Letters*, 77:2714–7, 1996.

W W Lee. Gyrokinetic approach in particle simulation. *Physics of Fluids*, 26:556–62, 1983.

F M Levinton, M C Zarnstorff, S H Batha, M Bell, R E Bell, R V Budny, C Bush, Z Chang, E Fredrickson, A Janos, J Manickam, A Ramsey, S A Sabbagh, G L Schmidt, E J Synakowski, and G Taylor. Improved confinement with reversed magnetic shear in TFTR. *Physical Review Letters*, 75:4417–20, 1995.

R G Littlejohn. Variational principles of guiding centre motion. *Journal of Plasma Physics*, 29:111–25, 1983.

R G Littlejohn. Phase anholonomy in the classical adiabatic motion of charged particles. *Physical Review A*, 38:6034–45, 1988.

C Llewelyn-Smith and D Ward. Fusion power. *European Review*, 13:337–59, 2005.

B Lloyd et al. MAST and the impact of low aspect ratio on tokamak physics. *Plasma Physics and Controlled Fusion*, 46:B477–B494, 2004.

A Loarte, G Saibene, R Sartori, D Campbell, M Becoulet, L Horton, T Eich, A Herrmann, G Matthews, N Asakura, A Chankin, A Leonard, G Porter, G Federici, G Janeschitz, M Shimada, and M Sugihara. Characteristics of type I ELM energy and particle losses in existing devices and their extrapolation to ITER. *Plasma Physics and Controlled Fusion*, 45:1549–69, 2003.

R Lust and A Schlüter. Axialsymmetrische magnetohydrodynamische gleichgewichtskonfigurationen. *Zeitschrift fur Naturforschung*, 12a:850–854, 1957.

H Lütjens, A Bondeson, and A Roy. Axisymmetric MHD equilibrium solver with bicubic Hermite elements. *Computer Physics Communications*, 69:287–98, 1992.

H Lütjens, A Bondeson, and O Sauter. The CHEASE code for toroidal MHD equilibria. *Computer Physics Communications*, 97:219–60, 1996.

A Maluckov, N Nakajima, M Okamoto, S Murakami, and R Kanno. Statistical properties of the neoclassical radial diffusion in a tokamak equilibrium. *Plasma Physics and Controlled Fusion*, 43:1211–26, 2001.

K G McClements. Full orbit computations of ripple-induced fusion α-particle losses from burning tokamak plasmas. *Physics of Plasmas*, 12:2072510, 2005.

K G McClements and M J Hole. Toroidal ripple transport of beam ions in the mega-ampère spherical tokamak. *Physics of Plasmas*, 19:072514, 2012.

K G McClements and R J McKay. The orbital dynamics and collisional transport of trace massive impurity ions in rotating tokamaks. *Plasma Physics and Controlled Fusion*, 51:115009, 2009.

K G McClements, A Thyagaraja, and B Hamilton. An energy-conserving scheme for solving the Lorentz force equation. Culham Plasma Physics Note 2002/2.1, Culham Science Centre, 2002.

J McCone. Private communication, 2011.

R M McDermott, B Lipschultz, J W Hughes, P J Catto, A E Hubbard, I H Hutchinson, R S Granetz, M Greenwald, B LaBombard, K Marr, M L Reinke, J E Rice, D Whyte, and Alcator C-Mod Team. Edge radial electric field structure and its connections to H-mode confinement in Alcator C-Mod plasmas. *Physics of Plasmas*, 16:056103, 2009.

R McKay. *Test particle studies of acceleration and transport in solar and tokamak plasmas*. PhD thesis, University of Glasgow, 2008.

R J McKay, K G McClements, A Thyagaraja, and L Fletcher. Test-particle simulations of collisional impurity transport in rotating spherical tokamak plasmas. *Plasma Physics and Controlled Fusion*, 50:065017, 2008.

H Meyer, C Bunting, P G Carolan, N J Conway, M R Dunstan, A Kirk, R Scannell, D Temple, M Walsh, the MAST, and NBI Teams. The structure, evolution and role of the radial edge electric field in H-mode and L-mode on MAST. *Journal of Physics: Conference Series*, 123:012005, 2008.

H Meyer, N F M De Bock, N J Conway, S J Freethy, K Gibson, J Hiratsuka, A Kirk, C A Michael, T Morgan, R Scannell, G Naylor, S Saarelma, A N Saveliev, V F Shevchenko, W Suttrop, D Temple, R G L Vann, and the MAST and NBI teams. L-H transition and pedestal studies on MAST. *Nuclear Fusion*, 51:113011, 2011.

H Meyer et al. Formation of transport barriers in the MAST spherical tokamak. *Plasma Physics and Controlled Fusion*, 46:A291–A298, 2004.

H Meyer et al. Overview of physics results from MAST. *Nuclear Fusion*, 49:104017, 2009.

R L Miller. Economic goals and requirements for competitive fusion energy. *Fusion Engineering and Design*, 41:393–400, 1998.

Y Murakami, T Amano, K Shimizu, and M Shimada. Transport analysis of tungsten impurity in ITER. *Journal of Nuclear Materials*, 313–316:1161–6, 2003.

F Najmabadi. Prospects for attractive fusion power systems. *Philosophical Transactions of the Royal Society of London A*, 357:625–38, 1999.

H Nersisyan, C Toepffer, and G Zwicknagel. *Interactions between charged particles in a magnetic field: a theoretical approach to ion stopping in magnetized plasmas.* Course of theoretical physics. Springer–Verlag, Berlin, Germany, 2007.

T G Northrop. *Adiabatic motion of charged particles.* Wiley, New York, 1963.

W J Nuttall. *Fusion as an Energy Source: Challenges and Opportunities.* IOP, UK, 2008.

A G Peeters. Reduced charge state equations that describe Pfirsch Schlüter impurity transport in tokamak plasma. *Physics of Plasmas*, 7:268–75, 2000.

R F Post. Controlled fusion research — an application of the physics of high temperature plasmas. *Reviews of Modern Physics*, 28:338–62, 1956.

H Qin, X Guan, and W M Tang. Variational symplectic algorithm for guiding center dynamics and its application in tokamak geometry. *Physics of Plasmas*, 16:042510, 2009.

P H Rebut, R J Bickerton, and B E Keen. The Joint European Torus: installation, first results and prospects. *Nuclear Fusion*, 25:1011–22, 1985.

C M Roach, J W Connor, and S Janjua. Trapped particle precession in advanced tokamaks. *Plasma Physics and Controlled Fusion*, 37:679–98, 1995.

A L Rogister. Transport barriers formation and subneoclassical energy fluxes: a unified theoretical approach. *Physical Review Letters*, 81:3663–6, 1998.

M Romanelli, K G McClements, J Cross, P J Knight, A Thyagaraja, and J Callaghan. Full orbit simulation of collisional transport of impurity ions in the MAST spherical tokamak. *Plasma Physics and Controlled Fusion*, 53:054017, 2011.

V D Shafranov. On magnetohydrodynamical equilibrium configurations. *Soviet Physics JETP*, 6:545, 1958.

K C Shaing and R D Hazeltine. Effects of orbit squeezing on ion transport in the banana regime in tokamaks. *Physics of Fluids B*, 4:2547–51, 1992.

K C Shaing and M C Zarnstor. Effects of orbit squeezing on transport flluxes. *Physics of Plasmas*, 4:3928–32, 1997.

K C Shaing, A Y Aydemir, and R D Hazeltine. Effects of orbit distortion on classical transport. *Physics of Plasmas*, 5:3680–4, 1998.

J Sheffield, W Brown, G Garrett, J Hilley, D McCloud, J Ogden, T Shields, and L Waganer. A study of options for the deployment of large fusion power plant. *Fusion Science and Technology*, 40:1–35, 2001.

M Shimada, D J Campbell, V Mukhovatov, M Fujiwara, N Kirneva, K Lackner, M Nagami, V D Pustovitov, N Uckan, J Wesley, N Asakura, A E Costley, A J H Donné, E J Doyle, A Fasoli, C Gormezano, Y Gribov, O Gruber, T C Hender, W A Houlberg, S Ide, Y Kamada, A Leonard, B Lipschultz, A Loarte, K Miyamoto, V Mukhovatov, T H Osborne, A Polevoi, and A C C Sips. Progress in the ITER Physics Basis Chapter 1: Overview and summary. *Nuclear Fusion*, 47:S1, 2007.

R V Shurygin and R L Dewar. Anomalous transport barriers due to sheared radial electric fields in tokamaks. *Plasma Physics and Controlled Fusion*, 31:1311–35, 1995.

L S Solov'ev. The theory of hydromagnetic stability of toroidal plasma configurations. *Soviet Physics JETP*, 26:400–7, 1968.

L S Solov'ev and V D Shafranov. Plasma confinement in closed magnetic systems. In *Reviews of Plasma Physics*, volume 5, pages 1–247. Consultants Bureau, New York, 1966.

L Jr Spitzer. *Physics of fully ionized gases.* Interscience, New York, 1967.

E Strumberger. Deposition patterns of fast ions on plasma facing components in W7-X. *Nuclear Fusion*, 40:1697–713, 2000.

D Stutman, M Finkenthal, R E Bell, S M Kaye, B P LeBlanc, J E Menard, E J Synakowski, D S Darrow, V Soukhanovskii, and C Bourdelle. Impurity transport measurements in beam heated low-confinement mode discharges in the National Spherical Torus Experiment. *Physics of Plasmas*, 10:4387–95, 2003.

D Stutman, M Finkenthal, K Tritz, M H Redi, S M Kaye, M G Bell, R E Bell, B P LeBlanc, K W Hill, S S Medley, J E Menard, G Rewoldt, W X Wang, E J Synakowski, F Levinton, S Kubota, C Bourdelle, W Dorland, and The NSTX Team. Studies of improved electron confinement in low density L-mode National Spherical Torus Experiment discharges. *Physics of Plasmas*, 13:092511, 2006.

E J Synakowski, B C Stratton, P C Efthimion, R J Fonck, R A Hulse, D W Johnson, D K Mansfield, H Park, S D Scott, and G Taylor. Measurements of radial profiles of He2+ transport coefficients on the TFTR tokamak. *Physical Review Letters*, 65:2255–8, 1990.

E J Synakowski et al. Initial studies of core and edge transport of NSTX plasmas. *Plasma Physics and Controlled Fusion*, 44:A165–A173, 2002.

T Tala, Y Andrew, K Crombé, P C de Vries, X Garbet, N Hawkes, H Nordman, K Rantamäki, P Strand, A Thyagaraja, J Weiland, E Asp, Y Baranov, C Challis, G Corrigan, A Eriksson, C Giroud, M D Hua, I Jenkins, H C M Knoops, X Litaudon, P Mantica, V Naulin, V Parail, K D Zastrow, and JET-EFDA contributors. Toroidal and poloidal momentum transport studies in JET. *Nuclear Fusion*, 47:1012, 2007.

Y Q Tao, R W Conn, L Schmitz, and G Tynan. Ion flow in a strongly sheared electric field. *Physics of Plasmas*, 5:344–9, 1993.

D Temple, H Meyer, A Kirk, E Nardon, and the MAST and NBI teams. The radial electric field of MAST. In *Proceedings of the 36th EPS conference on Plasma Physics*, pages P–5.191, 2009.

A Thyagaraja. Numerical simulations of tokamak plasma turbulence and internal transport barriers. *Plasma Physics and Controlled Fusion*, 42:B255–B269, 2000.

A Thyagaraja, I L Robertson, and F A Haas. Test-particle transport due to fluctuating magnetic fields in tokamaks. *Plasma Physics and Controlled Fusion*, 27: 1217–41, 1985.

A Thyagaraja, M Valovič, and P J Knight. Global two-fluid turbulence simulations of L-H transitions and edge localized mode dynamics in the COMPASS-D tokamak. *Physics of Plasmas*, 17:042507, 2010.

K T Tsang, Y Matsuda, and H Okuda. Numerical simulation of neoclassical diffusion. *Physics of Fluids*, 18:1282–6, 1975.

N G Van Kampen. *Stochastic processes in physics and chemistry*. Elsevier, Oxford, UK, 3rd edition, 1992.

G E Vekstein, N A Bobrova, and S V Bulanov. On the motion of charged particles in a sheared force-free magnetic field. *Journal of Plasma Physics*, 67:215–21, 2002.

M R Wade, W A Houlberg, and LR Baylor. Evidence of neoclassical impurity transport in DIII-D. In *Transport Task Force meeting*, March 1998.

F Wagner, G Becker, K Behringer, D Campbell, A Eberhagen, W Engelhardt, G Fussmann, O Gehre, J Gernhardt, G v Gierke, G Haas, M Huang, F Karger, M Keilhacker, O Klüber, M Kornherr, K Lackner, G Lisitano, G G Lister, H M Mayer, D Meisel, E R Müller, H Murmann, H Niedermeyer, W Poschenrieder, H Rapp, H Röhr, F Schneider, G Siller, E Speth, A Stäbler, K H Steuer, G Venus, O Vollmer, and Z Yü. Regime of improved confinement and high beta in neutral-beam-heated divertor discharges of the ASDEX tokamak. *Physical Review Letters*, 49:1408–12, 1982.

W X Wang, G Rewoldt, W M Tang, F L Hinton, J Manickam, L E Zakharov, R B White, and S Kaye. Nonlocal neoclassical transport in tokamak and spherical torus experiments. *Physics of Plasmas*, 13:082501, 2006.

A A Ware. Pinch effect for trapped particles in a tokamak. *Physical Review Letters*, 325:15–7, 1970.

R H Weening. Aspect ratio scaling of toroidal plasma equilibria and the tokamak bootstrap effect. *Physics of Plasmas*, 4:3254–61, 1997.

R H Weening. Analytic spherical torus plasma equilibrium model. *Physics of Plasmas*, 7:3654–3662, 2000.

K W Wenzel and D J Sigmar. Neoclassical analysis of impurity transport following transition to improved particle confinement. *Nuclear Fusion*, 30:1117–28, 1990.

J Wesson. *Tokamaks*. Oxford University Press, Oxford, 3rd edition, 2004.

K L Wong and C Z Cheng. Orbit effects on impurity transport in a rotating tokamak plasma. *Physics of Fluids B*, 1:545–54, 1989.

M C Zarnstorff, M G Bell, M Bitter, R J Goldston, B Grek, R J Hawryluk, K Hill, D Johnson, D McCune, H Park, A Ramsey, G Taylor, and R Wieland. Bootstrap current in TFTR. *Physical Review Letters*, 60:1306–9, 1988.

S B Zheng, A J Wootton, and E R Solano. Analytical tokamak equilibrium for shaped plasmas. *Physics of Plasmas*, 3:1176–8, 1996.

H Zohm. The physics of edge localized modes (ELMs) and their role in power and particle exhaust. *Plasma Physics and Controlled Fusion*, 38:1213–23, 1996.